UNIVERSIDAD NACIONAL AUTÓNOMA DE MÉXICO

POSGRADO EN CIENCIA E INGENIERÍA DE LA COMPUTACIÓN

PHOTOACOUSTIC IMAGE RECONSTRUCTION OF HETEROGENEOUS MEDIA

T E S I S

QUE PARA OPTAR EL GRADO DE:

DOCTORADO EN CIENCIAS

PRESENTA:

VERENA MARGITTA MOOCK

CODIRECTORES DE TESIS:

DR. CRESCENCIO GARCÍA SEGUNDO, CCADET-UNAM

DR. EDGAR GARDUÑO ÁNGELES, IIMAS-UNAM

MÉXICO D.F.   NOVIEMBRE 2015

PHOTOACOUSTIC IMAGE RECONSTRUCTION OF HETEROGENEOUS MEDIA

VERENA MARGITTA MOOCK

A thesis submitted in fulfillment of the requirements for the degree of

DOCTOR OF PHILOSOPHY

in the Postgraduate Program of Computer Science and Engineering.

UNIVERSIDAD NACIONAL AUTÓNOMA DE MÉXICO

November 2015

Every man should plant a tree, have a child and write a book.

These all live on after us, insuring a measure of immortality.

– The Talmud and José Martí

An meine Familie

los muertos y los vivos

for their unconditional love

Verena M. Moock

Contents

Chapter 3   Inverse problems in heterogeneous media

Chapter 4   Enhanced photoacoustic image reconstruction

Chapter 5   Conclusions

List of Figures

List of Tables

List of Algorithms

List of Symbols

Symbols used in this document.

Symbol	Meaning	Page
μ_a	optical absorption coefficient	4
Φ	light fluence	4
$\mathbb{R}^n$	real space of dimension n	4
$\mathbf{x}$, $\mathbf{y}$	points in $\mathbb{R}^3$	4, 5
t	time instant	4
H	heat function	4
$a \cdot b = ab$	scalar product of a and b in $\mathbb{R}$	4
ω	angular frequency (measured in radians per second)	4, 33
$e, \exp$	exponential function	4
$\hat{\imath}$	imaginary unit equal to $\sqrt{-1}$	4
I_0	initial intensity of light	4
p	pressure distribution	5
$\mathscr{A}, \mathscr{B}, \mathscr{D}, \mathscr{H},$ $\mathscr{R}, \mathscr{T}, \mathscr{L}, \mathscr{P}$	linear transform operations	5, 20, 13-15, 29, 30-31, 33-34, 38, 44-47, 53-57
$:=$	is defined as	5, 13-15, 17
c	speed of sound	5
c^2	c squared, $c^2 := c \cdot c$	5
Γ	GrÃ¼neisen parameter	5
β	isobaric volume expansion coefficient	5
C_p	specific heat	5
J	Joule, unit of energy, work, or amount of heat	5
K	Kelvin, unit of measurement for temperature	5
kg	Kilogram; unit of mass	5
G	Green free-space function	5
$\delta\Omega$	boundary of the region Ω	5
∂_t	derivative with respect to t	5

Symbols used in this document.

Symbol	Meaning	Page
$\int_{\mathbb{R}^n} \bullet \, d\mathbf{x}$	integration of $\mathbf{x}$ over $\mathbb{R}^n$	5, 34
$\int_0^r \bullet \, dt$	integration of t over $[0,r] \subset \mathbb{R}$	20
$[\bullet]$	parenthesis of a unit declaration	5
m	Meter, unit of length	7
Hz	Hertz, unit of frequency	7
$f : D \to C$	function definition from the domain D to the target set C	13
$S \subset \mathscr{S}, \mathscr{S} \supset S$	S is subset of $\mathscr{S}$, a set of hyperplanes	13, 29
r	scalar	13
ϕ	angle	13
$\langle \bullet, \bullet \rangle$	scalar (or dot / inner) product of two vectors in $\mathbb{R}^n$	13
Φ^{n-1}	unit sphere in $\mathbb{R}^n$	13
w	scalar weighting function	13
$A \times B$	Cartesian product, $A \times B := \{(a,b) \mid a \in A, \ b \in B\}$	13, 20, 29, 50, 59, 61
$\approx$	approximately equal to	13
$\mathscr{P}^{-1}, \mathscr{R}^{-1}$	inverse operation	14
$\mathbb{N}$	natural numbers $\{1,2,3,...\}$	14, 50
i	integration index in $\{1,...,I\}, I \in \mathbb{N}$	17
j	pixel index in $\{1,...,J\}, J \in \mathbb{N}$	14
k	direction index in $\{1,...,K\}, K \in \mathbb{N}$	14
l	iteration index in $\{1,...,L\}, L \in \mathbb{N}$	15
m	structure index in $\{1,...,M\}, M \in \mathbb{N}$	44
$\mathbf{P}_k, \mathbf{R}, \mathbf{T}, \mathbf{U}, \mathbf{V}, \mathbf{W}$	matrices	16, 17, 49
$(\mathbf{R}_k)$	series of matrices with numerator $k \in \mathbb{N}$	16
$\mathbf{R}^{-1}$	inverse matrix of $\mathbf{R}$	16, 47
$\mathbf{R}^T$	transpose matrix of $\mathbf{R}$	17
$\mathbf{R}^*$	complex conjugate of $\mathbf{R}$	17
$\mathbf{e}, \mathbf{e}_k, \mathbf{f}, \mathbf{f}^\otimes, \mathbf{f}', \mathbf{g}, \mathbf{p}$	column-vectors	14, 15, 16, 20
$\bar{f}, \bar{f}_j, \bar{f}^{(m)}$	average value of f, w.r.t. the support of the basis function b_j or the structure m, respectively	16, 46
Ш	train of pulses	16
$\text{Ш} \otimes \mathbf{f}$	pointwise product, $\text{Ш} \otimes \mathbf{f} := (\text{Ш}_1 \mathbf{f}_1, \text{Ш}_2 \mathbf{f}_2, ...)$	16
$d(\bullet, \bullet)$	measure in $\mathbb{R}^n$ of two elements	17
$\|\bullet\|$	Euclidean (Frobenius) norm	17
$\leq$	less or equal to	17
$\sim$	similar to	17, 37
$|\bullet|$	absolute value of	20
$\mathbb{Q}$	rational numbers	20
$\leftarrow$	implements	21, 50, 53, 61
$f * g$	convolution between the functions f and g	22, 30
$\Box$	d'Alembert operator	30
∇^2	Laplace operator	30
$\hat{f}$	Fourier transform of f; $\hat{f}(\omega) := \frac{1}{2\pi} \int_{\mathbb{R}} f(t) \exp(-\hat{\imath}\omega t) dt$	33
$\int_{t_1}^{t_2} \bullet \, dt$	integration of t over the interval $[t_1,t_2]$	34
$k_a, k_d, k_{a,d}$	abstract wave numbers	34

Symbols used in this document.

Symbol	Meaning	Page
D, L, P	distances	36
N, S	objects	36
α	attenuation coefficient	38
$\mathbb{Q}_+$	positive rational numbers	41
Σ	(indefinite) sum operator	46
w_j	j-th singular value (the square root of the j-th eigenvalue)	49
ε	positive real number close to zero	49
dB	decibel	49
$\mathbf{U}, \mathbf{V}$	unitary matrices, i.e. $\mathbf{U}\mathbf{U}^* = \mathbf{I} = \mathbf{U}^*\mathbf{U}$	49
$\mathbf{I}$	identity matrix	49
$\mathbf{W}$	rectangular diagonal matrix, $\mathbf{W} = (\mathbf{W}_{u,v})$, $\mathbf{W}_{u,v} = 0$ for $u \neq v$	49
u	line index	49
v	row index	49
==	equals	50
$\lfloor a \rfloor$	floor function of $a \in \mathbb{R}$ representing the largest integer $\leq a$	53
$\lceil a \rceil$	ceiling function of $a \in \mathbb{R}$ representing the largest integer $\geq a$	53
μ	probabilistic mean	56
σ	standard deviation	56
s	histogram index	63
d_S	measure of entropy	63
h	histogram function, $h : [1, \Gamma] \to [0, J]$	63
Γ	total number of histogram values	63
$\log_2$	base two logarithm	63

Abstract

A challenging issue in photoacoustic image reconstruction is to take into account the presence of acoustically heterogeneous media because it is present in many biomedical applications and it degrades the quality of reconstructed images. The methods for image reconstruction from projections, the most common algorithms used in photoacoustic imaging, are based on a linear transport description. This doctoral thesis addresses the conjecture that the photoacoustic propagation obeys the Heaviside telegraph equation, a consideration based on experimental observations where acoustic perturbations affect the structural integrity of photoacoustic information. For the first time, both attenuation and acoustic dispersion are considered in one photoacoustic transport model. The reconstruction of an image representing the photoacoustic energy absorption map is an inverse problem. We approximate this inversion using a numerical representation of a two-dimensional heterogeneous pressure distribution map of a coronal human breast phantom and four distinct linear wave equations simulating different degrees of signal perturbations. As a result, analytical expressions for blurring and reflection effects in the reconstructed images are achieved. This projection-processing strategy results valuable to improve essentially the quality of the reconstruction and is independent of the choice of method to restore image information from perturbed photoacoustic signals. Based on our analysis, we consider that the proposed methodology has a great potential in non-destructive biomedical imaging. Furthermore, it can be extended to other modalities of waveform tomography, such as acoustical, seismic or optical tomography.

Resumen

Una cuestión desafiante en reconstrucción de imágenes fotoacústicas es tener en cuenta la presencia de los medios de propagación acústicamente heterogéneos ya que están presentes en muchas aplicaciones biomédicas y que degradan la calidad de las imágenes reconstruidas. Los métodos de reconstrucción imágenes a partir de proyecciones, los algoritmos más comunmente utilizados en la creación de imágenes fotoacústicas, están buscando en una descripción de transporte lineal. Esta tesis doctoral aborda la conjetura de que la propagación fotoacústica obedece a la ecuación del telégrafo Heaviside, una consideración con base en las observaciones experimentales en las que las perturbaciones acústicas afectan la integridad estructural de la información fotoacústica. Por primera vez, tanto la atenuación como la dispersión acústica se consideran en un modelo de transporte fotoacústica. La reconstrucción de una imagen que representa el mapa de absorción de energía fotoacústica es un problema inverso. Nosotros aproximamos este proceso de inversión usando un cálculo numérico de un mapa bidimensional de la distribución heterogénea de presión de una imagen de una maqueta que representa una sección coronal de mama humano y cuatro ecuaciones lineales de onda distintas que simulan diferentes grados de perturbaciones de la señal. Como resultado, se obtienen expresiones analíticas para la distorsión y diversos efectos de reflexión en las imágenes reconstruidas. Esta estrategia de procesamiento de proyecciones ha dado resultados rentables para mejorar esencialmente la calidad de reconstrucciones y es independiente del método elegido para restaurar la información de imágenes fotoacústicas. Con base en nuestro análisis, consideramos que la metodología propuesta aquí tiene un gran potencial en imagenología biomédica no-destructiva. Asimismo, se puede extender a otras modalidades de tomografía de forma de onda, tales como la tomografía acústica, sísmicas u óptica.

Preface

Background of the study

This thesis reports on the results of my Ph.D. project on computer science carried out at both the *Centro de Ciencias Aplicadas y Desarollo Tecnológico* (CCADET) and the *Instituto de Investigaciones en Matemáticas Aplicadas y en Sistemas* (IIMAS) of the *Universidad Nacional Autónoma de México* (UNAM). This project is the result of my interest in medical imaging and image processing techniques, in particular in the newly proposed photoacoustic imaging and its application to early cancer detection and therapy. As a result, I carried out my Ph.D. research under the supervision of Dr. Crescencio García Segundo and Dr. Edgar Garduño Ángeles, experts in the fields of photoacoustic imaging and image reconstruction from projections, respectively. My research covered some mathematical aspects of wave transport models and different computational strategies for image reconstruction.

The rationale behind photoacoustic imaging

Since its discovery in 1880 by Alexander Graham Bell, the photoacoustic effect (in essence, the formation of sound following light absorption) has made history in science. However, its non-invasive applications to medical imaging are still in an early stage of development [1, 2]. After data acquisition, an important step in photoacoustic imaging is the reconstruction of the pressure distribution; a process that is obtained through a computational method. Currently, the most popular computational algorithms employed in photoacoustic imaging are based on methodologies developed for other modalities, notably for x-ray computerized tomography where the data acquired by the sensors are modeled as if the signal propagation is linear. In this thesis we follow closely current observations and results, i.a., [3] and

its references, and claim that the photoacoustic phenomenon can be modeled as a linear process only under very specific circumstances: all acoustic perturbations need an analytic description which has to be (pseudo-) invertible. Nowadays, a challenging issue in photoacoustic imaging is to take into account the presence of acoustically heterogeneous media in deeper tissues because after ~2 mm the non-linear signal propagation effects become more prevalent. Consequently, it is necessary to expand the waveform model for heterogeneous media in order to be able to obtain *good* images of deeper layers of biological tissues. The literature on photoacoustics, e.g., [4], reports on the presence of two well-known types of image-degrading phenomena: blurring and internal reflections. However, the analytical description of the acoustic perturbations is generally neglected. This thesis proposes a transport model to approximate the distribution of the mechanical perturbation in the presence of physical heterogeneities that result in degrading phenomena. From the viewpoint of computer science, this is important because it allows the implementation of efficient strategies for image reconstruction, and hence better results; having knowledge of the process that takes place during the data collection process permits reducing degrading artifacts such as blurring.

The focus of this thesis is on suppressing blurring and internal reflections through extending a transport model incorporating a non-linear distribution of information. We demonstrate the goodness of our model using data from a photoacoustic imaging system with a large planar sensor that produces two-dimensional images. The reasons for selecting this type of system are the abundant availability of experimental data, the possibility to consider comparisons to already validated results by other laboratories, and the fast reconstruction outcome because all transport calculations are obtained through signal processing prior to reconstruction. However, it is worth noticing that the sensor shape is of little relevance since diverse transformation equations and a universal reconstruction formula has been demonstrated in [5] for three canonical geometries. Consequently, our proposal can be classified as of general use. The proposed model can be easily extended to higher dimensions; this option is prescinded here, because the experimental validation of the enhanced model for image reconstruction remains to be completed. Our ongoing research addresses the application of the new model for biomedical photoacoustic tomography with specialized sensors and image reconstruction of higher dimensions.

Overview and features of this dissertation

Photoacoustic tomography is a novel promising modality for early breast cancer detection because it provides functional information of physiological processes such as tissue hemoglobin oxygen saturation; i.a., low oxygenation promotes the spreading of breast cancerous cells [6]. The current advancements in the field are presented in Chapter 1. Most methods to produce images from photoacoustic measurements assume a linear approximation of the hybrid transport model combining electromagnetic and ultrasonic waves. The scientific details of forming computerized tomographic images are explained in Chapter 2. We also explain in Section 2.2 the photoacoustic data acquisition process and the transformation of acoustic signals into approximated projection data for near homogeneous transport.

This doctoral thesis focuses on the challenge to reconstruct photoacoustic images under the presence of acoustic perturbations within inhomogeneous tissues. In Chapter 3, we elaborate numerical routines based on linear transport models, capable to describe sufficiently accurately the impact of wave perturbations and approximate photoacoustically acquired data as projections. These are basically analytical approaches, promoting the employment of novel transform methods and algebraic reconstruction techniques. Their algorithmic design is carried out in Chapter 4. By means of two-dimensional computer simulations we demonstrate backprojection solutions to the linearized forward and inverse problems that are inherent to photoacoustic tomography of heterogeneous media. Additional non-linear adjustments on the transport assumptions are taken into account when iteratively reconstructing the source. Empirically, it seems that the predictions of our linear model for heterogeneous media hold in case of photoacoustic imaging of small animals and synthetic gelatinous phantoms with a diameter of a few centimeters that may produce acoustic reflections and image blurring. The improved image transformations for the case of wave perturbations can be realized by projection processing strategies and further rapid (spherical) Radon transform inversion. The proposed methodology turns out to be computational efficient, both in computation time as well as memory requirements; extra costs are assigned only to the preprocessing of measured signals. Additional improvements on artifact minimization are obtained by our iterative reconstruction algorithm incorporating a detector sensitivity map, as demonstrated by an entropy measure of a specific case study. Finally, we discuss the results obtained by our methods and their potential biomedical applications in Chapter 5.

Acknowledgments

First and foremost I offer my gratitude to my supervisors Dr. Crescencio García Segundo and Dr. Edgar Garduño Ángeles whose expertise in physics and bioengineering added considerably to my graduate work. Both supported my career at the UNAM on different, but complementary ways. I draw interdisciplinary benefit of this collaboration. They also stood on my side, understandingly and amicably, during the past four years, when many changes in the working relationship and my private life appeared.

I appreciate the invitation of Crescencio to contribute with the development of my research to the first project of photoacoustic tomography in Mexico. Throughout my studies at the CCADET-UNAM he was always available and encouraged to discuss problems and new trends related to my thesis and derivatives. From the beginning, he helped me to develop important connections to the international society of photoacoustics, i.a., with Wiendelt Steenbergen, Günther Paltauf, Peter Burgholzer, Gerald J. Diebold, Andreas Mandelis, Gerardo Gutierrez. Furthermore, he promoted me as a team-leader of our working group, as the administrator of the *Imaging Science Club* at the CCADET-UNAM, and as a lecturer on mathematics, what influenced my experience at the university a lot.

I thank Edgar for incorporating this interdisciplinary project on photoacoustic tomography to the postgraduate program of computer science at the IIMAS-UNAM. Only in this way, and related to my degree in mathematics at the *Technische Universität Darmstadt*, I managed to create a well-established fundament of my investigation and a fruitful basis for future scientific projects. In particular, Edgar has influenced essentially the strategy of my scientific publications. His attention and precision in proof-reading let me grow in the awareness that the present work is of considerable importance. Moreover, I am grateful for the opportunity to co-manage the renowned seminar of *Señales, Imágenes y Ambientes Virtuales* (SIAV) at the institute.

Chapter 1

Introduction

1.1

Fundamentals of photoacoustics

Photoacoustic signals are the result of the photoacoustic effect, that is, ultrasound generation by pulsed or modulated light absorption of visible to near-infrared wavelengths. This effect was discovered in the nineteenth century and was first mentioned in 1880 by the Scottish researcher Alexander Graham Bell in his work of the *photophone* [7], an optical communication instrument consisting of a voice-activated mirror, a selenium cell, and an electrical telephone receiver; an illustration of a photophone receiver is depicted in Figures 1.1.1 and 1.1.2.
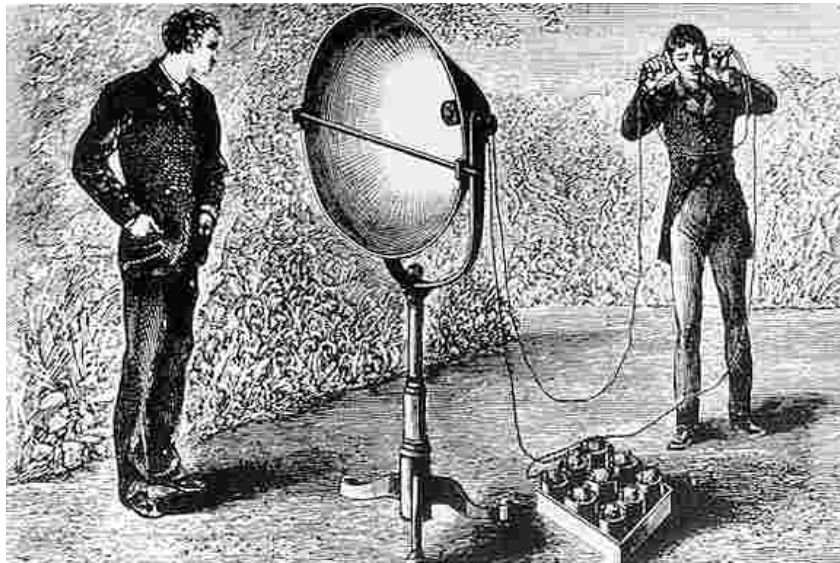
Fig. 1.1.1: One part of Bell's wireless optical communication system: a photophone receiver, circa 1880. Detailed description of the construction can be found in [8]. (Image courtesy of the U.S. Library of Congress, Photo Department.)

The physical mechanism behind the photoacoustic effect takes place through the following stages:

1. Emission of electromagnetic radiation.

2. Conversion of electromagnetic radiation into heat.

3. Temporary changes of temperature occur at the regions of absorption.

4. Thermal expansion and contraction due to pressure changes.

The terms *optoacoustic*, *photothermal* and *thermoacoustic* are synonyms for photoacoustic [3], hence indicate the same physical characteristics, but their effect is possibly generated in distinctively defined frequency ranges.
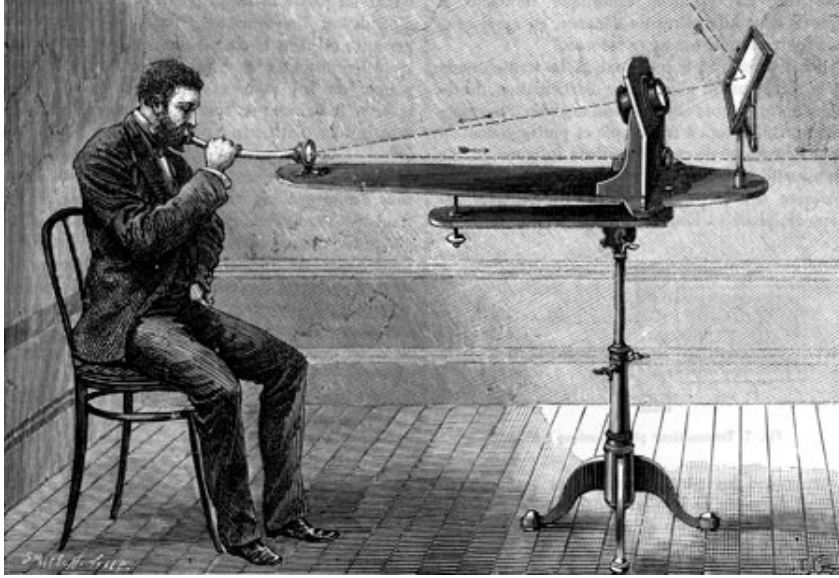
Fig. 1.1.2: Bell's photophone used for talking with reflected sunlight. (Reproduction from the original, received in Washington Post Library on March 4, 1947; image courtesy of the U.S. Library of Congress, Photo Department.)

The model of the absorbed optical energy, when converted to heat, relates the optical absorption to the light fluence [9]. The optical absorption coefficient μ_a quantifies how quickly and effectively radiation is absorbed in a certain medium. Furthermore, the light fluence rate Φ (also referred to as *radiant exposure*) at a given point $\mathbf{x} \in \mathbb{R}^3$ and a given time t is a measurement of energy over an area segment. Accordingly, the heating function H can be written as

$$H(\mathbf{x},t) = \mu_a(\mathbf{x})\Phi(\mathbf{x},t). \tag{1.1.1}$$

Under simplifying assumptions [10] (i.e., considering only absorption effects), the heating function, dependent on the angular frequency ω (or rather the ordinary frequency measured in Hertz times 2π), can be expressed as the following product

$$H(\mathbf{x},t;\omega) = \mu_a(\mathbf{x})I_0 e^{-\hat{\imath}\omega t}, \tag{1.1.2}$$

where I_0 is the initial intensity of light which varies in time in direct proportion to the generated pressure. The changes in pressure originate sound waves that propagate within the sample tissue and can be detected by a sensor coupled directly to it. Assuming a bounded region Ω of homogeneous media, such as biological tissue, the pressure distribution p can be modeled by a linear operator $\mathscr{L}$ in conformity to the following equation introduced in [3]

$$\mathscr{L}p(\mathbf{x},t) := \nabla^2 p(\mathbf{x},t) - \frac{1}{c^2}\frac{\partial^2}{\partial t^2}p(\mathbf{x},t) = -\frac{\Gamma}{c^2}\frac{\partial H}{\partial t}, \tag{1.1.3}$$

where c is the speed of sound and Γ is a dimensionless constant known as the Grüneisen parameter, which indicates the efficiency of the conversion from heat to pressure and is defined as $\Gamma = c^2\beta/C_p$; β is the isobaric volume expansion coefficient and C_p is the specific heat [J / (K · kg)]. The forward solution $p(\mathbf{y},t)$ of the photoacoustic wave equation (1.1.3) at the boundary of the observed region $\mathbf{y} \in \delta\Omega$ can be analytically determined using the Green free-space function G, given the initial pressure distribution $f(\mathbf{x}) = -\Gamma I_0/c^2\mu_a(\mathbf{x})$, as follows

$$p(\mathbf{y},t) = -\frac{\Gamma I_0}{c^2}\int_{\mathbb{R}^n}\mu_a(\mathbf{x})\frac{\partial G(\mathbf{y}-\mathbf{x},t)}{\partial t}d\mathbf{x}, \tag{1.1.4}$$

with the initial conditions

$$\mathscr{L}p(\mathbf{x},t) = 0, \tag{1.1.5}$$

$$p(\mathbf{x},0) = f(\mathbf{x}), \tag{1.1.6}$$

$$\partial_t p(\mathbf{x},0) = 0, \tag{1.1.7}$$

establishing a well-defined linear system. The initial sound pressure distribution $f(\mathbf{x})$ stands in strong relation to the map of light absorption according to the photoacoustic effect, i.e, dense pressure distribution where light is highly absorbed. A typical application of the above model is to solve the following inverse problem:

1. **Given** photoacoustic measurements at the boundary $p(\mathbf{y},t)$.
2. **Find** the initial sound pressure distribution $f(\mathbf{x})$ of the sample.

Its solution creates the conditions to enable *photoacoustic spectroscopy* and its derivations in imaging systems (see Section 1.2). Photoacoustic spectroscopy permits quick and nondestructive testing without

pretreatment or contact with the sample. The measurement sensitivity increases as the light source intensity raises. Specially designed measurements allow the analysis of irregularly shaped samples or surface treatments. Varying the modulation frequency and the wavelength of the probing radiation results in depth profiling of layered or gradient composition.

1.2

Photoacoustic imaging systems

Based on the photoacoustic effect, photoacoustic imaging is classified as a hybrid (optical-acoustical) imaging modality with a great potential for biomedical applications. Its main advantages are the use of non-ionizing radiation to produce images of ultrasonic resolution and electromagnetic absorption contrast. Presently, there are two main imaging systems using this principle: photoacoustic microscopy and photoacoustic tomography. The experimental method to generate the acoustic wave field by pulsed laser light follows the same principle in both systems but differs in the frequency range; consequently, they differ in their penetration depth and their resolution. The scanning and reconstruction strategies also vary between the two approaches.

Photoacoustic microscopy reflects information about the superficial light absorption (< 3 mm deep) typically within the bandwidth from 1 to ~ 50 MHz using a focused ultrasound sensor. Through linear or sector scans, two-dimensional images are generated directly without the need of a reconstruction algorithm. As soon as the light illuminates the sample tissue, ultrasonic scattering is two to three orders of magnitude weaker than optical scattering. Because of the dimensions of the tissue samples studied in photoacoustic microscopy, it is possible to obtain better spatial resolution than in pure optical imaging; a typical lateral resolution is about 50 μm [11]. Figures 1.2.1 and 1.2.2 show a photoacoustic microscopy scanner with an *in vivo* probe of a subcutaneously inoculated melanoma in an immunocompromised naked mouse.

In photoacoustic tomography, one typically acquires signal information with an unfocused ultrasound sensor and uses a radial scanning around the (three-dimensional) object of interest. By inversely solving the transport equations (1.1.5)-(1.1.7) the absorption map of the sample can be computationally reconstructed (typically with a depth up to 5 cm for an incidence frequency of 5 MHz). For this purpose, many photoacoustic measurements (transformed as approximated projection data in accordance to the methods presented in Section 2.2.1) for all mechanically realizable sensing directions are needed as an input for image reconstruction algorithms, which inevitably are memory or time intensive. Due to these computational costs, series of two-dimensional slice images are more common although losses in the resolution represent a considerable drawback. Recently, methods of *compressed sensing* have also been
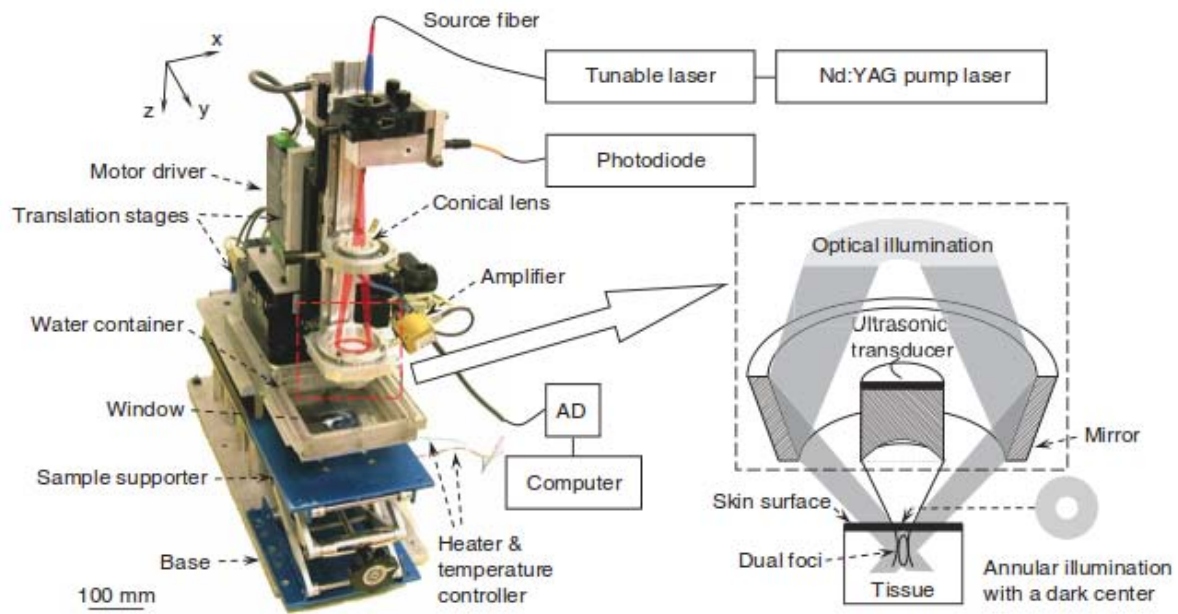
Fig. 1.2.1: The experimental photoacoustic microscopy scanner equipment by Zhang et al. [11]. (Image courtesy of Ph.D. Lihong Wang, Washington University in St. Louis, USA.)
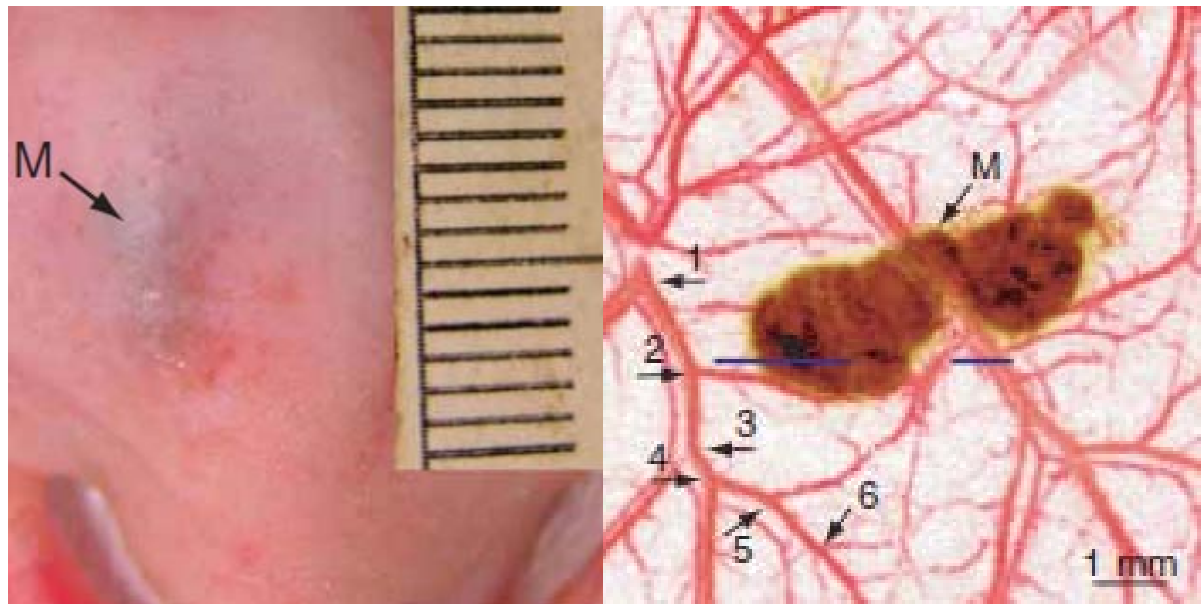
Fig. 1.2.2: *In vivo* imaging of a melanoma (M) 0.32 mm below the skin surface of a naked mouse using photoacoustic microscopy [11]. Left: Photograph of the melanoma. Right: A maximum amplitude projection image, where blood vessels are pseudo-colored red and the melanoma is pseudo-colored brown. As many as six orders of vessel branching can be observed in the image as indicated by the numbers 1-6. (Image courtesy of Ph.D. Lihong Wang, Washington University in St. Louis, USA.)

introduced to photoacoustics to use less projections [12]. These are signal processing techniques that efficiently acquire and reconstruct a signal from few samples (less than required by a traditional interpretation of the Shannon-Nyquist sampling theorem), by finding optimal solutions to underdetermined linear systems. We are aware that the detection problems due to acoustical perturbations become larger as the penetration increases. The sensitivity of the system can be enhanced using specific biocompatible contrast agents with greater optical absorption properties (e.g., nanoparticles). It has been shown in small animals, e.g., a zebrafish [13], that photoacoustic tomographic methods are capable of resolving optical molecular agents, fluorescent proteins, and other reporter agents, thus allowing the investigation of an entire living organism. In Figure 1.2.3 we reproduce from [13] the results of a photoacoustic tomographic procedure, applied on an adult zebrafish, that demonstrate the applicability of this technique.
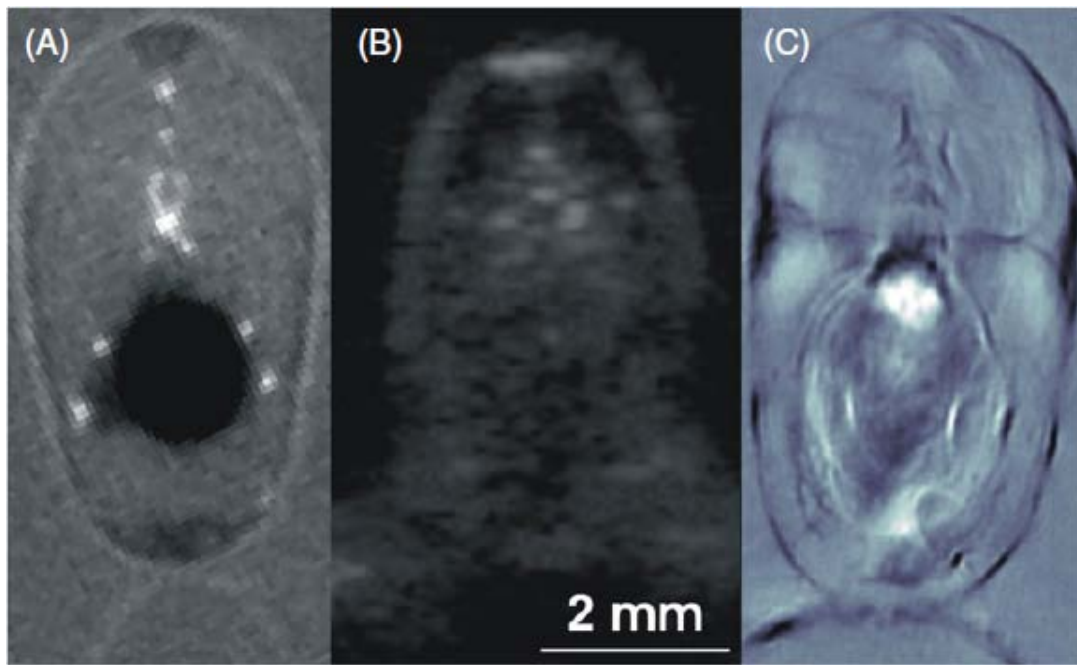
Fig. 1.2.3: Non-invasive cross-sectional imaging of an one-year-old female zebrafish [13]. Comparision between (A) x-ray computerized tomography, (B) ultrasound imaging and (C) photoacoustic tomography. (Image courtesy of Ph.D. Daniel Razansky, Technische Universität München, Germany.)

Scientific studies show that photoacoustic imaging is suited to visualize morphological changes as well as functional and molecular activities in biological tissues. Its applications (predominantly in soft tissues) include cancer developmental biology, small animal imaging, cellular biology, stroke and diabetes study (in particular ischemia). As a consequence, many scientists, such as those in the university of

Twente in the Netherlands, have developed photoacoustic mamoscopes to improve early breast cancer detection, see Figure 1.2.4 for some results obtained with such a device. The imaging possibilities are essentially limited by the electromagnetic penetration and acoustic transport perturbations. In deeper tissues, heterogeneous media acoustic reflection and scattering represent serious limitations because they induce severe artifacts.
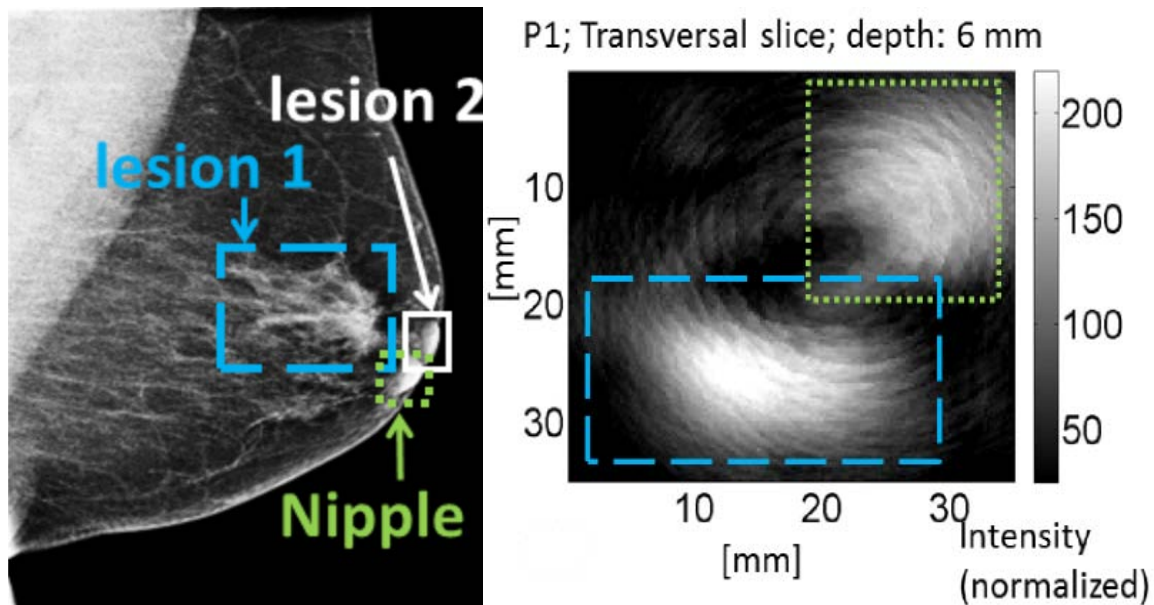
Fig. 1.2.4: Example images from the Twente photoacoustic mamoscope with annotations by the authors of [14]. Left: The cranio-caudal x-ray mammogram of a human breast shows a 20 mm lesion with a calcification. Right: A transversal cross-section with a slice-thickness of 0.24 mm through the photoacoustic volume at the expected lesion. (Image courtesy of Susannah Lehman, The Optical Society of America, and Ph.D. Michelle Heijblom, Universiteit Twente, Netherlands.)

Mathematical methods of computerized tomography

In the present chapter we introduce the basic mathematical concepts of computerized tomography and review the main image reconstruction strategies. Later on, we present the prevailing model for photoacoustic image formation of small specimens in connection with signal processing and specific integrating geometries.

Image reconstruction from projections

The problem of image reconstruction from projections has arisen independently in a large number of scientific fields [15]; all have in common that they solve the problem using methods of computerized tomography. The more popular tomographic modalities are defined via multiple x-ray projections, high-energy photon emission (such as those produced by positron anhiliation), or magnetic resonance. Recently, photoacoustic tomography has been demonstrated to be a version of this specific class of inverse problems [16]. All these technologies have a general mathematical basis: the tomographic concept of projections.

Technically speaking, a projection $\mathscr{P}$ is a mapping of a real-valued function $f : \mathbb{R}^n \to \mathbb{R}$ of some physical property of bounded support, onto a subset $S \subset \mathscr{S}$, where $\mathscr{S}$ is typically a set of hyperplanes; f represents the image to reconstruct. For instance, when dealing with the classical computerized tomography, f refers to the distribution of linear attenuation coefficients, or the Coulomb potential of molecules in electron microscopy; in photoacoustic imaging, f is the initial sound pressure distribution, measured with an acoustic detector (e.g., microphone), which in turn is related to the attenuation of light.

We can specify an $(n-1)$-dimensional hyperplane in spherical coordinates as $S(r, \phi) = \{\mathbf{x} \in \mathbb{R}^n | \langle \mathbf{x}, \phi \rangle = r\}$, perpendicular to ϕ, an element of the unit sphere Φ^{n-1} in $\mathbb{R}^n$. More specifically, $\mathscr{P}$ is a linear transformation of the form

$$(\mathscr{P}f)(r, \phi) = \int_{S(r,\phi)} w(\mathbf{x}, S) \cdot f(\mathbf{x}) d\mathbf{x}, \tag{2.1.1}$$

with a given weighting function (i.e., kernel) $w : \mathbb{R}^n \times S \to \mathbb{R}$. In the particular case of x-ray computerized tomography, all projections for image reconstruction are assumed to be known line or plane integrals, depending on the dimension of the density distribution. For simplicity, it is common to set the weighting function to be constant ($w = 1$). The resulting linear operator is called the (classical) Radon transform,

$$(\mathscr{R}f)(r, \phi) := \int_{S(r,\phi)} f(\mathbf{x}) d\mathbf{x} \approx g(r, \phi), \tag{2.1.2}$$

where g denotes the approximated projection for the orientation (r, ϕ) that we obtained as physical measurements. For integration over curved hyperplanes we speak about the spherical Radon transform; a close analysis of this transform is presented in [18].

The common tomographic aim is to produce the image f using a program that implements an algorithm to calculate the approximate inversion of $\mathscr{P}^{-1}g$. It has been demonstrated in [15] that the inverse Radon transform

$$(\mathscr{R}^{-1}g)(\mathbf{x}) := \int_{\boldsymbol{\Phi}^{n-1}} g(\mathbf{x} \cdot \phi, \phi) d\phi \qquad (2.1.3)$$

is associated with $\mathscr{P}^{-1}$. The same authors also proved that $\mathscr{R}^{-1}\mathscr{R}f = f$ for any real continuous and bounded image f, satisfying the physical reasonable condition of $\mathscr{R}f$ having a continuous first derivative. Generally, there are two basic approaches to reconstruct the image f: *transform methods* and *series expansion methods*. Both reconstruction families made their first appearance in the scientific literature and in the computed tomography scanner industry around 1970. An essential difference between the two families of methods lies in the discretization precedence. Transform methods replace the continuous operators by their discrete counterparts at the very end of the process, whereas the series expansion methods discretize the reconstruction problem from the very beginning, before further mathematical analysis. All computational methods are based on digital assumptions which can be a source of error and may lead to a very inaccurate reconstruction [17].

2.1.1 Transform methods

In practice, all numerical applications demand for discretization, either of the problem description or their results. Transform methods do the latter and approximate the projection operation over Ω by the Radon transform $\mathscr{R}$, a discretized image $\mathbf{f}$ and a finite sequence of projection values $\mathbf{g}$, both represented by column-vectors. Thence, the reconstruction task is stated as

1. **Given** the physically obtained projection estimations $\mathbf{g} \approx \mathscr{R}f$.
2. **Find** a *good* approximation $\mathbf{f}$ to the image f through the inverse operation $\mathscr{R}^{-1}$.

The image $\mathbf{f}$ is discretized by the spatial elements $\mathbf{x}_j$, in the range of $1 \leq j \leq J$; in the following we implement these elements by pixels. For the directions $\phi_1, \phi_2, ..., \phi_K$ of a discrete vector field at every $\mathbf{x}_j$ we may approximate the inversion operation by

$$(\mathscr{R}^{-1}\mathbf{g})(\mathbf{x}_j) \approx \sum_{k=1}^{K} \mathbf{g}_k(\mathbf{x}_j \cdot \phi_k, \phi_k). \tag{2.1.4}$$

The graph of projections $(\mathbf{g}_1, \mathbf{g}_2, ..., \mathbf{g}_K)$ versus incidence direction is also referred to as the *sinogram*, which represents the Radon transformed image at the corresponding orientations $(\phi_1, \phi_2, ..., \phi_K)$. Since $\mathscr{R}^{-1}\mathscr{R}f = f$, we expect that its discrete version $\mathscr{R}^{-1}\mathscr{R}\mathbf{f} = \mathbf{f}'$ should result in a *good* approximation $\mathbf{f}'$ to the original f.

Much of the theory of the Radon transform follows from its behavior under the Fourier transform and convolution [19]. The *central slice theorem* provides the starting point to various analytic transform methods, as summarized in [20]. Thus, the inverse Radon transform can alternatively be obtained, for example, through the operation

$$\mathscr{R}^{-1} = -\frac{1}{2\pi}\mathscr{B}\mathscr{H}\mathscr{D}, \tag{2.1.5}$$

by the backprojection $(\mathscr{B}p)(r, \phi) = \int_0^{\pi} p(r\cos(\theta - \phi), \theta)\ d\theta$ of the Hilbert transform $(\mathscr{H}p)(r, \phi) = -\frac{1}{\pi}\int_{-\infty}^{\infty} p(l, \phi)/(r - l)\ dl$ (evaluated in the sense of the *Cauchy principal value theorem*) and partial differentiation $(\mathscr{D}p)(r, \phi) = \lim_{\delta r \to 0}(p(r + \delta r, \phi) - p(r, \phi))/\delta r$. Depending on the imaging geometry as well as on the quality and the quantity of the projection data, the replacement of the Radon operator and, moreover, their discretizations may yield better reconstruction results in practice than with the operator itself; further implications of possible replacements are discussed in [15].

Any pure transform method works well with noiseless data for all projections and hyperplanes. However, no real application satisfies this assumption for the experimentally obtained projection data. Transform methods have to perform on finite and imperfect data using the limited capabilities of computers [15]. Although computationally more time-efficient and straightforward to implement, the backprojection algorithms are unfortunately very prone to imaging artifacts; errors in the projections spread to the overall reconstruction when no further correction procedures are implemented. In essence, what needs to be done is to develop numerical procedures that are able to deal with noise and limited data.

2.1.2 Series expansion methods

Series expansion methods include methods such as the *algebraic reconstruction techniques* (ART), *Kaczmarz procedure*, *iterative algorithms*, or *optimization theory techniques* which are immediately applicable to many forms of data collection and have the advantage that can incorporate repeatedly correction pro-

cedures (unlike transform methods). The basic principle behind these methods is that a discrete image $\mathbf{f}^{\otimes}$ of the original f can be approximated by a linear combination of basis functions $b_1, b_2, ..., b_J$,

$$\mathbf{f}^{\otimes}(r, \phi) := \sum_{j=1}^{J} \bar{f}_j b_j(r, \phi), \tag{2.1.6}$$

where $\bar{f}_j$ is the average value of f on the support of the basis function b_j; for piecewise basis functions holds $\mathbf{f}^{\otimes} \approx \mathrm{III} \otimes f$, the pointwise product of the continuous image f with a *train of pulses* III. A common choice for a basis function, but by far not the only one, is the following

$$b_j(r, \phi) = \begin{cases} 1 & \text{if } (r, \phi) \text{ is inside the } j\text{-th pixel,} \\ 0 & \text{else.} \end{cases} \tag{2.1.7}$$

However, it has been argued that basis functions with such sharp transitions are not the most appropriate; hence, other basis functions with smooth transitions from 1 to 0 have been proposed [15]. Later, we suggest a novel non-linear photoacoustic implementation of a basis function in Section 4.4.

As easily deduced from (2.1.4), the Radon transform can be approximated by the series of (pseudo-) invertible matrices $(\mathbf{R}_k)$ for every projection in direction ϕ_k. These Radon functionals present special characteristics such as

- linearity, i.e., $\mathbf{R}_k(\gamma_1 \mathbf{f}_1 + \gamma_2 \mathbf{f}_2) = \gamma_1 \mathbf{R}_k \mathbf{f}_1 + \gamma_2 \mathbf{R}_k \mathbf{f}_2$,
- continuity, i.e., for $\mathbf{f}_1 \approx \mathbf{f}_2$ holds $\mathbf{R}_k \mathbf{f}_1 \approx \mathbf{R}_k \mathbf{f}_2$.

Accordingly, the translation of the continuous projection into a discrete one is as follows

$$\mathbf{R}_k \mathbf{f}^{\otimes} = \sum_{j=1}^{J} \bar{f}_j \mathbf{R}_k b_j \approx \mathbf{g}_k, \tag{2.1.8}$$

where $\mathbf{R}_k b_j$ can be efficiently calculated because the basis functions are defined *a priori*. The approximation in (2.1.8) due to inaccurate measurements leads to the summed error description $\mathbf{e} = \sum_{k=1}^{K} \mathbf{e}_k$ of the reconstruction, involving the error of each backprojection $\mathbf{e}_k$ (including linear and nonlinear parts),

$$\mathbf{f}^{\otimes} = \mathbf{R}_k^* \mathbf{g}_k + \mathbf{e}_k. \tag{2.1.9}$$

Usually, the discrete reconstruction task will not reveal a unique solution since the system of equations (componentwise) (2.1.9) is undetermined. Hence, series expansion methods try to find the *nearest* esti-

mation of $\mathbf{R}_k^* \mathbf{g}_k$ to the discrete image $\mathbf{f}^\otimes$. This approach requires the definition of a distance between two images, which is also crucial for the problem of how to treat noise and limited data. The widely used ART procedure chooses *least squares* as an appropriate measure d,

$$\mathbf{e}_k = d(\mathbf{R}_k^* \mathbf{g}_k, \mathbf{f}^\otimes) := \|\mathbf{R}_k^* \mathbf{g}_k - \mathbf{f}^\otimes\|^2, \tag{2.1.10}$$

where $\|\cdot\|$ denotes the Euclidean norm. Others express the error in relation to an optimization criterion, e.g., *maximum likelihood estimation*, *total variation*, and many more [15], and focus on its minimization.

All series expansion methods are iterative procedures and produce a sequence of images $\mathbf{f}_1, \mathbf{f}_2, \ldots$ that is supposed to converge to $\mathbf{f}^\otimes$. The flexible ART procedure, operates sequentially on one of the K orthogonal projections $\mathbf{P}_k$ onto the affine subspace $\mathbf{R}_k \mathbf{f}^\otimes = \mathbf{g}_k$ in $\mathbb{R}^n$, given by

$$\mathbf{P}_k \mathbf{f}^{(l)} := \mathbf{f}^{(l)} + \mathbf{R}_k^* (\mathbf{R}_k \mathbf{R}_k^*)^{-1} (\mathbf{g}_k - \mathbf{R}_k \mathbf{f}^{(l)}), \tag{2.1.11}$$

where $\mathbf{f}^{(l)}$ is a previous estimation of the image f (which may be initially the zero image vector). One iterative step is explicitly described by setting $\mathbf{f}_1^{(l)} := \mathbf{f}^{(l)}$ and computing $\mathbf{f}_i^{(l)}$, with $1 \leq i \leq I$, according to

$$\mathbf{f}_{i+1}^{(l)} := \mathbf{P}_k \mathbf{f}_i^{(l)} = \mathbf{f}_i^{(l)} + \frac{\mathbf{g}_{k_i} - \langle \mathbf{R}_{k_i}, \mathbf{f}_i^{(l)} \rangle}{\langle \mathbf{R}_{k_i}, \mathbf{R}_{k_i} \rangle} \mathbf{R}_{k_i}^T, \qquad 1 \leq i \leq I \tag{2.1.12}$$

$$\tag{2.1.13}$$

where $\mathbf{R}_{k_i}$ is the i-th row of the matrix $\mathbf{R}_k$, which in turn represents the projection in the k-th direction; respectively, $\mathbf{g}_{k_i}$ is the i-th entry of the vector $\mathbf{g}_k$. Then, $\mathbf{f}^{(l+1)} := \mathbf{f}_I^{(l)}$. This algorithm (without relaxation) will converge (slowly, in comparison to transform methods), if the condition that the product of the matrix and its complex conjugate $\mathbf{R}_k \mathbf{R}_k^* > 0$ is a positive definite matrix is fulfilled for all $1 \leq k \leq K$ [19]. Hence, $d(\mathbf{f}^{(l+2)}, \mathbf{f}^{(l+1)}) \leq d(\mathbf{f}^{(l+1)}, \mathbf{f}^{(l)})$, and the error $\|\mathbf{e}\|$ becomes smaller. Different convergence properties can be observed by variations of the ART algorithm, e.g., relaxation (additive ART) may improve the total count of iterative steps [15].

2.2

Prevailing photoacoustic image formation

It is possible to think of photoacoustic tomography as a modified computerized tomography modality that is based on acoustic wave propagation instead of electromagnetic radiation. Such a wave is produced via the photoacoustic effect within small specimens by pulsed laser light, e.g., a neodymium-doped yttrium aluminum garnet (Nd:YAG) pulse at ~ 5 ns time-width. Photoacoustic applications with a Nd:YAG laser permit the variation of the frequency bandwidth from 1 to ~ 50 MHz. The laser is typically placed in front of a water basin containing the immersed object of interest, as illustrated in Figure 2.2.1. As in common tomographic systems, the specimen is mounted on a turnable support frame.
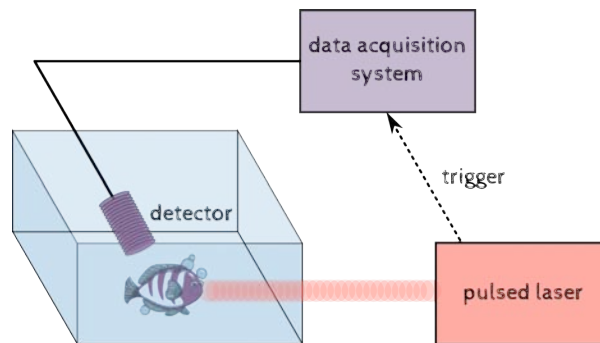
Fig. 2.2.1: Schematic illustration of a typical photoacoustic imaging setup with its basic components. The subject under study is a zebra fish which is commonly used because of its relative transparency and because of its large usage as an animal model in biology research.

Photoacoustically visible are the sensor itself, specific fluorescence molecules [21], and other light absorbing and sound emitting probes; biological light absorbing objects include, to a large extend, soft, thin or homogeneous tissues. These objects respond to the laser pulses with almost planar ultrasound waves. Their wavelengths response range from 0.03 mm to 1.5 mm with a temporal length of ~ 200 ns. The acoustic signals are captured by specific sensors, positioned on the perimeter of the sample and also immersed in water. The magnitude of the photoacoustic signals mostly depends on the following three factors: the composition and thickness of the probe as well as the bandwidth admittance of the sensors. Larger admittance implies higher image quality; however, also more sensitivity to environmental noise.

2.2.1 From acoustic signals to approximated projection data

No matter what tomographic image reconstruction technique, all require the acquisition of quasi ideal projection data of the specimen. In photoacoustic sensing, the captured signals are oscillating acoustic measurements, with positive and negative phases, as illustrated in Figure 2.2.2, that cannot be interpreted as line-integrals (or curve-integrals) over the object. We demonstrated in [22] that signal analysis is essential for further investigations. A processing strategy can be applied to convert the photoacoustic response into a purely positive and normalized function, that, in turn, may be considered as projection data. The decision of what strategy is best suited for photoacoustic signals and tomographic purposes is still an open problem. Authors in [23] pointed out the convenience of the absolute Abel transformation $\mathscr{A}$ of the pressure signal $\mathbf{p}_k$, defined as follows with the new discretization variable $i \in \{1,...,I\}, I \in \mathbb{N}$

$$(\mathscr{A}\mathbf{p}_k(t))(i) = \int_0^i \frac{|\mathbf{p}_k(t)|}{\sqrt{i-t}} dt \approx \mathbf{g}_k(i), \tag{2.2.1}$$

over the use of the envelope function (a smooth curve outlining the extremes), the mean effective pressure (low-pass filtering) and rectifications (converting alternating to positive signals as is common practice in electrical science). However, this observation requires further study in order to obtain stable routine conditions. All mentioned signal processing methodologies are conventional for the treatment of data from any other waveform sources. How these affect unidimensional photoacoustic measurements $\mathbf{p}_k$ is illustrated in Figures 2.2.2-4. For further image reconstruction purposes we decide to approximate projection data by the results of Algorithm 2.2.1 below. This computational method has as input the photoacoustic signals $\mathbf{S}$ (a $K \times I$ data matrix, where $\mathbf{S}_{k,.}$ is the k-th row of $\mathbf{S}$) registered by an oscilloscope over the given discrete interval $\mathbf{time} = \{start,...,end\}$ in $\mathbb{Q}$ (outside this interval $\mathbf{p}_k(t) = 0, \forall k \in \{1,...,K\}, \forall t \in \{start,...,end\}$). The projection data is approximated in line 7 of the pseudocode by the Abel transformed signal as given in equation (2.2.1). The output represents the projection approximation $\mathbf{G}$ (a $K \times I$ data matrix) in every k direction. The procedure **normalize** represents the standard min-max normalization, i.e., the amplitude is scaled with the maximum intensity value equal to one and the minimum intensity value equal to minus one. The **detrend** procedure removes the mean value or linear trend from the photoacoustic scan. This is done by computing the least-squares fit of a straight line to the data and subtracting the resulting function from the data.

Algorithm 2.2.1: PHOTOACOUSTIC SIGNAL PREPROCESSING ($\mathbf{S}$, **time**)

---

1   **main**

2   **for**   k $\leftarrow$ 1 **to** K

3      $\mathbf{s} \leftarrow \mathbf{S}_{k,\cdot}$

4      $\mathbf{d} \leftarrow$ **normalize**($\mathbf{s}$)

5      $\mathbf{p} \leftarrow$ **detrend**($\mathbf{d}$)

6   **for**   i $\leftarrow$ **time**($start$) **to** **time**(end)

7        $\mathbf{p}'(i) \leftarrow \sum_{t=0}^{i} \frac{|\mathbf{p}(t)|}{\sqrt{i-t}}$

8      $\mathbf{g} \leftarrow \mathbf{p}' * \mathbf{p}'$

9      $\mathbf{G}_{k,\cdot} \leftarrow \mathbf{g}$

10   **output** $\mathbf{G}$

2.2.2 Acquisition geometries

The aim of the photoacoustic imaging technique is to reconstruct the initial pressure distribution map given projection information of the object. In this work we obtain projection data by one of the afore-mentioned strategies, but we still need to figure out the acquisition geometry of information integration. The shape of sensors determines how the approximate information integration takes place. When projections are obtained by integration over (flat) hyperplanes (like the large planar sensors sketched as an oblong detector element in Figure 2.2.5a) the inverse problem gets solved by inverting the classical Radon transform of the measured data $\mathbf{g}_k$ as stated in Section 2.1. In fact, a similar approach has been successfully used by the authors of [23] who use a cylindrical detector. In the case of an approximate point sensor, as indicated by a circular detector element in Figure 2.2.5b, the reconstruction of the initial pressure distribution map requires the integration over spheres. For this geometry, the forward projection is modeled using the inversion of the spherical Radon transform reported in [18].

For the sake of illustrating reconstruction qualities and for further comparisons with a realistic case study, we mimic in Figure 2.2.6a the two-dimensional schematic light absorption map of an axial cross-section of the zebra-fish obtained in [23] by analog geometrical objects and simulate the plane wave transport within this phantom; the assigned values from $[0,1] \cap \mathbb{Q}_+$ are chosen to illustrate, by gray scales, different absorption coefficients. Dark gray values $(0.5,1]$ specify regions of high electromagnetic
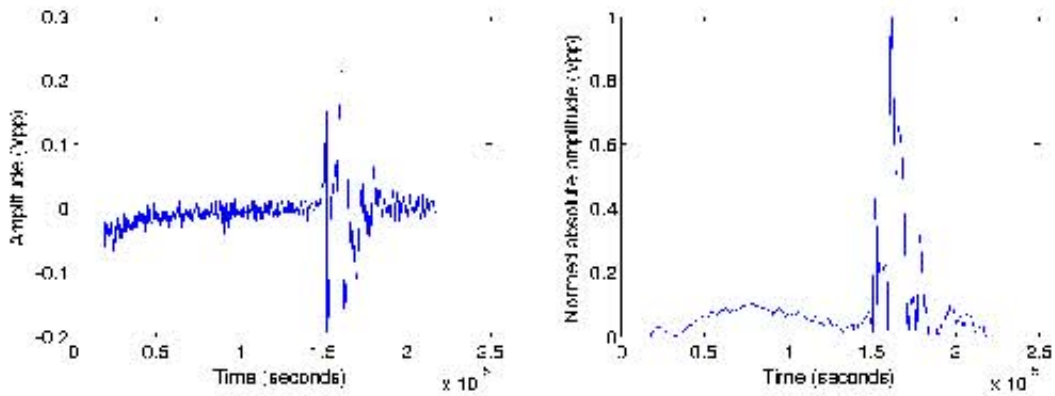
Fig. 2.2.2: Photoacoustic signal processing to obtain an approximation of projection data $\mathbf{g}_k$. Left: A photoacoustic measurement of a real zebra-fish (raw data). Right: Absolute Abel transformed data.
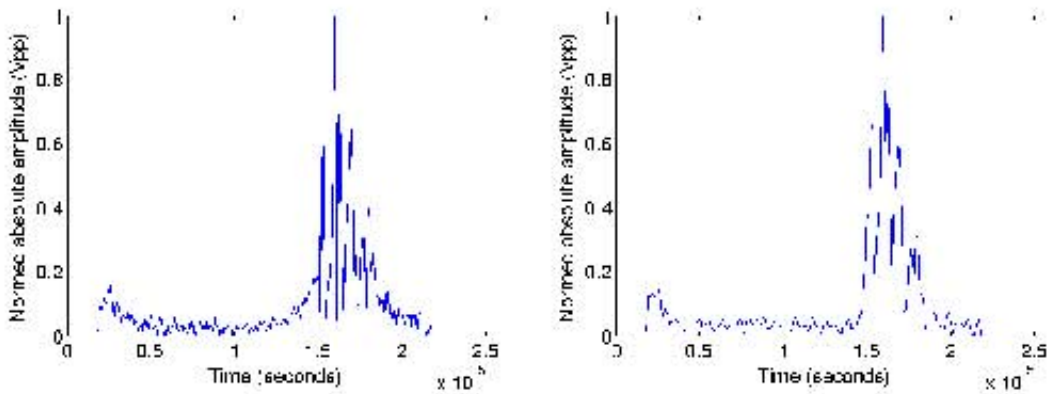
Fig. 2.2.3: Photoacoustic signal processing of the measurement of Figure 2.2.2 using the envelope function $\text{env}(\mathbf{p}_k) = |\mathbf{p}_k - \hat{\imath}\mathcal{H}(\mathbf{p}_k)|$ (left) and the mean effective pressure over an ε-neighborhood (right) as an approximation of projection data $\mathbf{g}_k$.
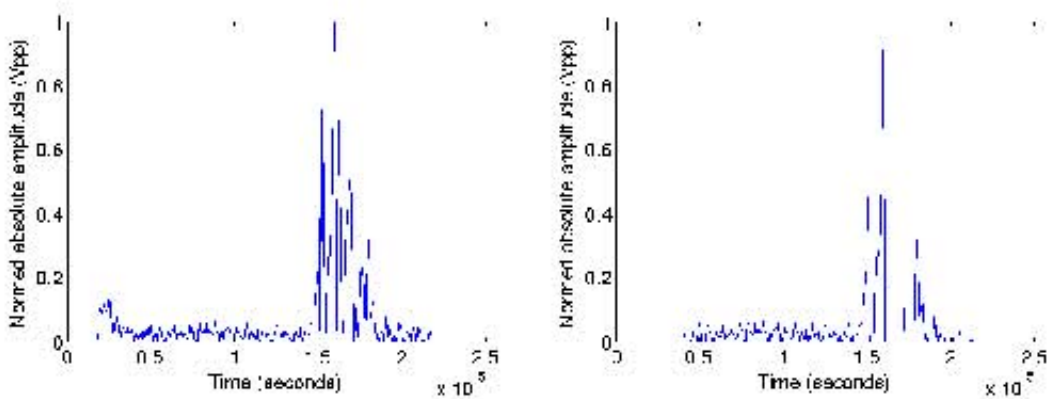
Fig. 2.2.4: Photoacoustic signal processing of the measurement of Figure 2.2.2 using full rectification $\mathbf{g}_k \approx |\mathbf{p}_k|$ (left) and half rectification $\mathbf{g}_k \approx \mathbf{p}_k$ if $\mathbf{p}_k > 0$, else 0 (right).

(a) Large planar sensor (b) Point-like sensor
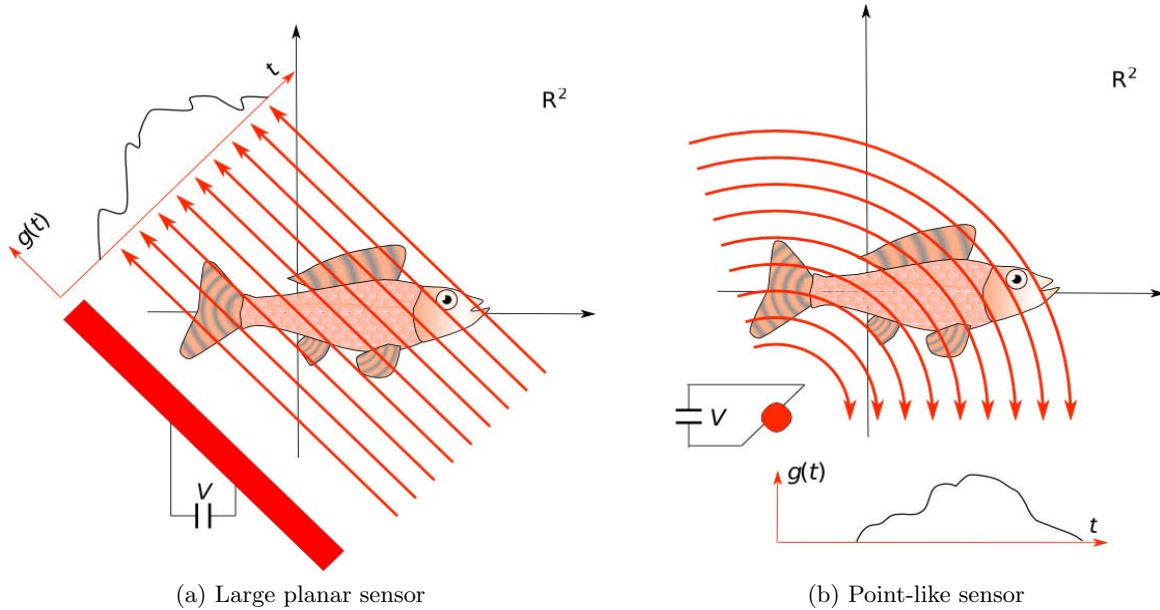
Fig. 2.2.5: Common integrating geometries in photoacoustic imaging using a fish as a specimen. We show (a) a large planar sensor with a red oblong detector element, and (b) a point-like sensor with a circular detector element (illustrated as a red point).

energy absorption, e.g., the pelvic fins, and light gray values $[0, 0.5]$ refer to poor absorption, e.g. in water. The absorption map approximates the initial sound pressure distribution according to the photoacoustic effect (see Section 1.1). We calculate a total of 180 projections, represented in the sinogram in Figure 2.2.6b, each with 400 parallel line integrals, equally distributed over the half-circle, e.g., using the Radon transform of the phantom.

In this case, we try to reconstruct the phantom from the set of projections calculated by the computer simulation. Transforming the sinogram with the inverse Radon operator yields an approximation of one of its cross-sections. This algorithm is also known as *Delay-and-Sum* (alternative reconstruction approaches have been discussed in Section 2.1). The result by backprojecting the data is displayed in Figure 2.2.7a. By the signal analysis of biomedical photoacoustic measurements in time and frequency domains [48] we understood that the sensed data contain an error that may be approximated by using an additive Gaussian white noise. In our laboratory we have tested different piezoelectric sensors and measured their ambient noise in water with a signal-to-noise ratio (SNR) of 14 dB, a mean of $\mu = 0.1$ and a standard deviation of $\rho = 0.004$. These numerical observations are very similar to what Mandelis et al. published for time and frequency domains [48]. The reconstruction with this noise is shown in Figure 2.2.7b.

(a) Zebra-fish phantom
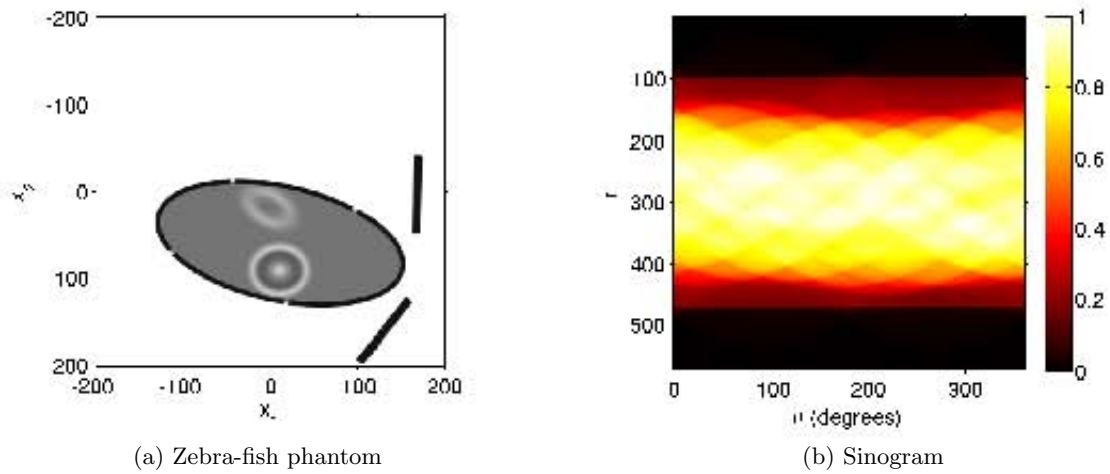
(b) Sinogram

Fig. 2.2.6: (a) A phantom digitalized by 400×400 pixels illustrating the musculoskeletal and digestive atlas of an axial cross-section of a zebra-fish; dark gray levels represent regions of high electromagnetic energy absorption. (b) Sinogram obtained from the phantom for 180 noise-free projections with 400 line integrals and an angular displacement of 1 degree.

(a) Noise-free backprojection

(b) Noisy backprojection
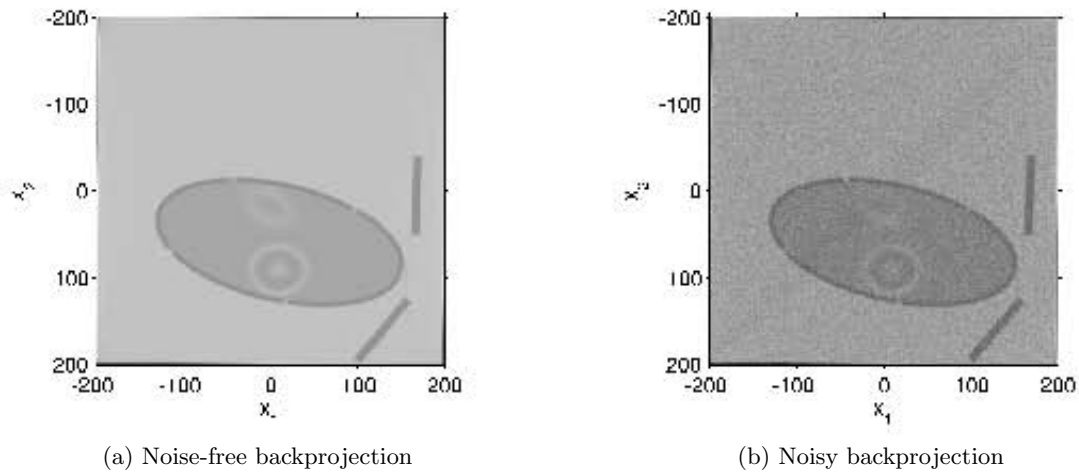
Fig. 2.2.7: (a) Reconstruction of the phantom given noise-free projections. (b) Backprojection of data with a SNR of 14 dB.

To test our methodology on real photoacoustic data, a group of physicists from the Karl-Franzens Universität in Graz, Austria measured a cross-section of a zebra-fish with 400 photoacoustic scans with an cylindrical detector (i.e. a parallel integrating geometry), every $0.9°$ over $360°$, and kindly provided them to us. To obtain the reconstructed cross-section of the zebra-fish [23] we followed the procedure described earlier: The pressure quantification is absolute Abel transformed to obtain the sinogram in Figure 2.2.8a; by backprojecting this photoacoustic projection approximation we reconstruct the zebra-fish cross-section in Figure 2.2.8b.

(a) Sinogram   (b) Backprojection
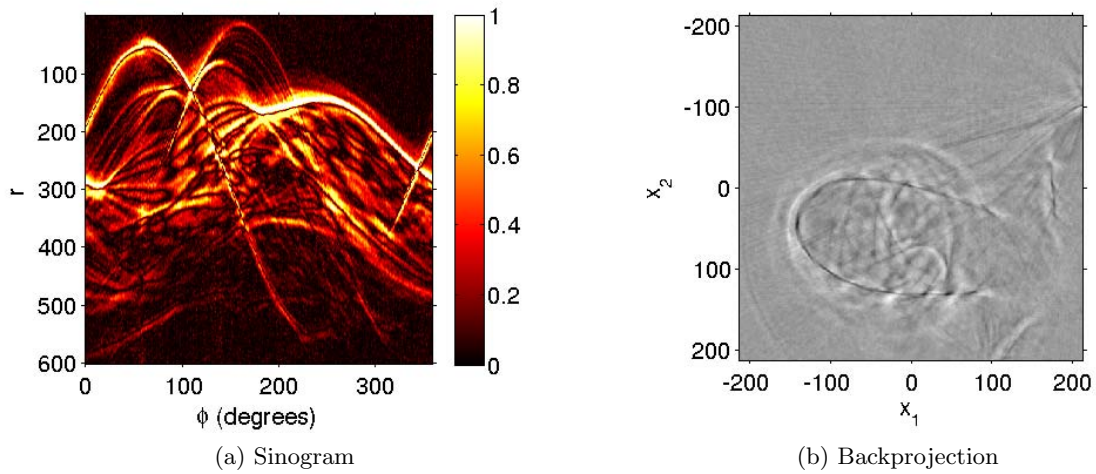
Fig. 2.2.8: (a) Sinogram of photoacoustic measurements absolute Abel transformed. (b) Backprojection of the zebra-fish cross-section

Inverse problems in heterogeneous media

This chapter pays close attention to inverse problems in heterogeneous media. We provide a series of four transport models for the broader domain of waveform tomography, which comprises photoacoustic imaging. These models offer a way for analysing the nature of signal perturbations. Since the considerations involving heterogeneous media do not represent a (linear) projection scheme, alternative solution strategies to the photoacoustic inverse problem are indispensable. We present three numerical approximations that lead to an intrinsic representation of photoacoustic line integrals. In the final section we outline the specimen manufacturing process that allows us to control experimental model conditions.

3.1

Transport models for waveform tomography

A challenging issue in photoacoustic imaging is to take into account the presence of acoustically heterogeneous media because such characteristic is present in many biomedical applications. In particular, much attention is paid on reducing image artifacts in a reconstructed image resulting when imaging a thick tissue representing acoustically heterogeneous and perturbing media. Much of the research about this topic in recent years has focused on minimizing either blurring or defects related to reflections and scattering of acoustic waves; all these imaging defects are non-linear in nature. Efforts range from experimental procedures [3, 25, 26] to computational algorithms on error minimization, in particular, when the plane wave transport is used as a first approximation [4, 27, 28]. Most algorithmic contributions are focused on eliminating attenuation at the very beginning of the computational process, before managing the image formation [29, 30].

Among all current works, one thing remains clear: the photoacoustic transport model still fails to account satisfactorily for recorded artifacts caused by heterogeneous media when working with tissues at considerable depth [26, 30]. Like in most imaging systems, even with contrast agents [31], attenuation considerations or sophisticated reconstruction algorithms, it is still impossible to completely eliminate artifacts and noise. It is worth noticing that sound dispersion is a factor which is generally neglected. This is what led us to review waveform tomography concepts in search for adequate model extensions that could explain the non-linear signal deviation, e.g., shifts and compressions in the frequency domain. For the purpose of tomographic image reconstruction from physically-obtained measurements, we restrict our work to signal-processing, linear transport approximations and model projections.

As mentioned in Section 1.1, the linear photoacoustic transport is well described by $\mathscr{L}p(\mathbf{x},t) = 0$ in (1.1.5), together with the Cauchy conditions $p(\mathbf{x},0) = f(\mathbf{x})$ and $\partial_t p(\mathbf{x},0) = 0$. This system of equations represents a general model which is valid and defined for the broader domain of simple waveform transport comprising acoustic, optical, and electromagnetic modalities. In what follows we provide a summary of distinct waveform transport analyses for the specific linear operator $\mathscr{L} : \Omega \times [t_1,t_2] \to \mathbb{R}_+$ for non-negative real-values t_1, t_2 that describes a linear differential equation of second order in the presence, or absence, of minor derivatives.

Photoacoustic imaging of homogeneous and non-attenuating media, such as that of small animals or breast tissue, is commonly based on a plane wave transport [3] and modeled by the linear d'Alembert operator $\Box$, a generalization of the Laplace operator ∇^2, that includes the constant wave speed c,

$$\mathscr{L}_0 p_0 := \Box p_0 = (\partial_t^2 - c^2 \nabla^2) p_0. \tag{3.1.1}$$

From now on, we denote the linear operator $\mathscr{L}$, the pressure distribution function p, the image data f and the registered projection data g with an index in order to distinguish each model from the others.

The transport of ultrasound is closely related to the above model, generally described in terms of the Helmholtz operator as in [32],

$$\mathscr{L}_a p_a := \Box p_a + a * p_a, \tag{3.1.2}$$

where $*$ denotes the convolution between two functions. Equation (3.1.2) expresses an augmented wave by means of a weight function $a(t)$ acting on the transport; for experimental applications, this weight function can be estimated by optimizing the set

$$\{ a : [t_1, t_2] \to \mathbb{C} \mid \min_t \| a(t) * g(t) + \partial_t^2 g(t) \| \}. \tag{3.1.3}$$

The set in (3.1.3) is chosen to fulfill the system requirements and contains implicit information about the presence of acoustic heterogeneities. The model (3.1.2) has served to include an acoustic attenuation approximation into the photoacoustic transport [29] following the recognized need of incorporating inhomogeneities into the model for various biomedical applications of photoacoustic tomography [33].

Optical tomography describes the radiation inside a body using the Boltzmann transport equation [34, 35]. Under this model, the pressure distribution is a solution to the following wave equation

$$\mathscr{L}_d p_d := \Box p_d + d * \partial_t p_d, \tag{3.1.4}$$

where d is a weight function for the gradient transport. The importance of this dispersion approximation becomes more evident when there are heterogeneities having considerable impact on the optical radiation effects. Appropriate weights can be estimated by optimizing the set

$$\{ d : [t_1, t_2] \to \mathbb{C} \mid \min_{t \in [0,T]} \| d(t) * \partial_t g(t) + \partial_t^2 g(t) \| \}. \tag{3.1.5}$$

Because we are interested in photoacoustic tomography from heterogeneous media, we would like to extend the diffusive wave equation of (3.1.4) by incorporating the attenuation approach of (3.1.2), as described by the Heaviside telegraph equation [36], as follows

$$\mathscr{L}_{a,d} p_{a,d} := \Box p_{a,d} + d * \partial_t p_{a,d} + a * p_{a,d}. \tag{3.1.6}$$

This operator combines wave enhancement with diffusive attenuation and we believe that it represents a more realistic and universal transport description than the photoacoustic model of (3.1.1). Although it is possible to choose the perturbation functions a and d from the finite sets (3.1.3) and (3.1.5), respectively, so they meet some *a priori* criteria, e.g., constant perturbation, a more realistic alternative is to select these functions by applying empirical methods; in Section 3.3 we give some examples.

3.2

Solution strategies in the presence of acoustic heterogeneities

In the presence of acoustic heterogeneities, the inversion of the photoacoustic perturbations within the object of interest represents the main difficulty in the task of tomographic image reconstruction. Ammari presented in [29] a practical strategy to numerically solve the photoacoustic inverse problem with an attenuation approximation, in a similar way to the operator $\mathscr{L}_a$ of (3.1.2). His method describes a signal preprocessing of the boundary measurements such that the impact of attenuation within the media tends to disappear. In this way, the conventional image reconstruction algorithms, such as backprojection, remain applicable for processed projection information.

We follow an analog approach to [29] by modeling the photoacoustic transport with a sound dispersion approximation with the operators $\mathscr{L}_d$ of (3.1.4) and $\mathscr{L}_{a,d}$ of (3.1.6). Our reference is the wave equation of (1.1.5) under the consideration of the initial conditions presented in (1.1.6) and (1.1.7) as well as under the *Duhamel's principle*. We proceed by taking its Fourier transform (symbolized by $\hat{\cdot}$ and defined as on page XVI) in terms of the frequency-dependent pressure and consider the following four cases:

1. Plane wave transport ($\mathscr{L} = \mathscr{L}_0$) in accordance to the model of (3.1.1),

$$(c^2\nabla^2 + \omega^2)\hat{p}_0(\mathbf{x}, \omega) \overset{\mathscr{L}=\mathscr{L}_0}{=} \frac{\hat{\imath}\omega}{\sqrt{2\pi}}f(\mathbf{x}). \tag{3.2.1}$$

2. Plane wave transport with the presence of acoustic attenuation ($\mathscr{L} = \mathscr{L}_a$) in accordance to the model of (3.1.2),

$$(c^2\nabla^2 + \omega^2 - \hat{a}(\omega))\hat{p}_a(\mathbf{x}, \omega) \overset{\mathscr{L}=\mathscr{L}_a}{=} \frac{\hat{\imath}\omega}{\sqrt{2\pi}}f(\mathbf{x}). \tag{3.2.2}$$

3. Plane wave transport with the presence of acoustic dispersion ($\mathscr{L} = \mathscr{L}_d$) in accordance to model of (3.1.4),

$$(c^2\nabla^2 + \omega^2 - \hat{\imath}\omega\hat{d}(\omega))\hat{p}_d(\mathbf{x}, \omega) \overset{\mathscr{L}=\mathscr{L}_d}{=} \frac{\hat{\imath}\omega}{\sqrt{2\pi}}f(\mathbf{x}). \tag{3.2.3}$$

4. Plane wave transport with the presence of attenuation and dispersion ($\mathscr{L} = \mathscr{L}_{a,d}$) in accordance to the model of (3.1.6),

$$(c^2 \nabla^2 + \omega^2 - \hat\imath \omega \hat{d}(\omega) - \hat{a}(\omega)) \hat{p}_{a,d}(\mathbf{x}, \omega) \overset{\mathscr{L}=\mathscr{L}_{a,d}}{=} \frac{\hat\imath \omega}{\sqrt{2\pi}} f(\mathbf{x}). \tag{3.2.4}$$

In conformity with the previous equations, we derive the measurements at the boundary for $\mathbf{y} \in \delta\Omega$ in the Fourier space and consider the following system of equations comparing the homogeneous with the heterogeneous case

$$\hat{g}_0(k_a(\omega)) = \frac{k_a(\omega)}{\omega} \hat{g}_a(\omega), \tag{3.2.5}$$

$$\hat{g}_0(k_d(\omega)) = \frac{k_d(\omega)}{\omega} \hat{g}_d(\omega), \tag{3.2.6}$$

$$\hat{g}_0(k_{a,d}(\omega)) = \frac{k_{a,d}(\omega)}{\omega} \hat{g}_{a,d}(\omega), \tag{3.2.7}$$

where $g_0(t) = p_0(\mathbf{y}, t)$, $g_a(t) = p_a(\mathbf{y}, t)$, $g_d(t) = p_d(\mathbf{y}, t)$, and $g_{a,d}(t) = p_{a,d}(\mathbf{y}, t)$ are valid in $\mathbb{R}^n$ and

$$k_a(\omega) := \sqrt{\omega^2 - \hat{a}(\omega)}, \tag{3.2.8}$$

$$k_d(\omega) := \sqrt{\omega^2 - \hat\imath \omega \hat{d}(\omega)}, \tag{3.2.9}$$

$$k_{a,d}(\omega) := \sqrt{\omega^2 - \hat\imath \omega \hat{d}(\omega) - \hat{a}(\omega)}. \tag{3.2.10}$$

A better projection approximation in the case of the presence of acoustic heterogeneities can be achieved via one of the following estimations, depending on the physical considerations:

A1. In the presence of acoustic attenuation, we estimate g_0 from g_a using the relationship $g_a = \mathscr{T}_a g_0$, where $\mathscr{T}_a$ is defined by

$$\mathscr{T}_a g_0(t) = \frac{1}{2\pi} \int_{\mathbb{R}} \frac{\omega}{k_a(\omega)} e^{\hat\imath \omega t} \int_{t_1}^{t_2} g_0(t') e^{-\hat\imath k_a(\omega) t'} dt' d\omega.$$

A2. In the presence of sound dispersion, we estimate g_0 from g_d using the relationship $g_d = \mathscr{T}_d g_0$, where $\mathscr{T}_d$ is defined by

$$\mathscr{T}_d g_0(t) = \frac{1}{2\pi} \int_{\mathbb{R}} \frac{\omega}{k_d(\omega)} e^{\hat\imath \omega t} \int_{t_1}^{t_2} g_0(t') e^{-\hat\imath k_d(\omega) t'} dt' d\omega.$$

A3. In the presence of both attenuation and dispersion, we estimate g_0 from $g_{a,d}$ using the relationship $g_{a,d} = \mathscr{T}_{a,d} g_0$, where $\mathscr{T}_{a,d}$ is defined by

$$\mathscr{T}_{a,d} g_0(t) = \frac{1}{2\pi} \int_{\mathbb{R}} \frac{\omega}{k_{a,d}(\omega)} e^{\hat\imath \omega t} \int_{t_1}^{t_2} g_0(t') e^{-\hat\imath k_{a,d}(\omega) t'} dt' d\omega.$$

3.3

Specimen manufacture and experimental model conditions

Our main objective is to use photoacoustic imaging on biomedical tissues which are complex systems. It is well-known that test models (phantoms), either physical or virtual, are indispensable for the analysis of physical principles, the development of imaging tomographic technologies and image processing techniques. Unfortunately, the topic of manufacturing realistic specimens for photoacoustic purposes has been barely investigated [37]. Colleagues at the UNAM are involved in the investigation of how to manufacture good physical phantoms and we rely on them to obtain models for our experiments. The feasibility of developing reliable models depends on the availability of materials that simulate optical, electrical, mechanical, and thermal properties, in particular, energy absorption and emission, of real biological systems. However, including all important characteristics in a physical phantom simultaneously is difficult, that is why we limit the task to few specific physical properties associated with a particular problem in mind: We focus our attention on early breast cancer detection, considering the world-wide mortality rate by this disease; in 2001 it represented the second most common type of cancer in Mexico [38]. It is worth while noticing that although the scope of our problem is very specific there are still many unsolved questions.

Current breast cancer phantoms produced at the CCADET-UNAM are able to mimic optical (scattering), acoustical (sound dispersion), and mechanical (attenuation due to varying viscosity) properties of a mammary gland. The testing phantoms, like the one shown in Figure 3.3.1, are made of polyvinyl alcohol (PVA) and optional nanoparticles or other electromagnetic energy-absorbing obstacles imitating hemoglobin containing structures [37]. This material composition behaves similar to human breast tissues when photoacoustically analyzing the phantom; due to the absorption of electromagnetic radiation, acoustical disturbances are generated and propagated at sound speed. Therefore, these heterogeneous phantoms are likely to provoke attenuation and sound dispersion to be considered within the sound transport. A mathematical model that captures these perturbations is given in equation (3.1.6). Unfortunately, the PVA breast phantom described above is not appropriate for investigating the hypothesis that the sound transport approximated by plane waves suffers acoustic attenuation and dispersion since our home-made detector performance has not been validated yet.
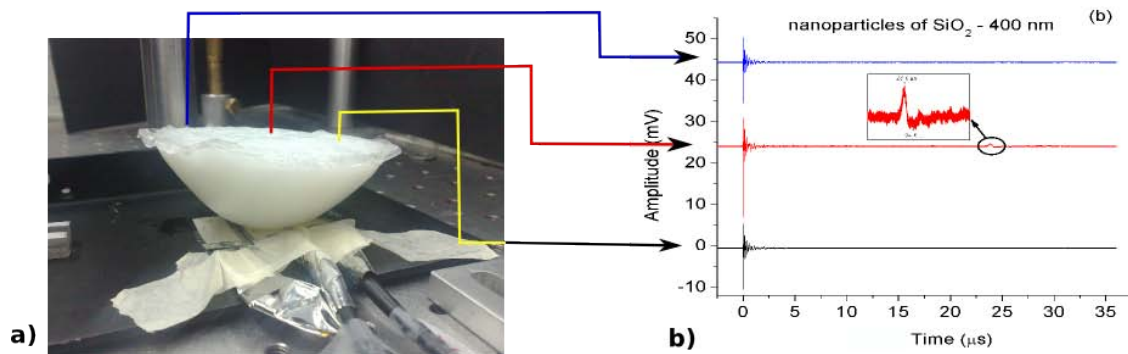
Fig. 3.3.1: Left: The polyvinyl alcohol (PVA) phantom taken from [37] with a lesion made with silicon dioxide (SiO_2) nanoparticles. Right: The photoacoustic signals at three different locations of the phantom: the top and bottom response represent lesion free tissue, the middle represents the photoacoustic signal when the dummy lesion is targeted.

To overcome this situation, we inspected two PVA rectangular 3D samples, see the scheme of the cubic samples in Figure 3.3.2, measuring 3.9 cm long (L), 4.5 cm wide, and 1.0 cm tall, and containing a 1.5 mm thick slice of neoprene (labeled N), occupying almost the complete phantom cross-section. On the phantoms' opposite side, at a distance of 2.0 cm (D), we set the photoacoustic detector (S). The detector used for our experiments of transport model validation and photoacoustic analysis is a low-noise capacitive transducer of Polyvinylidene Fluoride (PVDF) in piezoelectric mode [39]. The laser source is a pulsed Nd:YAG laser emitting pulses of $\sim$ 7 ns time-width at 1064 nm wavelength and repetition rate of 10 Hz. At the initial experimental stage, the target N is set on the surface of the phantom in such a way that the laser pulses impinge directly on it. Thus, the triggered photoacoustic signal travels $\sim$ 3.9 cm across the phantom length, plus 2.0 cm in water, before being read out by the detector S. The signal output produced by this setup is presented as a solid line in Figure 3.3.3.

Fig. 3.3.2: Schematic drawings of the two PVA-phantoms with a 1.5 mm thick slice of neoprene (N) inside. Left: N is positioned at the very extreme of the probe to gain superficial photoacoustic response. Right: N is shifted 1 cm (P) inside.

For a second experiment we place the phantom with N set at a distance (P) equal to 1.0 cm within the PVA. Thus the photoacoustic signal travels ~ 2.9 cm across the PVA and 2.0 cm in water before reaching S. This signal output is presented as a dashed line in Figure 3.3.3. For all the experiments the sensor and phantoms are kept immersed in water; see [39] and [40] for further experimental details. On the left hand side of the figure we display the photoacoustic response in the time domain while on the right hand side we display it in the frequency domain. Signal differences are apparent (for purposes of visual comparison we normalized the response amplitude): We can appreciate the time shift due to acoustic impedance and the difference in the photoacoustic signal path length. When analyzed in the frequency domain, a distribution shift and a simultaneous bandwidth ($\Delta\nu$) scaling are present. From the frequency maxima ν_{max} we estimate that the shift measures ~ 3.4 MHz, and from the estimate of $\Delta\nu_1 \sim$ 18 MHz and $\Delta\nu_2 \sim 9$ MHz, we estimate that there is a factor of 2 between the frequency bandwidths. Notice that all distances related to the incidence point and the sensor position (D + L) are kept constant during the experiments. We made sure that the neoprene's interaction area and the transducer's sensing area were parallel, while the laser excitation and, thus, the photoacoustic signal propagation were set to be perpendicular to these areas.
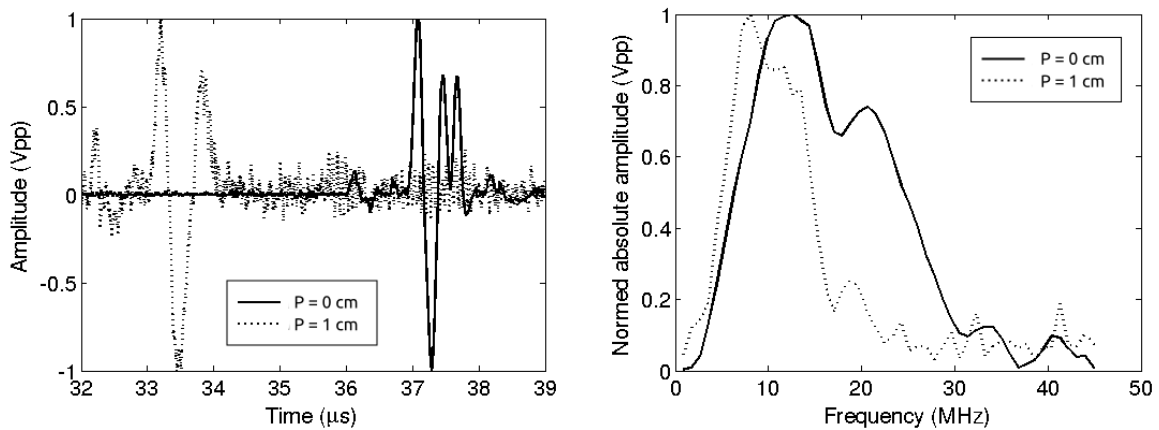
Fig. 3.3.3: Experimental photoacoustic signals in the semilogarithmic time domain (left) and frequency domain (right). We display the direct response when laser pulses impinge on a 1.5 mm thick slice of neoprene within a PVA phantom; the continuous curve results from superficial neoprene sample and the dashed curve from a 1 cm deep insertion. The bandwidth difference between both photoacoustic signals is noticeable.
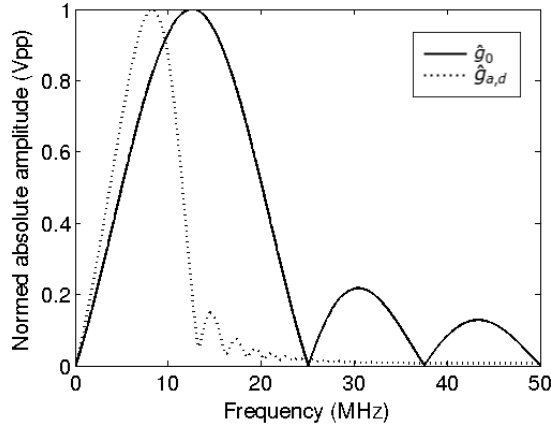
Fig. 3.3.4: Model prediction for the absence and presence of attenuation and sound dispersion. The considered cases are: the continues curve $\hat{g}_0$ expressing N on the phantom surface and the dashed curve $\hat{g}_{a,d}$ approximating N hidden within the phantom. The theoretical outcome for the photoacoustic frequency response is phenomenologically in near correspondence with the experimental observations.

Evidently, the description of the heterogeneous transport requires the knowledge of the function $k_{a,d}(\omega)$. To define this function we made the following assumptions on the acoustic propagation. For sound absorption in a homogeneous thermo-viscous medium, the wave number and frequency are related by the following equation $k(\omega) = \omega/\sqrt{1 - i\alpha\omega}$, where α is the attenuation coefficient [42, 43]. Thus, to be consistent with (3.2.10), we introduce a change of variables and define $\alpha = \bar{a} + i\omega\bar{d}$ with appropriate weighting factors $\bar{a}, \bar{d} \in \mathbb{R}$ mimicking the occurring perturbations. Then, by approximating with a series expansion of first order, we express (3.2.10) as

$$k(\omega) = \omega + \frac{1}{2}\left[\hat{\imath}\bar{a}\omega^2 - \bar{d}\omega^3\right]. \tag{3.3.1}$$

For our analysis, we assume that the superficial neoprene response approximates projection data of a rectangular function, which should result in $\hat{g}_0$ being an absolute sinc-function. Then, we discretize the transport $\mathscr{T}_{a,d}$ of (3.2) and deduce with a line search algorithm the value of -0.01 for both parameters a and b; these values best approximate the experimental photoacoustic signals. In Figure 3.3.4 we display the corresponding perturbed model response $\hat{g}_{a,d}$ which exhibits the close match between our model prediction and the physically obtained photoacoustic data in Figure 3.3.3.

This frequency analysis emphasizes the significance of attenuation and sound dispersion over the transport of a photoacoustic signal before its detection and gives support to the mathematical model extension of Section 3.1. By numerical approximations we establish a phenomenological interpretation of the experimental phenomenon and analyze sound perturbations within the detector measurements. We further develop the experimental model evaluation in the publication [44]; a copy of the article is provided in the Appendix 5.2.

Enhanced photoacoustic image reconstruction

In this chapter we present photoacoustic simulations for heterogeneous media producing sound perturbations. The objective of these experimental simulations is to facilitate the evaluation of image reconstruction results. For our experiments we use a two-dimensional image of a phantom resembling the absorption map in a cross section of a human breast. With our description of the forward problem we calculate the phantom's projections by line integrals and produce acoustic perturbations, such as transport attenuation and dispersion. Then, we approximately solve the inverse problem by applying the classical backprojection approach to the simulated data. With our system of image formation we replicate common image artifacts in the reconstruction, such as blurring and internal reflections. Importantly, when inverting the acoustic perturbations we manage to minimize these artifacts. Finally, we also propose an alternative reconstruction strategy that improves the reconstruction results by taking into account non-linear transport considerations such as detector sensibility. The advantages of the proposed algorithm are demonstrated by using realistic data of a zebra-fish provided by the Karl-Franz Universität in Graz, Austria.

4.1

Photoacoustic simulations

4.1.1 The forward problem

In order to demonstrate how the modeled sound perturbations affect the photoacoustic transport results, we carried out a simulation of the two-dimensional propagation through the phantom in Figure 4.1.1. This phantom resembles the anthropomorphic features of a cross section of a female human breast according to [45]. It is discretized to offer a simple visualization of different constant geometries (i.a, indicated by manual annotations of medical experts) and is here described as a collection of several overlapped circles and one star displayed by gray scales at distinct values from $[0,1] \cap \mathbb{Q}_+$. The data set was generated with the open source vector graphics editor INKSCAPE in such a way that it captures the geometrical properties of the characteristic biological breast components. Based on [45], we assign normalized optical absorption coefficients to the different regions in this human tissue and use values in the range $(0.5, 1]$ to specify sections of major absorption (dark gray picture elements), as it is the case of cancerous and glandular tissue. On the other hand, values in the range $[0, 0.5]$ specify sections of lesser absorption (brighter picture elements), such as fat and fibroadenoma. According to the photoacoustic effect, the light absorption map resembles the initial pressure distribution (see Section 1.1). The soft tissues that we include in the phantom appear typically in a common mammograph and similar values are expected for photoacoustic tomography due to familiar energy absorption characteristics; as an example, see the results shown in Figure 1.2.3. For testing our algorithms we used a digitized version of the phantom using a 400×400 image, which allows *enough* resolution for the details of the specimen.

The three variants of our heterogeneous transport model of Section 3.2, equations (3.2.5)-(3.2.7), require some knowledge of the function $k(\omega)$ (this is also identified as the complex wave-number). To define this function, we made the following assumptions on the acoustic propagation in accordance to both the thermo-viscous model of Nachman et al. [42] (by expanding Maclaurin series) and the mentioned differences in equations (3.2.8)-(3.2.10):
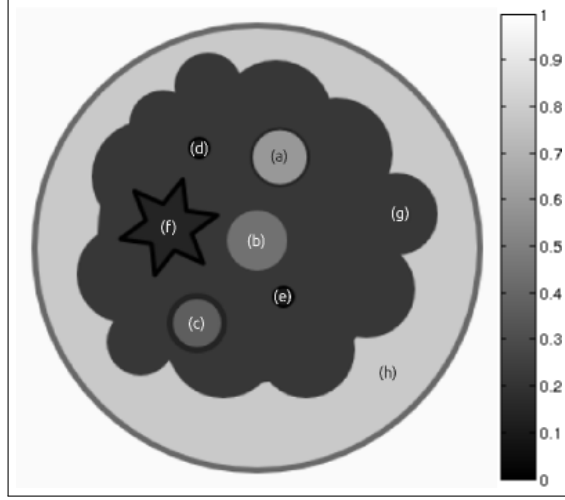
Fig. 4.1.1: A 400×400 digitization of a phantom representing structures in the coronal view of a breast by geometrical shapes. The light gray circles (a),(b), and (c) represent bounded and unbounded fibroadenomas and the dark circles (d) and (e) represent small cancerous tumors; a larger tumor is here depicted by a star (f). The expected absorption coefficients in the antropomorphic features are quantified with a value arbitrarily assigned from the interval $[0,1] \cap \mathbb{Q}_+$, while the expected absorption coefficients in the breast glandular tissue (g) are assigned to a value equal to 0.8 and in fat (h) to 0.2 (in arbitrary units).

$$k(\omega) \leftarrow \begin{cases} k_a(\omega) = \omega + \frac{1}{2}\hat{\imath}\bar{a}c\omega^2, \\[2mm] k_d(\omega) = \omega - \frac{1}{2}\bar{d}c\omega^3, \\[2mm] k_{a,d}(\omega) = \omega + \frac{1}{2}c(\hat{\imath}\bar{a}\omega^2 - \bar{d}\omega^3), \end{cases} \tag{4.1.1}$$

with appropriate weighting factors $\bar{a}$ and $\bar{d}$ mimicking perturbations in the probed soft tissues. The experimental model conditions derived in Section 3.3 suggest that the values of $\bar{a}$ and $\bar{d}$ should be equal to -0.01. Here, we simulate a photoacoustic scenario which is much larger (the diameter of the average female human breast measures 25 cm), thus, probably is characterized by greater acoustic density than the 5 cm long PVA-neoprene phantom. Accordingly, we set both perturbation weights on $\bar{a}$ and $\bar{d}$ to -0.1. Moreover, these parameters are close to the model settings of [29] and keep all calculations stable. The propagation velocity c is normalized and set to 1.

Once we decided on the corresponding attenuation and acoustic dispersion weights $\bar{a}$ and $\bar{d}$ for a specific application, and on the complex wave number $k(\omega)$ of (4.1.1), the heterogeneous forward solutions g_a, g_d, and $g_{a,d}$ can be easily derived by the homogeneous solution g_0 according to the mathematical expressions in A1-A3 of Section 3.2. For our experiments we use 180 parallel projections acquired every degree with 400 lines each. The resulting projection integrations are approximated by $g_0 \approx \mathscr{R}f$. The

heterogeneous projection data is derived by the transformation $\mathscr{T}g_0$ as outlined in the strategies A1-A3, respectively; in other words, in the case of acoustic attenuation $g_a \approx \mathscr{T}_a g_0$, in the case of sound dispersion $g_d \approx \mathscr{T}_d g_0$, and $g_{a,d} \approx \mathscr{T}_{a,d} g_0$ in the case of both perturbation factors.

4.1.2 The classical backprojection results

The results produced by the classical backprojection algorithm are obtained by applying the inverse Radon transform to the calculated projections g_0, g_a, g_d and $g_{a,d}$. After backprojecting every set of the differently perturbed data, we managed to simulate familiar artifacts, such as internal reflections [4] and image blurring [27, 28], as described in recent publications in the field, see Figure 4.1.2.

On first visual inspection, we can give the following observations: While the result in Figure 4.1.2a is an almost error-free image of the original pressure distribution map f, it poorly represents a realistic reconstruction of a breast by photoacoustic imaging in comparison to Figure 1.2.4. Backprojection of $\mathscr{L}_a$ measurements in Figure 4.1.2b brings out a blurring effect increasing towards the upper half of the image, generated in accordance to our attenuation approximation. On the other hand, backprojection of $\mathscr{L}_d$ measurements in Figure 4.1.2c produces internal reflections, directed towards one side, as determined by the transport propagation direction. As expected from the telegraph equation, Figure 4.1.2d describes a reconstruction with both phenomena, blurring and less visible reflections; hence it represents a more realistic photoacoustic transport. Besides, this last image shows that the induced blurring is dominant over the reflections.

A task oriented figure-of-merit (FOM) is suitable for a qualitative evaluation of algorithm performance. FOMs provide different measures of picture distances between a reconstruction and a phantom. Below we list two standard measures in the reconstruction literature that we use in our qualitative evaluation [15, 46]. Many other FOMs, such as the *pixel density comparision*, the *normalized mean absolute distance*, or the *pointwise accuracy*, are implemented and give in similar results. Again, for this comparison we define $\mathbf{f}$ to be the digitized phantom and $\mathbf{f'}$ to be the backprojected data of $\mathscr{R}f$; $\overline{f}$ denotes the average density of $\mathbf{f}$. Without physical evidence, this observation seems to be consistent with the real phenomenon of photoacoustic image artifacts, since blurring is significantly more mentioned in the literature.

(a) Backprojection $f_0 \approx \mathscr{R}^{-1} g_0$

(b) Backprojection $f_a \approx \mathscr{R}^{-1} g_a$

(c) Backprojection $f_d \approx \mathscr{R}^{-1} g_d$

(d) Backprojection $f_{a,d} \approx \mathscr{R}^{-1} g_{a,d}$
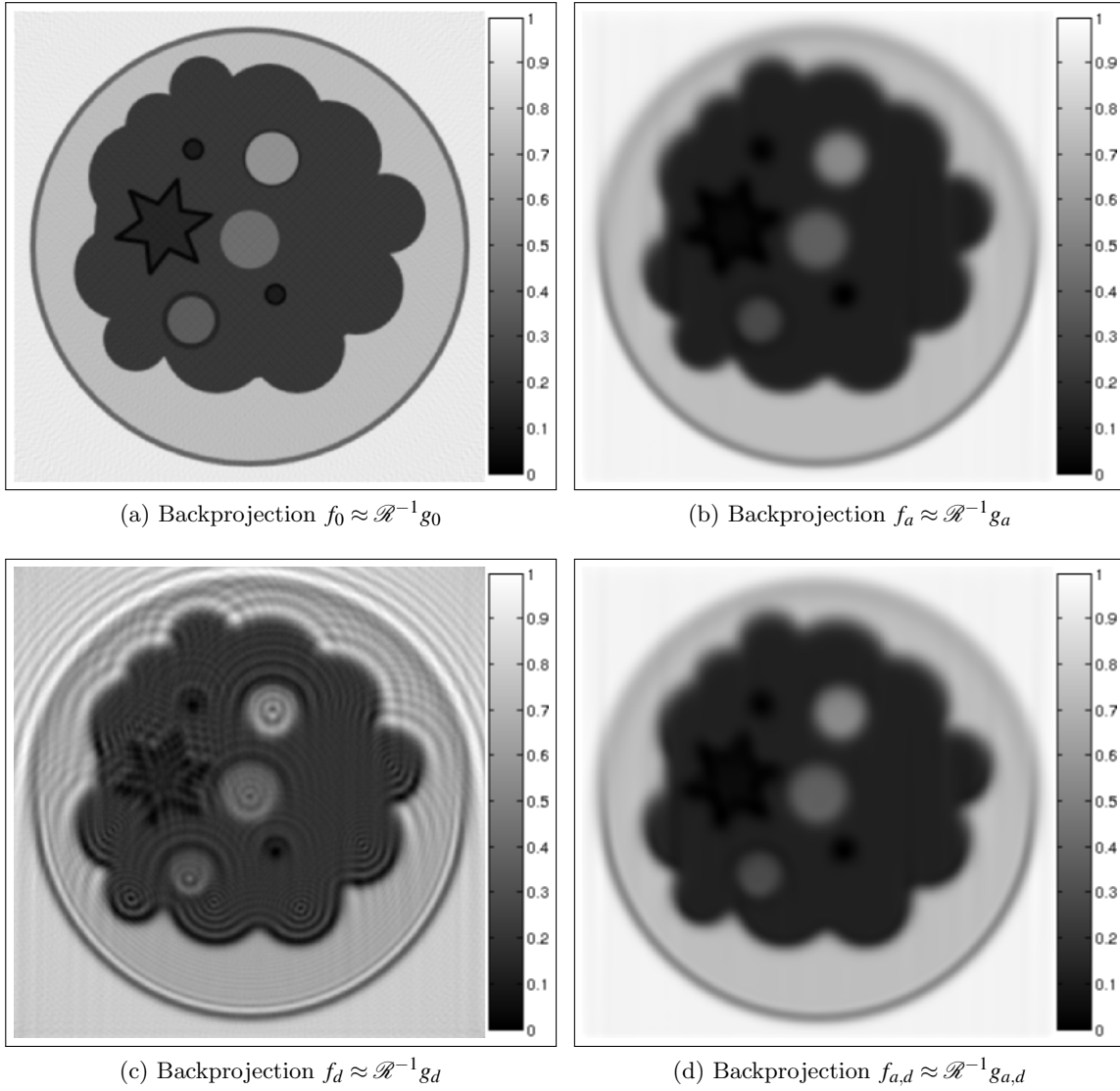
Fig. 4.1.2: Reconstructions from the projection data g_0, g_a, g_d and $g_{a,d}$. In the absence of acoustic hetero-geneities, no transport dependent artifacts are visible in (a); (b) shows image blurring, (c) shows internal reflections, and (d) shows the combination of reflections and blurring in the same reconstructed image.

1. *Normalized root mean squared distance measure* (RMS):

   This measure emphasizes the importance of large errors throughout every of the J pixels of the discretized images,

$$d_{RMS}(\mathbf{f}, \mathbf{f}') := \sqrt{\frac{\sum_{j=1}^{J}(\mathbf{f}_j - \mathbf{f}'_j)^2}{\sum_{j=1}^{J}(\mathbf{f}_j - \overline{f})^2}}. \tag{4.1.2}$$

A small value of $d_{RMS}(\mathbf{f}, \mathbf{f}')$ indicates a small reconstruction error.

2. *Structural accuracy* (STR):

   Let $\bar{f}^{(m)}, \bar{f}'^{(m)}$ be the average pixel value of $\mathbf{f}$, respectively $\mathbf{f}'$, of those pixels whose centers are within structure m from the total of M structures. Then we define the structural accuracy as

   $$d_{STR}(\mathbf{f}, \mathbf{f}') := -\frac{1}{M} \sum_{m=1}^{M} |\bar{f}'^{(m)} - \bar{f}^{(m)}|. \tag{4.1.3}$$

   In this study we compare a total number of six structures ($M = 6$) as can be distinguished in Figure 4.1.3.
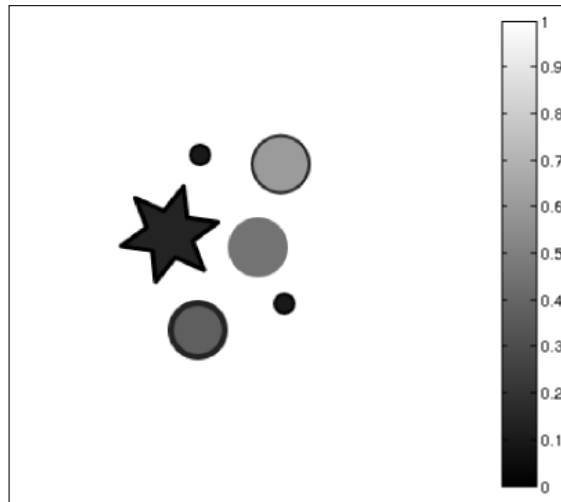
Fig. 4.1.3: Six objects of the phantom of Figure 4.1.1 for a structural accuracy evaluation.

In Table 4.1.1 we show the numerical comparison of the heterogeneous backprojection results in Figure 4.1.2 using the above mentioned FOMs. We notice that dispersion deteriorates mainly the structural accuracy and that acoustic dispersion increases the normalized root mean squared distance between the digitized phantom and its reconstruction. Interestingly, in this specific reconstruction example, the modeled acoustic perturbations are not linearly dependent. We consider that this case represents a realistic situation because attenuation and dispersion have physically distinct origins and implications.

Table 4.1.1: Mean distance and structural performance of heterogeneous noise-free backprojection.

Transport	$d_{RMS}(\mathbf{f},\mathbf{f'})$	$d_{STR}(\mathbf{f},\mathbf{f'})$
$\mathscr{L}_0$	0.1770	-0.0160
$\mathscr{L}_a$	0.2990	-0.0623
$\mathscr{L}_d$	0.4153	-0.0546
$\mathscr{L}_{a,d}$	0.2944	-0.0588

We decided not to use a filtered version of the reconstruction algorithm (e.g., *filtered backprojection*, FBP) for reasons of uncertainty what filter is suited for photoacoustic applications. Besides, we have no guarantee that some filter procedure will not delete significant information. We rely on the fact, that pure backprojection mathematically guarantees an approximate reconstruction, but actually does not produce good images [15]. The backprojection method is studied, because it indicates the nature of the more sophisticated reconstruction procedures. Of cause, in that manner blurriness is potentially more present in the reconstruction, but actually this artifact can be treated by the proposed signal processing strategy (*pre-filtering*).

4.2

Corrected photoacoustic projection data

The solution strategies elaborated in Section 3.2 give a hint about how to obtain an estimation of the transport inversion. For further simulations in a computer we need to discretize the transport $\mathscr{T}$ in propositions A1-A3 of Section 3.2 with the complex wave-number description in (4.1.1). However, its analytical inversion cannot be guaranteed since the linear system is ill-conditioned because of the heterogeneous description. An acceptable discretization $\mathbf{T}$ for the three propositions of A1-A3 can be derived by numerical analysis. One such discretization is the singular value decomposition (SVD) which approximates $\mathscr{T}$ by the matrix product $\mathbf{U}\mathbf{W}\mathbf{V}^t$ where $\mathbf{U}$ and $\mathbf{V}$ are real or complex unitary matrices (whose transpose is represented by $\mathbf{V}^t$), and $\mathbf{W}$ is a rectangular diagonal matrix. For a positive real number $\varepsilon > 0$ we can obtain an approximation of the inverse of $\mathbf{T}$ according to

$$\mathbf{T}_{1,\varepsilon}^{-1}\mathbf{g} = \sum_{j=1}^{J} \frac{w_j}{w_j^2 + \varepsilon^2} \langle \mathbf{g}, \mathbf{V}_j^t \rangle \mathbf{U}_j, \tag{4.2.1}$$

with $\mathbf{U}_j, \mathbf{V}_j^t$ representing the j-th row of matrices $\mathbf{U}, \mathbf{V}^t$, respectively, and all w_j, for all pixel indices $1 \leq j \leq J$, are nonnegative real singular values (i.e., the square roots of the J eigenvalues). As a follow-up study of the simulations in Section 4.1 we applied the inversion of the discretized transport description of propositions A1-A3 to better approximate projection data; this strategy has also been used by [29]. The SVD algorithm used for this purpose is known to become unstable when ε tends to zero. Hence, in order to derive a local optimum for the inversion, we applied a simple line search strategy which converged at $\varepsilon = 20$.

The inversion of the acoustic perturbations is realized by our procedure **PAIP** (the acronym for *photoacoustic inverse problem*) in Algorithm 4.2.1. The **PAIP** input matrix $\mathbf{G}$ is the result of the photoacoustic signal processing described by Algorithm 2.2.1. Besides, an acceptable discretization $\mathbf{T}$ with respective to one of the transport propositions A1-A3 of Section 3.2 and the precision value $\varepsilon > 0$ are given. The SVD algorithm, according to equation (4.2.1), is calculated within the procedure **svd** in line 2 of Algorithm 4.2.2. The output matrix $\mathbf{G}'$ represents corrected photoacoustic projection data.

Algorithm 4.2.1: PHOTOACOUSTIC INVERSE PROBLEM

---

1 **procedure PAIP** ($\mathbf{G}$, $\mathbf{T}$)

2 $(\mathbf{U}, \mathbf{W}, \mathbf{V}) \leftarrow \mathbf{svd}(\mathbf{T})$

3 **for** k $\leftarrow$ 1 **to** K

4      $\mathbf{g} \leftarrow \mathbf{G}_{k,\cdot}$

5      $\mathbf{g} \leftarrow \sum_{j=1}^{J} \frac{w_j}{w_j^2 + \varepsilon^2} \langle \mathbf{g}, \mathbf{V}_j^t \rangle \mathbf{U}_j$

6      $\mathbf{G}'_{k,\cdot} \leftarrow \mathbf{g}$

7 **return** $\mathbf{G}'$

Algorithm 4.2.2: PHOTOACOUSTIC COMPUTERIZED TOMOGRAPHY (Φ, $\mathbf{G}$, $\mathbf{T}$, *REC*, *PSF*)

---

1 **main**

2 $\mathbf{F} \leftarrow \mathbf{zeros}(\sqrt{J}, \sqrt{J})$

3 $\mathbf{G}' \leftarrow \mathbf{PAIP}(\mathbf{G}, \mathbf{T})$

4 $(K, I) \leftarrow \mathbf{get\_limits}(\mathbf{G}')$

5 *break* $\leftarrow$ **condition**(*strategy*)

6 **while** *break*

7   **for** k $\leftarrow$ 1 **to** K

8          $\mathbf{g} \leftarrow \mathbf{G}'_{k,\cdot}$

9   **if** *REC*$==$*BP*

10            $\mathbf{F}' \leftarrow \mathbf{Bell\text{-}BP}(\mathbf{g}, \Phi(k), \mathbf{F})$

11   **else if** *REC*$==$*BP*

12   **for** $i \leftarrow$ 1 to I

13                  $\mathbf{F}' \leftarrow \mathbf{Bell\text{-}ART}(\mathbf{g}(i), \Phi(k), \mathbf{F}, PSF)$

14   **else**

15   **return input_error**

16   *break* $\leftarrow$ **update**(*REC*)

17 **output** $\mathbf{F}'$

PAIP forms part of the computer program of two-dimensional photoacustic computerized tomography (PACT), an implementation of Algorithm 4.2.2. As it can be seen in the main body of PACT, the correction of the photoacoustic projection data occurs prior to any reconstruction strategy, either mode BP (our implemented transform method in Section 4.3) or mode ART (our series expansion method in Section 4.4). The resolution $\sqrt{J} \in \mathbb{N}$ of the reconstructed image in one dimension (i.e., the image is discretized in a total of J pixels) is a global input variable of the program, i.e., $\sqrt{J}$ is also known in the subroutines **Bell-BP** and **Bell-ART**. The $K \times I$ data matrix $\mathbf{G}$ holds the photoacoustic scans of the oscilloscope and further $\mathbf{G}'$ the projection approximations. The direction vector $\boldsymbol{\Phi}$ holds all the K acquisition angles. Predefined is the reconstruction condition (*strategy*), the point-spread function PSF (in the case of mode ART), and the transport proposition $\mathbf{T}$. The procedure **zeros**(a,b) creates an $a \times b$ matrix of zeros. The procedure **get_limits** evaluates the support of the photoacoustic transport and returns the number of the total integration directions K such as the number of projections I for each direction. The procedure **condition** determines whether the stop-criterion of the computer program is fulfilled; this criterion is modeled in consideration of a maximal iteration number and the desired image resolution, but is also influenced by procedure **update**, that adjusts the stop-criterion after each iteration adapting the reconstruction convergence conditioned by the choice of reconstruction algorithm. An error message will be returned by the procedure **input_error**, if the input data is false or incomplete.

4.3

An analytical approach

The classical backprojection method for our photoacoustic purposes is implemented in accordance to Algorithm 4.3.1. Here, one photoacoustic signal (over time or frequency) corresponds to a sequence of parallel line integrations, perpendicular to the light incidence direction. Since the procedure **Bell-BP** follows the nature of the standard *Delay-and-Sum* strategy, it approximates the inverse Radon transform $\mathscr{R}^{-1}$ and reconstructs the close match $\mathbf{f}'$ of the original image f following equation (2.1.4), given parallel beam projection data $\mathbf{g}$. Algorithm 4.3.1 assumes that the center of rotation is the center point of the projections, which is defined as (c,c), with $c = \lceil \sqrt{J}/2 \rceil$ defined as a function of the resolution $\sqrt{J}$. The input variables are the discrete projection information $\mathbf{g}$ in one acquisition angle ϕ and the zero-matrix $\mathbf{F}$ of size $\sqrt{J} \times \sqrt{J}$. As output this procedure returns the discrete approximation $\mathbf{F}$ of the original image f.

Algorithm 4.3.1: PHOTOACOUSTIC BACKPROJECTION

---

1 **procedure Bell-BP** $(\mathbf{g}, \phi, \mathbf{F})$

2 $\mathbf{x} \leftarrow [\sin(\phi), \cos(\phi)]$

3 **for** $u \leftarrow 1$ **to** $\sqrt{J}$

4   **for** $v \leftarrow 1$ **to** $\sqrt{J}$

5    $d_c \leftarrow (u-c)\cos(\theta) + (v-c)\sin(\phi)$

6   **if** $\lfloor d_c + c \rfloor \geq 1$ **and** $\lceil d_c + c \rceil \leq \sqrt{J}$

7     $\mathbf{F}(u,v) \leftarrow \mathbf{F}(u,v) + |\lfloor d_c+c \rfloor - (d_c-c)| \, \mathbf{g}(d_c+c) + |\lceil d_c+c \rceil - (d_c-c)| \, \mathbf{g}(d_c+c)$

8 **return F**

4.3.1 Improved backprojection results

In this subsection we want to demonstrate that the corrected projection data in accordance with the photoacoustic transport model leads to improved backprojection results.

Since a qualitative evaluation is restricted to a computer simulation, as performed in Section 4.1, we tried to incorporate a realistic error description into our mathematical model.
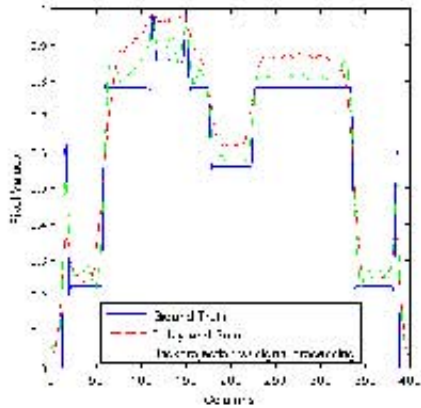
(a) Transport assumption $\mathcal{T}_a$, SNR = 14 dB
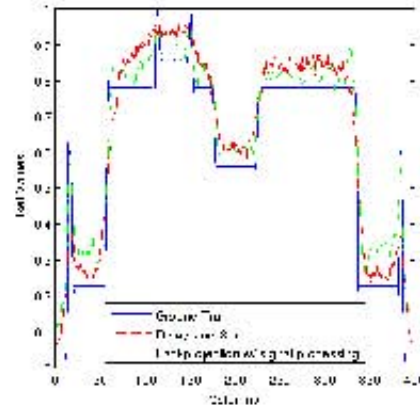
(a) Transport assumption $\mathcal{T}_a$, SNR = 8 dB
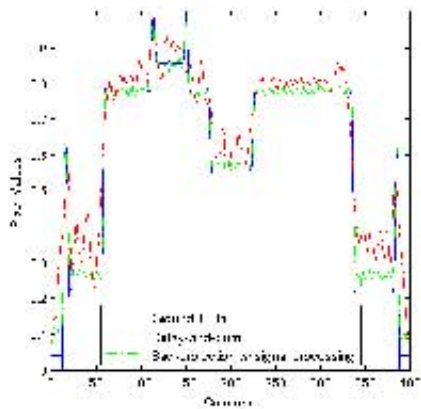
(b) Transport assumption $\mathcal{T}_d$, SNR = 14 dB
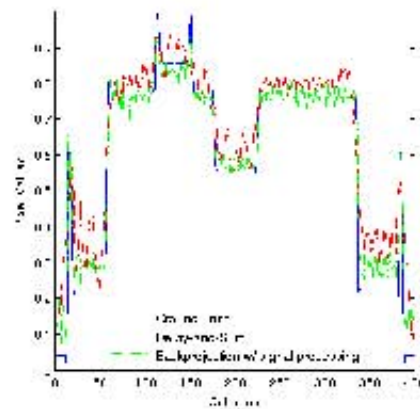
(b) Transport assumption $\mathcal{T}_d$, SNR = 8 dB
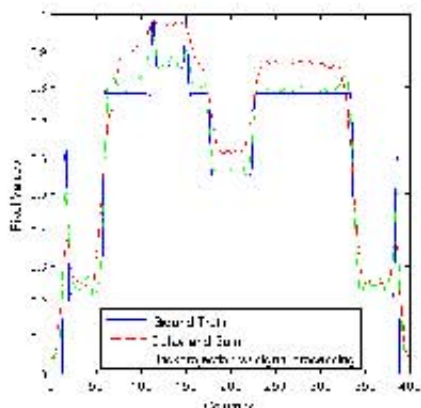
(c) Transport assumption $\mathcal{T}_{a,d}$, SNR = 14 dB
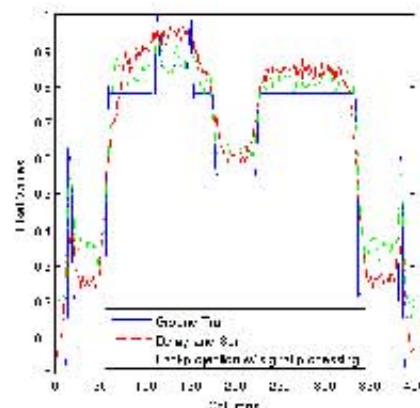
(c) Transport assumption $\mathcal{T}_{a,d}$, SNR = 8 dB

Fig. 4.3.2: The densities along the mid row in the phantom and their reconstructions with a SNR of 14 dB.

Fig. 4.3.3: The densities along the mid row in the phantom and their reconstructions with a SNR of 8 dB.

(a) Reconstruction $\mathbf{f}_a \approx \mathscr{R}^{-1}\mathbf{g}_a$

(b) Reconstruction $\mathbf{f}'_a \approx \mathscr{R}^{-1}\mathscr{T}_a^{-1}\mathbf{g}_a$

(c) Reconstruction $\mathbf{f}_d \approx \mathscr{R}^{-1}\mathbf{g}_d$

(d) Reconstruction $\mathbf{f}'_d \approx \mathscr{R}^{-1}\mathscr{T}_d^{-1}\mathbf{g}_d$

(e) Reconstruction $\mathbf{f}_{a,d} \approx \mathscr{R}^{-1}\mathbf{g}_{a,d}$

(f) Reconstruction $\mathbf{f}'_{a,d} \approx \mathscr{R}^{-1}\mathscr{T}_{a,d}^{-1}\mathbf{g}_{a,d}$
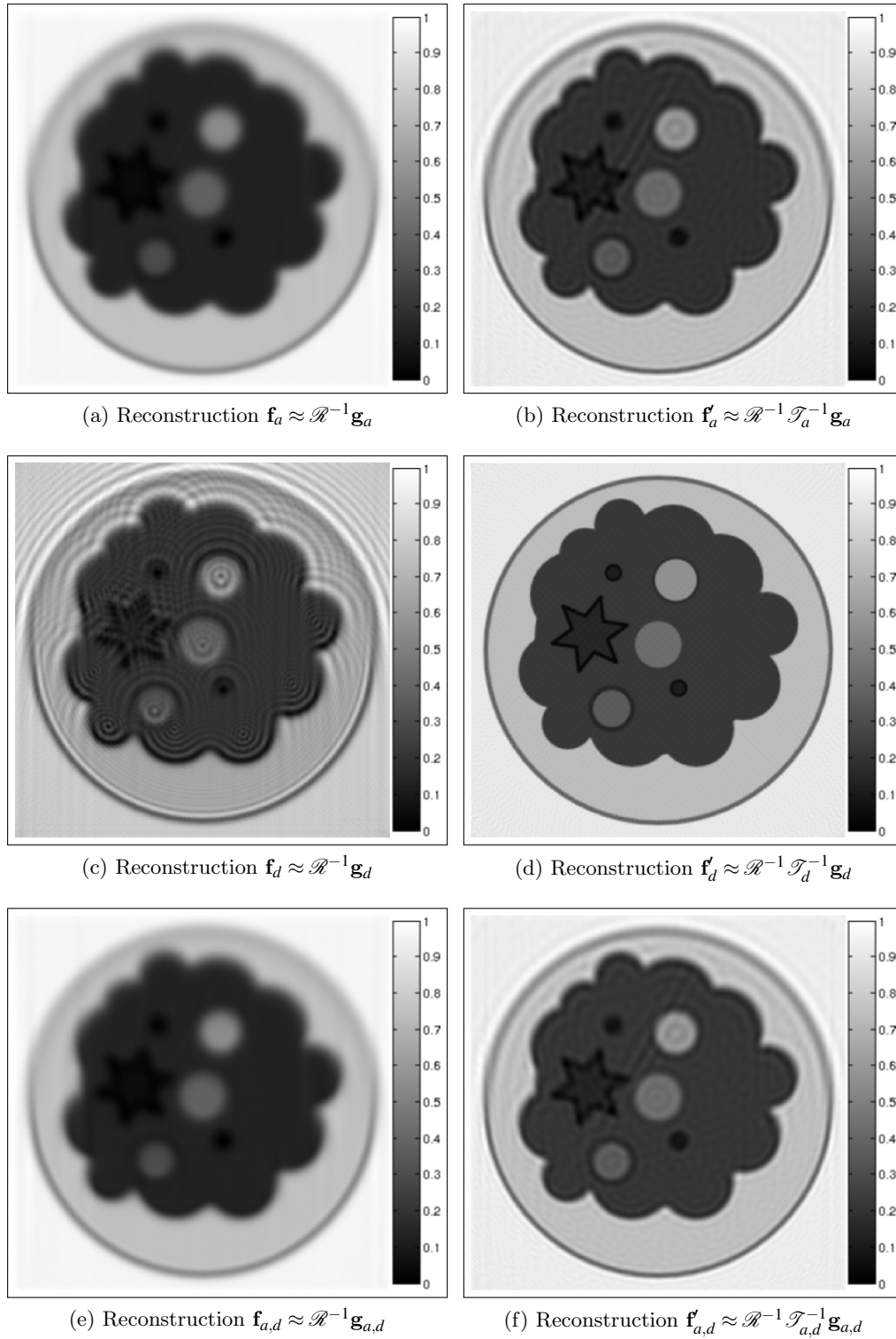
Fig. 4.3.1: Image reconstruction: (left) results of the common backprojection in the presence of additive Gaussian white noise with a SNR of 14 dB; (right) backprojection after adjustments to th projection data compensating the perturbation of acoustic heterogeneities.

The signal-to-noise analysis in [48] provides a noise description of biomedical photoacoustic measurements and indicates how to integrate this noise into our simulation. In the laboratories of the CCADET we have tested different piezoelectric sensors and measured their ambient noise; consequently, we added to our projections additive Gaussian white noise with mean $\mu = 50 \times 10^{-4}$ and standard deviation $\sigma_1 = 2 \times 10^{-4}$. The resulting signal-to-noise ratio (SNR), as defined in [47], is equivalent to $\mu/\sigma_1 = 25 \approx 14$ dB which is similar to the case study of [48]. Additionally, we considered that light scattering in deeper biological tissues impacts negatively on the photoacoustic SNR [49]. Therefore, we looked at the scenario when the SNR is reduced to 25%; thus, we selected $\sigma_2 = 8 \times 10^{-4}$, which results in $\mu/\sigma_2 = 6.25 \approx 8$ dB. This noise approximation is incorporated by $\mathbf{G}' \leftarrow \mathbf{G}' + \mathbf{noise}(\mu, \sigma)$ in the input data of Algorithm 4.2.2 after the transport calculations in line 3.

We present various backprojection reconstructions in Figure 4.3.1 obtained by inverting the simulated forward results following the three strategies A1-A3; in the left column we show the results of backprojecting the perturbed data while in the right column we show the results after appropriate adjustments that compensate for the perturbation of the modeled acoustic heterogeneities. A visual inspection of these results suggests that our methodology was able to minimize both image blurring as well as internal reflections; the latter problem seems to be particularly well resolved in this computer simulation.

For a more quantitative way of evaluating the image reconstructions we compared the plots of pixel densities for a representative column in the phantom and the reconstruction, as shown in Figures 4.3.2 and 4.3.3. In all study cases the reconstruction error, defined as the sum of all differences between the reconstruction using corrected photoacoustic projection data (green curve) and the ground truth (blue curve), has been considerably reduced, in comparison with the standard *Delay-and-Sum* algorithm (red curve). When the attenuation approximation perturbs the transport, the discrepancy between backprojection and phantom are less noticeable. The sound dispersion approximation in turn brings out a reduction of the error oscillations when applying our signal processing strategy.

In the presence of noise, we perform qualitative image reconstruction analysis taking into account the previously mentioned FOMs of Section 4.1. The results of this analysis are listed in the Table 4.3.1 (average values) where the backprojection and the perturbation adjusted reconstructions are contrasted. It is apparent that the application of transport inversion led to success in almost every transport study; the exception is the case of $\mathscr{L}_a$ with the poor SNR of 8 dB. In particular, when the heterogeneities provoke internal reflections due to acoustic dispersion the proposed projection adjustment is highly recommended.

Table 4.3.1: Mean distance and structural performance of heterogeneous noisy backprojection.

Transport	RMS		STR	
	$d_{RMS}(\mathbf{f},\mathscr{R}^{-1}\mathbf{g})$	$d_{RMS}(\mathbf{f},\mathscr{R}^{-1}\mathscr{T}^{-1}\mathbf{g})$	$d_{STR}(\mathbf{f},\mathscr{R}^{-1}\mathbf{g})$	$d_{STR}(\mathbf{f},\mathscr{R}^{-1}\mathscr{T}^{-1}\mathbf{g})$
SNR = 14 dB				
$\mathscr{L}_a$	0.2874	0.2100	-0.0544	-0.0270
$\mathscr{L}_d$	0.4220	0.1906	-0.0561	-0.0181
$\mathscr{L}_{a,d}$	0.2863	0.2021	-0.0532	-0.0235
SNR = 8 dB				
$\mathscr{L}_a$	0.2822	0.2860	-0.0475	-0.0430
$\mathscr{L}_d$	0.4174	0.2374	-0.0541	-0.0281
$\mathscr{L}_{a,d}$	0.2852	0.2807	-0.0518	-0.0380

The sound dispersion correction achieved a noticeable error minimization (especially in the center of the reconstruction) with respect to both quality measures d_{RMS} and d_{STR} when the SNR is high, while the modeled Gaussian white noise has a mean value close to zero. This correction became less noticeable as the SNR diminished. From these results we may infer that an inversion of the noisy projection information under the specific circumstances does not adversely affect the image reconstruction. On the contrary, the projection processing strategy provides a fundamental improvement on image reconstructions in the presence of acoustic perturbations. We identified the model inconsistencies and corrected the projection data at the stage prior to reconstruction. Hence, advanced algorithms using more detailed photoacoustic paradigms, such as [4], might improve the quality of reconstructions even more.

4.4

An algebraic reconstruction technique

Backprojection algorithms have been, so far, widely used for image reconstruction in photoacoustic tomography. These algorithms are based on closed-form inversion formulas expressed in two or three dimensions and are analogues to the inverse Radon transform [21]. The underlying mathematical concept only permits to approximate non-linear transport aspects to a certain degree. An alternative and even more flexible solution approach may be found in the class of iterative procedures outlined in Section 2.1. For instance, a series expansion technique allows incorporating heterogeneous transport descriptions during the iterative reconstruction process. The aim of this section is to investigate whether the use of the algebraic reconstruction techniques (ART) for photoacoustic transport may provide results comparable to, or even better than, those obtained by backprojection algorithms.

Similar to the work on model-based algorithms [50, 51], we consider the case of a suitable transfer function to specify the sensitivity of a general acoustic detector and incorporate it in the definition of the basis functions of the ART algorithm. A polar graph can describe how well a detector senses information from different directions, such as the supercardiodal Sennheiser MKH-416 displayed in Figure 4.4.1 where the colored curves indicate regions of equal frequencies [52].
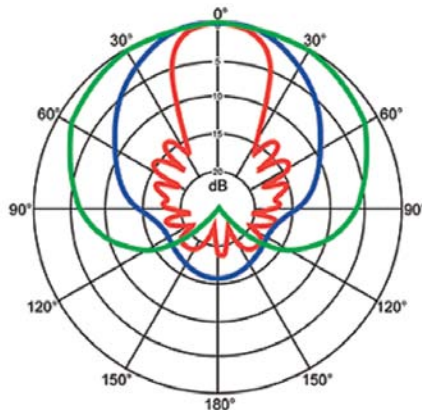
Fig. 4.4.1: The acoustic response of the microphone Sennheiser MKH-416: The polar response pattern for high frequencies (above 8 kHz) is shown in red. The mid-frequency (1-8 kHz) polar pattern of the same microphone is shown in blue. The typical cardioid response is shown in green.

For the following discussion we assume that a photoacoustic detector operates like the microphone whose polar graph is shown in Figure 4.4.2. This hypothesis is based on several observations and measurements of photoacoustic detectors manufactured by Dr. Bartolomé Reyes Ramirez [39, 40, 41] at the CCADET-UNAM. The detector of our interest tends to be unidirectional, so that a satisfactory microphone model describes a good sensitivity in the direction of 0 degrees. Its sensitivity decays monotonically towards its sides: the faster its decay the greater the distance to the microphone. Based on experimental observations, we intend to use basis functions for the ART algorithm of photoacoustcs that behave like the polar graph in Figure 4.4.2 by defining them as

$$
b_j(r,\phi) = \begin{cases}
1 & \text{if the } j\text{th pixel is inside the } \phi\text{-stripe of 100 \% reception} \\
0.8 & \text{if the } j\text{th pixel is inside a } \phi\text{-stripe of 80 \% reception} \\
0.6 & \text{if the } j\text{th pixel is inside a } \phi\text{-stripe of 60 \% reception} \\
0.4 & \text{if the } j\text{th pixel is inside a } \phi\text{-stripe of 40 \% reception} \\
0.2 & \text{if the } j\text{th pixel is inside a } \phi\text{-stripe of 20 \% reception} \\
0 & \text{otherwise.}
\end{cases}
\tag{4.4.1}
$$

The orientation of the stripes varies with the angle ϕ of the detector alignment. Since the sensitivity transfer function is fixed on Ω, conditioned by the position of the detector, b_j is invariant to r.
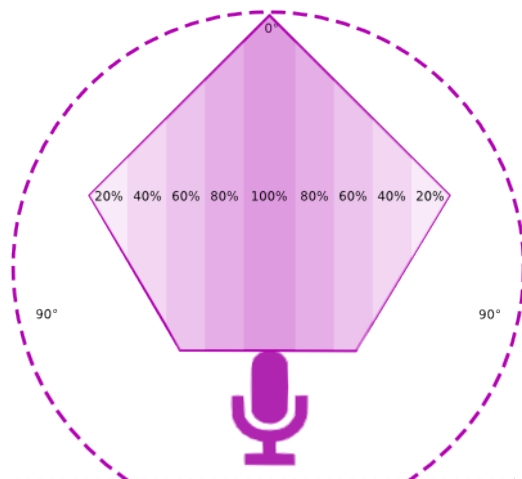
Fig. 4.4.2: Hypothetical response of a photoacoustic detector as used in [41]. Every colored stripe indicates a region of equal sensitivity. The centered strip corresponds to 100 % efficiency; each graduation towards the side corresponds to a potential loss of 20 %.

The ART algorithm presented in Section 2.1 has been extended for our photoacoustic purposes as indicated by the procedure **Bell-ART** in the pseudocode of Algorithm 4.4.1. Globally known are the matrix $\mathbf{P}$ that indicates the polygon approximating the polar graph of the sensor as in Figure 4.4.2 and the basis function b_j of equation (4.4.1). The input variables are the projection vector $\mathbf{g}$ at the integration position i, the acquisition angle ϕ, a discrete approximation $\mathbf{F}$ of the original image f (initialized with the zero-matrix of size $\sqrt{J} \times \sqrt{J}$) and the point spread function (PSF). The transfer function of the detector sensibility is represented by the boolean function PSF: the total of three modes $PSF(1)$, $PSF(2)$ and $PSF(3)$ manipulate the photoacoustic transport projections modeled by $\mathbf{R}$ and interfere with the operation $\mathbf{Rf} \approx \mathbf{g}$, where $\mathbf{f}$ represents the image vector to be reconstructed and $\mathbf{g}$ the detected photoacoustic response. **Bell-ART** inverts the discretized operation to approximate the image $\mathbf{f} \approx \mathbf{R}^{-1}\mathbf{g}$ that is represented by the output matrix $\mathbf{F}'$. Further, the Algorithm 4.4.1 makes use of the following procedures: **ones**(a,b) creates a $a \times b$ matrix of ones; **deblur(R)** returns the Gaussian filtered data matrix $\mathbf{R}$; **imrotate(R,ϕ)** rotates the matrix $\mathbf{R}$ by the angle ϕ around its center in a counterclockwise direction; **reshape(A,a,b)** gives a matrix of size $a \times b$ whose elements are taken columnwise from the array $\mathbf{A}$.

Algorithm 4.4.1: PHOTOACOUSTIC ART

---

1 **procedure Bell-ART** $(\mathbf{g}(i), \phi, \mathbf{F}, PSF)$

2 $\mathbf{R} \leftarrow \mathbf{zeros}(\sqrt{J}, \sqrt{J})$

3 **if** $PSF(1) == \text{true}$

4    $\mathbf{R}_{i,\cdot} \leftarrow \mathbf{ones}(1, \sqrt{J})$

5 **else if** $PSF(2) == \text{true}$

6    $(a,b) \leftarrow \mathbf{R}_{i,\cdot} \cap \mathbf{P}$

7    $d_l \leftarrow \|b - a\|$

8    $\mathbf{R}_{i,a:b} \leftarrow \mathbf{ones}(1, d_l)$

9   **for** $j \leftarrow a$ **to** b

10      $\mathbf{R}_{i,j} \leftarrow b_j(1, \phi)$

11 **if** $PSF(3) == \text{true}$

12    $\mathbf{R} \leftarrow \mathbf{deblur}(\mathbf{R})$

13 **else**

14   **return input_error**

15 $\mathbf{R} \leftarrow \mathbf{imrotate}(\mathbf{R}, \phi)$

16 $\mathbf{R} \leftarrow \mathbf{reshape}(\mathbf{R}, 1, \sqrt{J} \cdot \sqrt{J})$

17 $\mathbf{f} \leftarrow \mathbf{reshape}(\mathbf{F}, J, 1)$

18 $\mathbf{f} \leftarrow \mathbf{f} + \frac{\mathbf{g}(i) - \mathbf{R} \cdot \mathbf{f}}{\langle \mathbf{R}, \mathbf{R} \rangle} \mathbf{R}^T$

19 $\mathbf{F}' \leftarrow \mathbf{reshape}(\mathbf{f}, \sqrt{J}, \sqrt{J})$

20 **return** $\mathbf{F}'$

All PSF modes can be understood as independent ways of acoustic expansions: $PSF(1)$ refers to a homogeneous propagation through equi-longitudinal lines and implements the basis function b_j of (2.1.7), $PSF(2)$ implements b_j of (4.4.1), and represents a weighted propagation from one in the center towards zero at both ends following a linear decay, and $PSF(3)$ assigns distortion to the projection lines using a Gaussian kernel. The acoustic expansion of types $PSF(2)$ and $PSF(3)$ are of non-linear nature.

4.4.1 Iterative non-linear model-based results

In order to empirically evaluate the performance of the Bell-ART algorithm we considered once again the experimental measurements provided by the group of scientists at the Karl-Franz Universität in Graz [23] (see Section 2.2.2). The reference image by Gratt et al. as illustrated in Figure 4.4.3 (right) is the result of the filtered backprojection algorithm $\mathbf{iradon}(\mathbf{R}, \theta)$ (inverse Radon transform) included in MATLAB, an implementation of the function (2.1.4); its filter is designed directly in the frequency domain and then multiplied by the Fourier transform of the projections. The routine **iradon** reconstructs the image from projection data in the two-dimensional array $\mathbf{R}$; θ describes the angles (in degrees) at which the projections were taken. Further, to prevent any bias from additional image processing contributions on reconstruction, we compare the **Bell-ART** output to the similar result of the backprojection implementation **iradon** of MATLAB in Figure 4.4.3a; the output of **Bell-BP** in Figure 4.4.3b presents a clearly different histogram distribution compared to the ART reproductions. For all applications in this section we use an image resolution of 100×100 pixels because of the higher computational requirements of the **Bell-ART** algorithm as compared to those of backprojection. This resolution suffices our requirements for this preliminary study.

(a) MATLAB **iradon**　　　　　　　　　(b) **Bell-BP** ≡ **iradon** without filtration
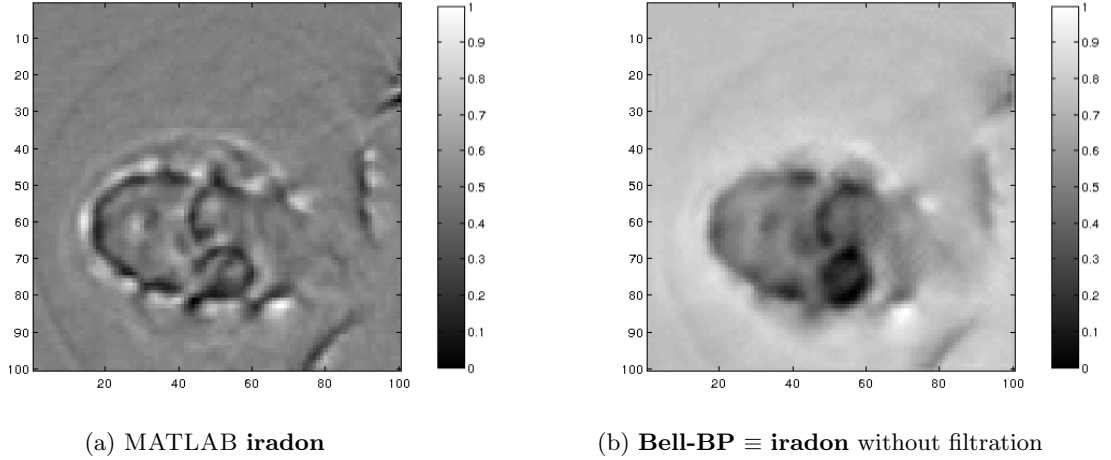
Fig. 4.4.3: Backprojection reconstructions: (a) result of the **iradon** algorithm by MATLAB, that is further processed with an Ram-Lak filter; (b) result of the **Bell-BP** algorithm.

The results of iterative non-linear model-based photoacoustic reconstruction are demonstrated in Figure 4.4.4 where we show the outcome of the **Bell-ART** algorithm taking into account the sensitivity of a hypothetical detector. Figure 4.4.5 shows the outcome when this method is extended by an acoustic distortion applying a Gaussian low-pass filter. By visually comparing the image reconstructions using the **Bell-ART** method it is possible to detect small differences in the different outputs of the different versions of **Bell-ART**. On the one hand, it seems that by incorporating a model of an acoustic detector it is possible to decrease the artifacts produced by reflections on the fish's outer borders. On the other hand, we observe that the distortion operator suppresses the background noise without losing image resolution inside the fish. Notwithstanding, the above observations are subjective. To account for an objective criterion, without knowledge of the effective photoacoustic absorption map, we use the measure d_S of entropy, inspired by [53] on the obtained reconstructions. Hence, we define

$$d_S(\mathbf{f'}) := -\sum_{s=1}^{\Gamma} h^{\mathbf{f'}}(s) \times \log_2(h^{\mathbf{f'}}(s)), \tag{4.4.2}$$

where $h^{\mathbf{f'}} : [1, \Gamma] \to [0, J]$ is a histogram function (over $\mathbb{N}$) that represents the histogram of the image $\mathbf{f'}$ with J bins; the change of the definition set of values form $[0,1] \in \mathbb{Q}_+$ to $[1, \Gamma] \in \mathbb{N}$ is required by the definition of d_S. In our representation in Figure 4.4.3 - Figure 4.4.5 the total number of bins Γ equals 255.

(a) **Bell-ART** *PSF*(1)   (b) **Bell-ART** *PSF*(2)
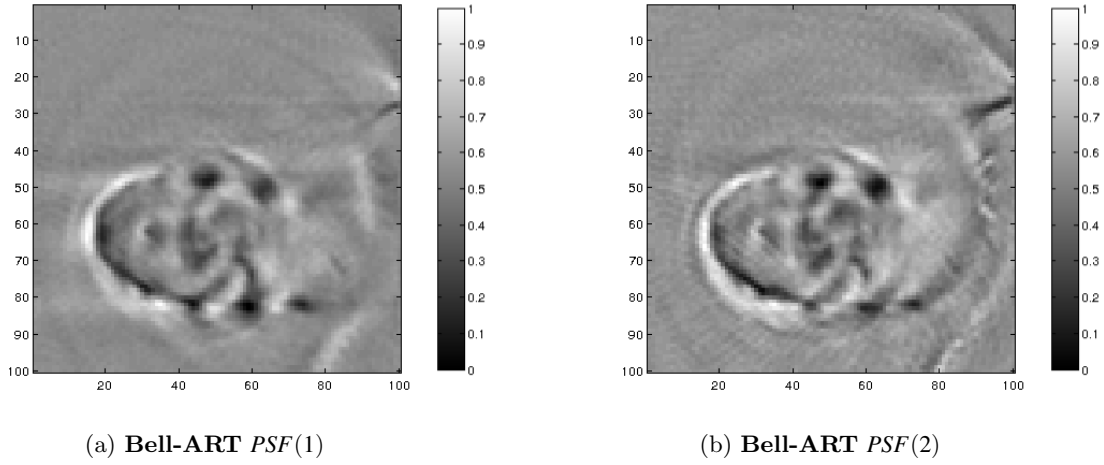
Fig. 4.4.4: Results of the **Bell-ART** algorithm: (a) linear photoacoustic transport considerations (mode PSF(1)); (b) non-linear transport considerations taking into account the sensitivity of the detector (mode PSF(2)).

(a) **Bell-ART** PSF(1) with PSF(3)   (b) **Bell-ART** PSF(2) with PSF(3)
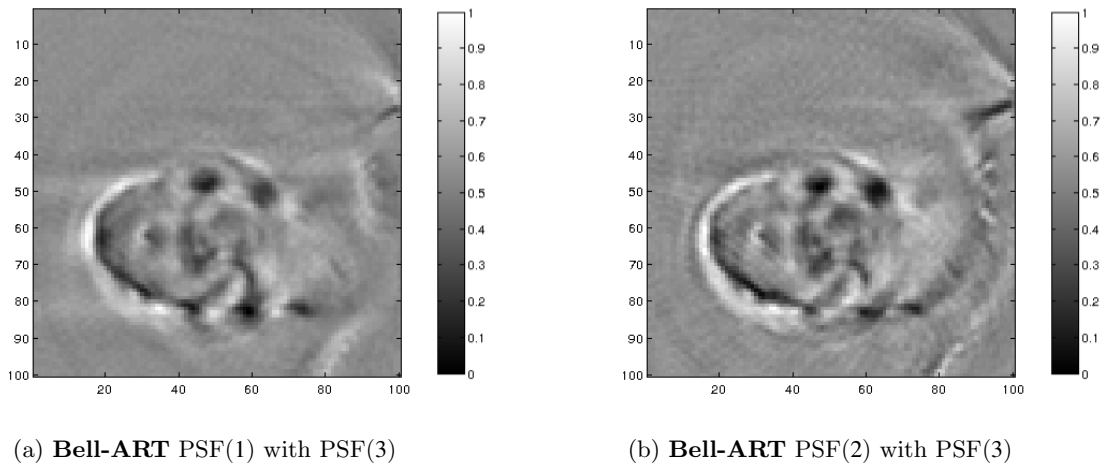
Fig. 4.4.5: Results of the **Bell-ART** algorithm under non-linear transport considerations: (a) the effect of acoustic distortion (mode PSF(3)); (b) the effect of detector sensitivity influences and acoustic distortion (mode PSF(2) + PSF(3)).

Table 4.4.1: Measure of entropy on the obtained reconstructions.

iradon	2.9883
Bell-ART PSF(1)	3.0706
Bell-ART PSF(2)	3.1766
Bell-ART PSF(1) with PSF(3)	3.0716
Bell-ART PSF(2) with PSF(3)	3.1832

According to [53], high entropy using the definition (4.4.2) implies more reasonable images and better fits to the original distribution map. This fact allows to interpret the results in Table 4.4.1 analytically. We conclude that the apparently outstanding performance of **Bell-ART** in mode PSF(2) with PSF(3) over backprojection methods looks promising to enhance photoacoustic imaging. In this comparison we leave out the result of the **Bell-BP** algorithm since it produces a completely different value distribution as illustrated in Figure 4.4.3b.

Chapter 5

Conclusions

5.1

Discussion of the obtained results

New photoacoustic waveform models have been studied and implemented at the UNAM along this doctoral thesis. We focused on the complex scenario of acoustically heterogeneous media producing sound perturbations which is of great importance for biomedical applications. After a review of the literature, it was considered that transport adjustments, especially for sound perturbations, have to be included when reconstructing photoacoustic images from projection data.

As exhibited by the frequency analysis of the shown experiments, attenuation and sound dispersion affect significantly the acoustic transport. Our studies have demonstrated that the photoacoustic transport in heterogeneous media can be modeled by the Heaviside telegraph equation (3.1.6). This propagation model is capable of simulating internal reflections and image blurring commonly present in images produced from photoacoustic data. On observing the model output we deduce, that in general, projection data identified as the Radon transform of the source lead to bad approximation of the absorption distribution. Moreover, we illustrated, by a computational simulation, how this misinterpretation affects the reconstruction details. An approximate inversion of the considered sound perturbation is implemented as a preprocessing of the acquired data. This compensation led to a significant improvement in all study cases, using a quality and performance evaluation of the backprojection algorithm. It is unlikely that this improvement occurs by chance alone.

The findings presented here show the applicability of common algorithms for reconstruction from projections in photoacoustic imaging by making sure that the acquired data complies with an appropriate perturbed transport model. As well as in [29], our work encourages the usage of recent improvements on reconstruction algorithms to produce superior results. Besides our achievement on linear transport adjustments, we also introduced some novel non-linear considerations along with our preliminary research on photoacoustic ART. We noticed that especially the polar graph of the sensors sensitivity plays an important role in computerized tomography which is worth taking into account while reconstruction.

Consistent with most photoacoustic transport considerations, our model extension unifies actual theoretical and experimental findings of photoacoustics and provides support for a better tomographic image analysis and diagnosis on the field. We developed a classification of the waveform transport, inspired on photoacoustic methods, that potentially will benefit biological, geological and medical waveform imaging, such as acoustical, seismic or optical tomography.

Finally, we consider that our proposed methodology can be extended to other modalities of waveform tomography by simply estimating the model parameters for the specific inverse problem. Once the appropriate values are selected, it is important to adjust the acquired photoacoustic data to the perturbed transport model. It is important to notice that to advance the research in photoacoustic tomography it is necessary to carry further work to characterize the noise present in the data acquired by different kinds of detectors.

5.2

Future work

During the study of photoacoustic image reconstruction of heterogeneous media different physical-mathematical considerations and computational implementations were acquired. In the following, I summarize my personal point of view towards its state of the art and its worthwhile future work:

Concept: In this thesis, I present the mathematical concept of photoacoustic tomography as a generalization of principles from acoustical, seismic, and optical tomography. This approach represents a valid extension for all waveform modalities. It tends to reduce image artifacts such as wave reflections and blurring and possibly facilitates photoacoustic image registration and fusion applications.

Model constraints: Linear model constrains are necessary for the projection approach of the image reconstruction algorithms. I explored all classes of linear differential equations of second order that can be represented by the Heaviside telegraph equation (3.1.6). The model coefficients imply a great variety of experimental interpretations, that is left to discover. Onward performing a broad phantom study, medical applications become viable. Ongoing research addresses further realistic phantoms of biological tissues of different dimensions. Laboratory sessions with small animals, such as fishes, mice or scorpions, are also considered at the CCADET-UNAM together with our international collaborators. Algorithmic benefits are expected with the combination of the linear sound dispersion transport adjustments and algebraic reconstruction techniques with non-linear adjustments.

Furthermore, the perturbed wave transport can be represented by higher order systems of equations, as long as they fit the inverse problem with a *manageable* and linearizable set of solutions. It surely arises my interests to search for even better perturbed wave equations for the purpose of photoacoustic reconstructions of heterogeneous media.

Error studies: Error studies are essential for validating realistic models; this refers to noise approximations in Section 4.3.1 and the error on transforming photoacoustic measurements into a positive signal in Section 2.2.1. They influence in large part the image resolution and contrast. The considerations in the present thesis follow some observations of other authors from this field of research. But actually, no explicit photoacoustic error studies are provided in the literature. Among others, I am looking forward to work on this topic in the future.

References

1. Balasundaram, G., Ho, C.J.H., Li, K., Driessen, W.H., Dinish, U.S., Wong, C.L., Ntziachristos, V., Liu, B., Olivo, M.: Molecular photoacoustic imaging of breast cancer using an actively targeted conjugated polymer. Int. J. Nanomed. **10**, pp. 387–397 (2015)

2. Nass, S.J., Henderson, I.C., Lashof, J.C.: Mammography and Beyond Developing Technologies for the Early Detection of Breast Cancer. National Academies Press, Washington, D.C. (2001)

3. Xu, M., Wang, L.V.: Photoacoustic imaging in biomedicine. Rev. Sci. Instrum. **77**, pp. 041101-1–22 (2006)

4. Dean-Ben, X.L., Ma, R., Razansky, D., Ntziachristos, V.: Statistical Approach for Optoacoustic Image Reconstruction in the Presence of Strong Acoustic Heterogeneities. IEEE T. Med. Imaging **30**, pp. 401–408 (2011)

5. Xu, M., Wang, L.V.: Universal back-projection algorithm for photoacoustic tomography. Phys. Rev. E **71**, pp. 016706-1–7 (2005)

6. Gilkes, D.M., Xiang, L., Lee, S.J., Chaturvedi, P., Hubbi, M.E., Wirtz, D., Semenza, G.L.: Hypoxia-inducible factors mediate coordinated RhoA-ROCK1 expression and signaling in breast cancer cells. P. Natl. Acad. Sci. USA **111**, pp. E384–E393 (2013)

7. Bell, A.G.: On the production and reproduction of sound by light: the photophone. Am. J. Sci. **3**, pp. 305–324 (1880)

8. Thompson, S.P.: Notes on the construction of the photophone. Phys. Soc. Proc. **4**, pp. 184–190 (1881)

9. Cox, B., Beard, P.C.: Modeling photoacoustic propagation in tissue using k-space techniques. In: Wang, L.V.: Photoacoustic Imaging and Spectroscopy, pp. 25–34. CRC Press, Taylor & Francis Group, Boca Raton, USA (2009)

10. Diebold, G.J.: Photoacoustic monopole radiation: waves from objects with symmetry in one, two, and three dimensions. In: Wang, L.V.: Photoacoustic Imaging and Spectroscopy, pp. 25–34. CRC Press, Taylor & Francis Group, Boca Raton, USA (2009)

11. Zhang, H.F., Maslov, K., Stoica, G., Wang, L.V.: Functional photoacoustic microscopy for high-resolution and noninvasive in vivo imaging. Nat. Biotechnol. 24, pp. 884–851 (2006)

12. Provost, J., Lesage, F.: The application of compressed sensing for photo-acoustic tomography. IEEE T. Med. Imaging **28**, pp. 585 – 594 (2009)

13. Ma, R., Distel, M., Deán-Ben, X.L., Ntziachristos V., Razansky, D.: Non-invasive whole-body imaging of adult zebrafish with optoacoustic tomography. Phys. Med. Biol. **57**, pp. 7227–7237 (2012)

14. Heijblom, M., Piras, D., Xia, W., van Hespen, J.C.G., Klaase, J.M., van den Engh, F.M., van Leeuwen, T.G., Steenbergen, W., Manohar, S.: Visualizing breast cancer using the Twente photoacoustic mammoscope: What do we learn from twelve new patient measurements?. Opt. Express **20**, pp. 11582–11597 (2012)

15. Herman, G.T.: Fundamentals of Computerized Tomography: Image Reconstruction from Projections. Springer Publishing Company, Incorporated (2009)

16. Kruger, R.A., Reinecke, D.R., Kruger, G.A.: Thermoacoustic computed tomography. Med. Phys. **26**, pp. 1832–1837 (1999)

17. Herman, G.T., Davidi, R.: Image reconstruction from a small number of projections. Inverse Probl. **24**, pp. 1–17 (2008)

18. Finch, D., Patch, S.K., Rakesh: Determining a function from its mean values over a family of spheres. SIAM J. Math. Anal. **35**, pp. 1213–1240 (2004)

19. Natterer, F., Wübbeling, F.: Mathematical Methods in Image Reconstruction. SIAM Monographs on Mathematical Modeling and Computation (2001)

20. Felsberg, M.: A novel two-step method for CT reconstruction. In: Tolxdorff, T., Braun, J., Deserno, ,T.M., Handels, H., Horsch, A., Meinzer H.P.: Bildverarbeitung für die Medizin, pp. 303–307. Informatik aktuell, Springer, Berlin, Germany (2008)

21. Ntziachristos, V., Razansky, D.: Molecular imaging by means of multispectral optoacoustic tomography. Chem. Rev. **110**, pp. 2783–2794 (2010)

22. Moock, V.M., García-Segundo, C., Garduño, E., Arámbula-Cosio, F., Jithin, J., van Es, P., Manohar, S., Steenbergen, W.: Signal processing for photoacoustic tomography. In: 5th International Congress on Image and Signal Processing (CISP), pp. 957–961. Chongqing, China (2012)

23. Gratt, S., Passler, K., Nuster, R., Paltauf, G.: Photoacoustic section imaging with an integrating cylindrical detector. Biomed. Opt. Express **2**, pp. 2973–2981 (2011)

24. Censor, Y.: Finite Series-Expansion Reconstruction Methods. P. IEEE **71**, pp. 409–419 (1983)

25. La Rivière, P.J., Zhang, J., Anastasio, M.A.: Image reconstruction in optoacoustic tomography for dispersive acoustic media. Opt. Lett. **31**, pp. 781–783 (2006)

26. Maslov, K., Wang, L.V.: Photoacoustic imaging of biological tissue with intensity-modulated continuous-wave laser. J. Biomed. Opt. **13**, pp. 0240061–0240065 (2008)

27. Grün, H., Nuster, R., Paltauf, G., Haltmeier, M., Burgholzer, P.: Photoacoustic tomography of heterogeneous media using a model-based time reversal method. P. SPIE **6856**, pp. 685620-1–9 (2008)

28. Jithin, J., Willemink, R.G.H., Steenbergen, W., Slump, C.H., van Leeuwen, T.G., Manohar, S.: Speed-of-sound compensated photoacoustic tomography for accurate imaging. Med. Phys. **39**, pp. 7262–7271 (2012)

29. Ammari, H.: Photoacoustic imaging for attenuating acoustic media. In: Ammari, H.: Mathematical Modeling in Biomedical Imaging II – Optical, Ultrasound, and Opto-Acoustic Tomographies, pp. 57–84. Springer, Berlin Heidelberg, Germany (2012)

30. Xu, C., Kumavor, P.D., Aguirre, A., Zhu, Q.: Investigation of a diffuse optical measurements-assisted quantitative photoacoustic tomographic method in reflection geometry. J. Biomed. Opt. **17**, pp. 061213-1–11 (2012)

31. Zha, Z., Deng, Z., Li, Y., Li, C., Wang, J., Wang, S., Quc, E., Dai, Z.: Biocompatible polypyrrole nanoparticles as a novel organic photoacoustic contrast agent for deep tissue imaging. Nanoscale **5**, pp. 4462–4467 (2013)

32. Greenleaf, J.F.: Computerized tomography with ultrasound. P. IEEE **71**, pp. 330–337 (1983)

33. Kowar, R., Scherzer, O.: Attenuation models in photoacoustics. In: Ammari, H.: Mathematical Modeling in Biomedical Imaging II – Optical, Ultrasound, and Opto-Acoustic Tomographies, pp. 85–130. Springer, Berlin Heidelberg, Germany (2012)

34. Barnard, V.: The inversion of the Boltzmann transport equation with medical optical tomography applications. Imperial College London. `http://amcg.ese.ic.ac.uk/~jgomes/AMCG_thesis/Barnard_Thesis.pdf` (2006). Accessed 18 July 2013.

35. Joseph, D.D., Preziosi, L.: Heat waves. Rev. Mod. Phys. **61**, pp. 41–73 (1988)

36. Arridge, S.R.: Optical tomography in medical imaging. Inverse Probl. **15**, pp. R41–R93 (1999)

37. Quispe-Siccha, R.M., Reyes-Ramírez, B., García-Segundo, C., Hevia-Montiel, N., Arámbula Cosío, F., Sato-Berrú, R., Flores-Flores, J.O.: Implementation of polyvynil-alcohol mixed with nano-particles as a near representation of biological tissue: ultrasonic and photothermal study. J. App. Res. Technol. **10**, pp. 63–72 (2012).

38. Nass, S.J., Henderson, I.C., Lashof, J.C.: Mammography and Beyond: Developing Technologies for the Early Detection of Breast Cancer. National Cancer Policy Board, Institute of Medicine, Division of Earth and Life Studies, National Research Council (2001)

39. Reyes-Ramírez, B., García-Segundo, C., García-Valenzuela, A.: An examination of polyvinylidene fluoride capacitive sensors as ultrasound transducer for imaging applications. Meas. Sci. Technol. **25**, pp. 055109-1–10 (2014)

40. Reyes-Ramírez, B., García-Segundo, C., García-Valenzuela, A.: On the spectral response of thick piezoelectric capacitive sensors for arrays in imagenology applications. Proc. SPIE **9040**, pp. 90401J-1–8 (2014)

41. Reyes-Ramírez, B., García-Segundo, C., García-Valenzuela, A.: Spectral response analysis of PVDF capacitive sensors. J. Phys: Conf. Series **450**, pp. 012032-1–6 (2013)

42. Nachman, A.I., Smith, J.F., Waag, R.C.: An equation for acoustic propagation in inhomogeneous media with relaxation losses. J. Acoust. Soc. Am. **88**, pp. 1584–1595 (1990)

43. Landau, L.D., Lifshitz, E.M: Fluid Mechanics, chapter VIII, Butterword and Heinemann, 2nd Ed. (1987)

44. Moock, V.M., Reyes-Ramírez, B., García-Segundo, C., García-Valenzuela, A., Arámbula-Cosio, F., Garduño, E.: Frequency analysis for an extended photoacoustic transport model. Opt. Lett. **40**, pp. 4030–4033 (2015)

45. Madsen, E.L., Hobson, M.A., Frank, G.R., Shi, H., Jiang, J., Hall, T.J., Varghese, T., Doyley, M.M., Weaver, J.B.: Anthropomorphic breast phantoms for testing elastography systems. Ultrasound Med. Biol. **32**, pp. 857–874 (2006)

46. Herman, G.T., Odhner, D.: Performance evaluation of an iterative image reconstruction algorithm for positron emission tomography. IEEE T. Med. Imaging **10**, pp. 336–346 (1991)

47. Schroeder, D.J.: Astronomical Optics, p. 434. Academic Press, San Diego, California, USA (1999)

48. Telenkov, S., Mandelis, A.: Signal-to-noise analysis of biomedical photoacoustic measurements in time and frequency domains. Rev. Sci. Instrum. **81**, pp. 124901-1–7 (2010)

49. Ku, G., Wang, L.V.: Deeply penetrating photoacoustic tomography in biological tissues enhanced with an optical contrast agent. Opt. Lett. **30**, pp. 507–509 (2005)

50. Rosenthal, A., Razansky, D., Ntziachristos, V.: Fast semi-analytical model-based acoustic inversion for quantitative optoacoustic tomography. IEEE T. Med. Imaging **29**, pp. 1275–1285 (2010)

51. Rosenthal, A., Jetzfellner, T., Razansky, D., Ntziachristos, V.: Efficient framework for model-based tomographic image reconstruction using wavelet packets. IEEE T. Med. Imaging **31**, pp. 1346–1357 (2012)

52. White, P.: Using Microphone Polar Patterns Effectively. Sound On Sound: Est. 1985. `http://www.soundonsound.com/sos/mar07/articles/micpatterns.htm` (2007). Accessed 18 August 2014.

53. Gelman, A.: Constrained maximum entropy methods in an image reconstruction method. In: Skilling, J.: Maximum Entropy and Bayesian Methods, pp. 429–435. Kluwer Academic Publishers (1989)

54. Xu, M., Wang, L.V.: Universal back-projection algorithm for photoacoustic tomography. In: Wang, L.V.: Photoacoustic Imaging and Spectroscopy, pp. 37–46. CRC Press, Taylor & Francis Group , Boca Raton, USA (2009)

55. Ammari, H.: Mathematical Modeling in Biomedical Imaging II – Optical, Ultrasound, and Opto-Acoustic Tomographies. Springer, Berlin Heidelberg (2012)

56. Eghtedari, M., Oraevsky, A., Copland, J.A., Kotov, N.A., Conjusteau, A., Motamedi, M.: High sensitivity of in vivo detection of gold nanorods using a laser optoacoustic imaging system. Nano Lett. **7**, pp. 1914–1918 (2007)

57. Wang, L.V.: Photoacoustic Imaging and Spectroscopy. CRC Press, Taylor & Francis Group, Boca Raton, Florida, USA (2009)

Appendix

Scientific publications under my Ph.D. research

1. Moock, V.M., García-Segundo, C., Garduño, E., Arámbula-Cosio, F., Jithin, J., van Es, P., Manohar, S., Steenbergen, W.: Signal processing for photoacoustic tomography. 5th International Congress on Image and Signal Processing (CISP), pp. 957–961, CISP 2012, October 16–18, Chongqing, China (2012)

2. Moock, V.M., Garduño, E., García-Segundo, C., Arámbula-Cosio, F.: Photoacoustic tomography with diffusion approximation. Proceedings of The World Congress on Engineering (WCE) Vol. I, pp. 65–68, WCE 2013, July 3–5, London, U.K. (2013)

3. Moock, V.M., Reyes-Ramírez, B., García-Segundo, C., García-Valenzuela, A., Arámbula-Cosio, F., Garduño, E.: Frequency analysis for an extended photoacoustic transport model. Opt. Lett. **40**, pp. 4030–4033 (2015)

Signal Processing for Photoacoustic Tomography

V. Moock*, C. García-Segundo†, E. Garduño‡, F. Arámbula Cosio,†
J. Jithin§, P. van Es§, S. Manohar§ and W. Steenbergen§

*Posgrado en Ciencia e Ingeniería de la Computación, Universidad Nacional Autónoma de México (UNAM)
Ciudad Universitaria, C.P. 04510, México, D. F., Email: verena.moock@ccadet.unam.mx

†Centro de Ciencias Aplicadas y Desarrollo Tecnológico, UNAM, Circuito Exterior, Apdo. Postal 70-186
‡Instituto de Investigaciones en Matemáticas Aplicadas y en Sistemas, UNAM, Circuito Escolar, Apdo. Postal 20-726
§Biomedical Photonic Imaging Group, MIRA Institute, University of Twente, P.O. Box 217, NL-7500 AE Enschede

Abstract—This study examines one of the open problems yet to solve in photoacoustic tomography: How to prepare photoacoustic signals to ensure interpretation as projection data? The main part of this difficulty is related to the setting of the linear photoacoustic transport model. Notably errors are due to the discrepancy between the mathematical reconstruction and the physical realization: Tomographic image reconstruction from projections require a linear acquisition system. However in practice, the physical reality presents different non-linear phenomena. In account of this incompatibility, it was our purpose to provide some advancement in signal processing for dealing the projection issue while considering different perspectives in the interpretation of the transport model to be applied in a broader manner. Numerical examples are analyzed in detail and unveil the foundations for photoacoustic signal processing methodologies focused on the task of tomographic image reconstruction from projections.

Index Terms—Signal processing techniques for acoustic inverse problems; remote sensing methods, acoustic tomography; ultrasonographic imaging.

PACS numbers: 43.60.Pt; 43.60.Rw; 87.63.dh.

I. Introduction

In the last decade the development of photoacoustic imaging methods has increased, particularly because it is a promising tool for early non-invasive and non-ionizing detection of breast cancer. Photoacoustic images uniquely combine electromagnetic (EM) and ultrasonic (US) information about (biological) objects, e.g. human breast tissue. The operation principle specifies that the object be exposed to infrared radiation with laser pulses, thereby inducing the photoacoustic effect: The absorption of light, while dissipating in a non-radiative manner, produces mechanical disturbances expressed as changes in the pressure distribution. This distribution is confined in time and space and is expressed as a mechanical impulse that is recorded by specific detectors [1] outside the region of interest. Once photoacoustic data is captured, the required projection information therein, in correspondence to the transport model, is deduced via signal processing techniques. Certainly, the common usage of a homogeneous plane wave transport model for photoacoustic applications, as outlined by Wang et al. in

[13], is over-simplified for most biomedical applications. This is in view of assumptions on homogeneous media and negligible influence of viscosity and diffusion. In fact, these assumptions breakdown when imaging real biological tissue such as breasts and corrections have to be incorporated into the model. For instance, posterior sound velocity corrections have to be involved in image processing algorithms, as shown in [7]. Consequently, we need a better analytical description of the photoacoustic transport to reconstruct high-quality images and take effective advantage of the US resolution and EM contrast present in this imaging modality. Notwithstanding, for computed tomography (CT) it is technically unavoidable to approximate registered signals as linear projection data; in accordance with the selected transport model.

This manuscript proposes a method that takes into account viscous and scattering media properties for a linear transport model. Departing from these considerations, our contribution which is partitioned as follows: In section II we describe image reconstruction as an inverse source problem with the aim of identifying the role of the linear transport operator and recall the necessary boundary conditions. Then, in section III we present a new classification of the different linear wave forms with diffraction patterns; these will bring us closer to a more realistic transport description, whenever in practice more precise model conditions can be set up *a priori*. The main section of this study is dedicated to the photoacoustic signal processing methodologies that outline the key part to combine mathematical reconstruction and physical realization. Based on the understanding that reconstruction principles are governed by the same rules that are followed in the US-CT and photon detection from projections, in section V we review the CT strategies designed for modalities with diffraction. The literature in the field of photoacoustic methods mainly utilize backprojection strategies; despite, there are several other tomographic methods; whence reconstruction can be done using many different algorithms. Next we analyze several of these methods, with the aim of determining possibly more efficient reconstruction techniques for photoacoustic imaging.

II. Inverse source problem

The photoacoustic image reconstruction can be considered as an inverse source problem in the sense that the initial pressure distribution $f(\mathbf{x}) = \psi(\mathbf{x}, 0)$ acts as the source; this is provided by electromagnetic absorption, where $\psi : \mathbb{R}^n \times \mathbb{R}_+ \to \mathbb{R}$ and $n \geq 3$ is the spatial dimension. The propagation of this pressure distribution in a linear model allows a description as a homogeneous wave equation in terms of a linear differential operator $\mathcal{L}$ of second order with (temporal gradient) initial conditions,

$$\mathcal{L}\psi(\mathbf{x}, t) = 0 \tag{1}$$
$$\psi(\mathbf{x}, 0) = f(\mathbf{x}) \tag{2}$$
$$\partial_t \psi(\mathbf{x}, 0) = 0. \tag{3}$$

This is applied to photoacoustic imaging, under the assumption that there exists a trace of the forward problem (1-3) that is in correspondence with the ultrasonic sensor registering at the boundary of the observed region Ω,

$$\psi(\overline{\mathbf{x}}, t) = g(t), \quad \overline{\mathbf{x}} \in \partial\Omega. \tag{4}$$

Given the photoacoustic signal $g(t)$ as a damped wave in a possibly inhomogeneous environment, one can make inferences on the constituent terms of the wave equation. The simplest and most used description in accordance with [13] is given by the operator d'Alembert $\square$ acting on the pressure distribution $\psi(\mathbf{x}, t)$; variable in space and time,

$$\mathcal{L}_1 \psi(\mathbf{x}, t) := (\partial_t^2 - \mathbf{c}^2 \nabla^2)\psi(\mathbf{x}, t) =: \square\psi(\mathbf{x}, t), \tag{5}$$

where ∂_t^2 represents the second temporal derivative. Accordingly ∇^2 is the Laplace operator and $\mathbf{c}^2$ is a measure of the sound speed. On applying the principle of Duhamel, the inverse problem in (1-3), to derive the image data $f(\mathbf{x})$, appears as its equivalent version in terms of the following inhomogeneous wave equation (see [10]),

$$\mathcal{L}\psi(\mathbf{x}, t) = f(\mathbf{x})\partial_t \delta(t), \tag{6}$$
$$\partial_t \psi(\mathbf{x}, 0) = 0, \tag{7}$$
$$\psi(\mathbf{x}, t_-) = 0, \quad t_- < 0. \tag{8}$$

Here, δ represents the temporal delta function related to the illumination. For a physically homogeneous medium, the forward solution of the above problem expressed by the operator $\square$ in dimension n turns out to be specified in terms of the spherical Radon transform

$$\psi(\overline{\mathbf{x}}, t) = g(t) \sim \mathcal{R}[f](t). \tag{9}$$

Since the spherical Radon transform has its known inverse operator, analyzed in [5], the inverse problem gets solved. The image data can be reconstructed numerically if sufficiently measurements of the homogeneously illuminated object of interest are taken. Notwithstanding, in practice the inverse problem is ill-conditioned. A physically acceptable, approximate, solution can only be obtained, when *a priori* information is taken into account, satisfying additional constrains, considering instrumental aspects of the acquisition system, as described in [2].

III. Generalization of the transport model

For miscellaneous biomedical applications of photoacoustic imaging it is of interest to achieve a more appropriate linear model of the underlying transport than what the operator $\square$ fulfills; which can include for example viscous and/or scattering media properties. In order to maintain a second order linear model for tomographic reconstructions we present the following extensions:

$$\mathcal{L}_1 := \square, \tag{10}$$
$$\mathcal{L}_2 := \square + \mathbf{v}, \tag{11}$$
$$\mathcal{L}_3 := \square + d, \tag{12}$$
$$\mathcal{L}_4 := \square + \mathbf{v}, + d. \tag{13}$$

The literature focused on the photoacoustic transport problem exhibits that the first instance (10) for plane waves and frequently appears in systems assumed as physically homogeneous. The Boltzmann operator[1] (11) involves a constant $\mathbf{v}$, allowing wave attenuation as a first approximation to the presence of viscosity in the referred system. The Helmholtz operator (12) in turn involves a constant d, accepting wave augmentation as a first approximation for the presence of linear diffusion in the system under study. Both additional contributions are present in the fourth operator[2], related to the Heaviside telegraph equation (13). The latter model symbolizes the most general second order linear photoacoustic transport and is analyzed for the purpose of image reconstruction in [12]. Although, the choice of the above operators will not alter the signal processing routines below, it will somewhat vary the reconstruction conditions.

IV. Photoacoustic signal processing

Photoacoustic signals can be captured by ultrasonic detectors as a time sequence of voltage variations. Figure 1 shows a one-dimensional scan of a sample with two small inhomogeneities over the interval $[0, t_1]$, $t_1 = 72$ μs, at a sample frequency of 80 MHz.
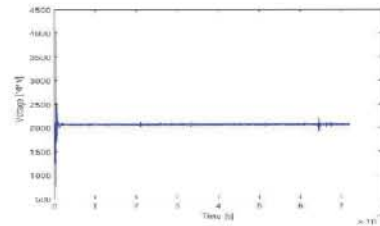

Fig. 1: **D**: Raw data captured by an US detector.

[1] To the best of our knowledge, physical models for photoacoustic and photothermal applications by the presence of continuous conditions present only one of two terms, $\mathbf{v_x}$ o v_t:
$\square + \langle \mathbf{v_x}, \nabla \rangle \overset{\text{cont.}}{\equiv} \square + v_t \partial_t$.

[2] Possibly there is an equivalence relation:
$\square + \langle \mathbf{v_x}, \nabla \rangle + d \overset{\text{cont.}}{\equiv} \square + v_t \partial_t + d$.

In order to improve the low signal-to-noise ratio (SNR) of the photoacoustic raw data is necessary to make some preprocessing. It is already known that the dominant initial peak is related to the voltage source and the direct impact of momentum on the sensor [4]. Since there is little contribution to the photoacoustic information of the region of interest within the time interval $[0, t_0]$, $t_0 = 2.0 \ \mu$s this part was ignored for further processing. Linear trends in the carrier signal were also removed and normalized with respect to atmospheric pressure p_0 2.0mV. For this case study auto-correlation was considered as a useful global technique to improve the SNR; see the result of preprocessing in Figure 2.
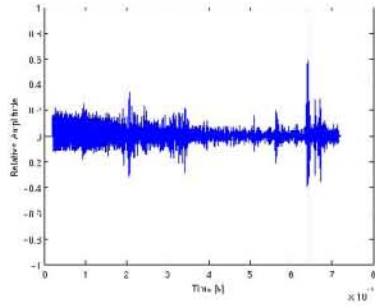

Fig. 3: $\mathbf{D}_0^+ = \text{env}(\mathbf{D}_0)$: Normalized envelope function.

Fig. 2: $\mathbf{D}_0$: Calibration by suppressing the influence of the instrumentation device and auto-correlation.
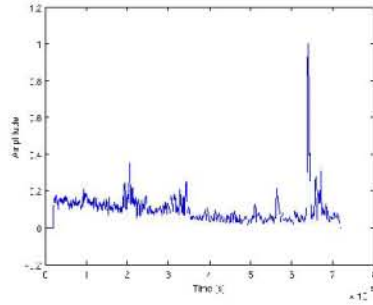
Fig. 4: $\mathbf{D}_0^+ = \text{eff}(\mathbf{D}_0)$: Normalized effective pressure.

The photoacoustic image data are provided by the detector response and become readily accessible for reconstruction after using a global signal processing techniques; miscellaneous are described next:

1) Calculating the envelope function $\text{env}(t)$ as in [11],

$$\text{env}(\mathbf{D}_0) = \mathbf{D}_0 \quad i\mathcal{H}(\mathbf{D}_0) , \qquad (14)$$

with respect to the normalized data $\mathbf{D}_0 = \mathbf{D} \quad p_0$ and the Hilbert transform $\mathcal{H}$, applied to the test data in Figure 3.

2) Calculating the statistical measure of the amplitude variation of the photoacoustic pressure, indicated by the effective sound pressure $\text{eff}(t)$, which is equal to the root mean square (RMS) of the normalized signal $\mathbf{D}_0$,

$$\text{eff}(\mathbf{D}_0) = \sqrt{\frac{\sum_{t_+ = \ v/2}^{v/2} \mathbf{D}_0^2(t + t_+)}{v}}, \qquad (15)$$

where the size of the reference window v, considered when calculating RMS, is set to 21 in the numerical example presented in Figure 4.

3) Rectification of the measured signal [3]: Half wave as well as full wave rectification may be chosen to point out the absolute pressure distribution, see Figure 5.
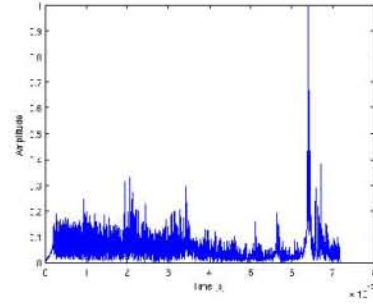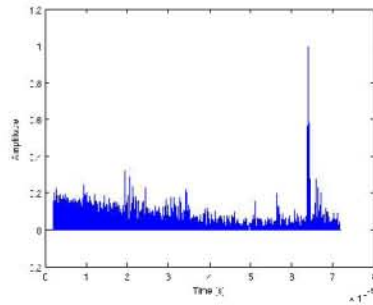

Fig. 5: $\mathbf{D}_0^+$: Normalized half wave rectification.

After successfully applying one of the above filtering methodology, the processed data $\mathbf{D}_0^+$ was further enhanced by thresholding in relation to the estimated value of the SNR. The signal was additionally cleared by convolution with the ideal impulse function, particularly with regard to secondary sampling to carry out the requested image resolution. When all mentioned signal processing is performed, a set that approximates the data g is supplied for finally solving the inverse problem.

V. Tomographic image reconstruction

The fundamentals of computerized tomography are based on the reconstruction from projections. Given the photoacoustic data, the geometry settings for the tomographic reconstruction algorithm have to be in accordance with the projection concept within the photoacoustic model. Consequently, the transport model is restricted to a linear system. Yet, the physical reality may not fulfill the linearity condition. Hence, digital processing routines would be needed to linearize the data for reconstruction purposes.

Once processing true projection data, computerized tomography offers a multitude of reconstruction algorithms. All tomographic methods for images reconstruction can be classified into two groups according to [6]:

(A) Transform-based methods and
(B) Series expansion methods.

These groups particularly differ in the mathematical model of their specification. Transform-based methods are very efficient and fast in operating time. Besides, for linear projections, these algorithms are exact if the system is noise-free. The most intuitive and less complex algorithm is the backprojection routine. Unfortunately, small errors have severe influence on reconstruction results: multiple artifacts in the reconstructed image make a digital biopsy impossible. On the other hand, series expansion methods, mainly typified by ART, also produce exact solutions for the absence of noise. These methods consume more computational resources, but are not restricted to linear models. Corrections to the projection approach can be considered iteratively.

In the following subsections, we show results of implementations of representative algorithms of both families for photoacoustic methods. An adequate phantom for the case study was made of agar where inhomogeneities have been introduced. These local inhomogeneities of different concentrations allow interpretations as tumor propagations. The colorized schema in Figure 6 illustrates the geometric parameters of the experimental setup with a passive element as a primary US source, carried out by [7]. The intention of this figure is also to provide a clearer idea of how the photoacoustic signals are interpreted.

A. Photoacoustic backprojection

Backprojection algorithms are very important techniques for tomographic image reconstruction. The methodology can be considered as the direct numerical application of the inversion formula for the (spherical) Radon transform. Thus, we discretized in (9) the given photoacoustic signal g received by the detector array to the vector $\mathbf{g}$ and interpret that as the integral of the US waves along the aperture, $\mathcal{R}\,\mathbf{f} = \mathbf{g}$ over $L_2(\Omega)$, where $\mathbf{f}$ represents a
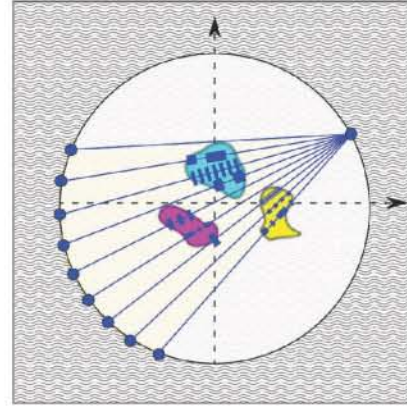

Fig. 6: Phantom, sensor and signal interpretation: high pressure amplitude refers to mayor pressure distribution.

discrete estimate of the image vector. With the aim to get a good approximation, we apply the signal processing as mentioned in section IV and compare their strategies. The reconstruction is performed via iteration over all detector positions and carry out photoacoustic backprojection, very similar to the program for X-rays in [6], but on spherical geometries. The visible cone of each detector element is estimated by the a half-angle of 15 in consideration of [8]. The result with effective pressure signal processing, is shown in Figure 7 for the image resolution of 200   200 pixels. Considerably, the presence of artifacts due to few and erroneous projection data. Justified by the difference between the phantom and test results that, we conclude for backprojection reconstructions from a series of few scans, it is particularly important to implement more accurate or rather corrected signal processing for photoacoustic data.
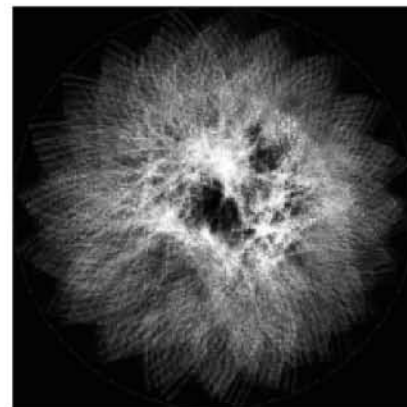

Fig. 7: Examplary photoacoustic backprojection.

B. Photoacoustic ART

ART represents a class of iterative algorithms, not only for image reconstruction from a series of projections, but for solving universal linear systems, and is also known as the Kaczmarz method. In the retrieval of an approximate, physically acceptable solution of the inverse problem ART principally represents a good strategy to attack the ill-posedness of the model. The following notation is consistent with F. Natterer [9], except for changes of letters to be consistent with the previous declaration. Let $A_j f = g_j$ be a system with $A_j : H \quad H_j$ bounded linear operators of Hilbert space H in the Hilbert space H_j, respective to every projection $j = 1, , ..., p$. We resume the model to

$$A = \begin{pmatrix} A_1 \\ \vdots \\ A_p \end{pmatrix}, \quad g = \begin{pmatrix} g_1 \\ \vdots \\ g_p \end{pmatrix}, \quad Af = g.$$

The orthogonal projection P_j in H on the affine subspace $A_j f = g_j$ is given by $P_j f = f + A_j (A_j A_j)^{-1}(g_j \quad A_j f)$. The Kaczmarz procedure with relaxation w (no relaxation if $w = 1$) to solve $Af = g$ is

$$f^{k+1} = P^w f^k, \tag{16}$$

with $P^w = P_p^w ... P_1^w$, $P_j^w = (1 \quad w)\mathbf{I} + wP_j$. The following describes a step explicitly: set $f^{k,0} = f^k$ to compute $f^{k,j}$ for $j = 1, ..., p$ of according to

$$f^{k,j} = f^{k,j\ 1} + \omega A_j (A_j A_j)^{-1}(g_j \quad A_j f^{k,j\ 1}) \tag{17}$$

$$= f^{k,j\ 1} + w \frac{g_j \quad A_j f^{k,j\ 1}}{A_j^{\ 2}} A_j^t, \tag{18}$$

for all $j = 1, ..., p$, and ultimately, we get $f^{k+1} = f^{k,p}$.

The ultimate advantage of ART is its versatility. The method of series expansion is suitable for all scanning geometry and also for problems with incomplete data. ART for $0 < w < 2$ converges to a general solution or to the minimum norm solution of $Af = g$, if the linear system is consistent, see [9]. It should be perceived that $P^w f^k < 1$. Unfortunately, we examine that the actual photoacoustic equation system is ill-posed.

VI. Discussion, conclusions and future work

The problem of how to prepare photoacoustic signals to ensure by signal processing interpretation as projection data for tomographic reconstruction was examined. The contemplated digital methodologies unveil foundations for further improvements on image reconstructions. Still, the discrepancy between mathematical conditions and the physical realization is not balanced so far. Certainly, a proper treatment of photoacoustic signals requires more a sophisticated processing. All presented routines are very versatile tools for many different digital treatments; yet many promising denoising strategies for US signals are left to implement (e.g. wavelet analysis).

For the algorithmic task on image reconstruction (from few projections) we still have to stabilize the convergence on our ART reconstruction results, that suffer on ill-posedness of the problem structure. A mathematical acceptable solution of minimal norm will not solve the reconstruction task in the physical sense. Further regularization techniques (e.g. Tikhonov-Phillips) or similar approximation methods supposably will produce better results, as recommended by [9] for CT in general.

References

[1] A. Guadarrama-Santana C. García-Segundo A. García-Valenzuela B. Reyes-Ramirez, J. G. Bermúdez-Servín. 2d-capacitive-pyroelectric sensor array for photoacoustic detection. Symposium of Photothermal Phenomena, SMCTSM 2012.

[2] M. Bertero and P. Boccacci. *Introduction to Inverse Problems in Imaging*. IOP Publishing Ltd, 2nd ed. edition, 2002.

[3] K.S. Boyle and T.C. Tricas. Pulse sound generation, anterior swim bladder buckling and associated muscle activity in the pyramid butterflyfish, hemitaurichthys polylepis. *J. Exp. Bio.*, 213:3881–3893, 2010.

[4] A.J. Smith C. García-Segundo and J.-P. Connerade. Optically induced non-radiative fast pulses in metals. *J. Mod. Opt.*, 20:233–253, 2004.

[5] S.K. Patch D. Finch and Rakesh. Determining a function from its mean values over a family of spheres. *SIAM J. Math. Anal.*, 35:1213–1240, 2004.

[6] G.T. Herman. *Fundamentals Of Computerized Tomography - Image Reconstruction From Projections*. Advances In Computer Vision And Pattern Recognition. 2nd ed. edition, 2010.

[7] S. Resink-D. Piras J. van Hespen C. Slump W. Steenbergen-T. van Leeuwen J. Jose, R. Willemink and S. Manohar. Passive element enriched photoacoustic computed tomography for simultaneous imaging of acoustic propagation properties and light absorption. *Opt. Express*, pages 2093–2104, 2010.

[8] D.H. Johnson and D.E. Dudgeon. *Array Signal Processing, Concepts And Techniques*. Prentice Hall Signal Processing Series. 1993.

[9] F. Natterer and F. Wübbeling. *Mathematical Methods In Image Reconstruction*. Monographs on Mathematical Modeling and Computation. SIAM, 2001.

[10] H. Grün M. Haltmeier P. Burgholzer, J. Bauer-Marschallinger and G. Paltauf. Temporal back-projection algorithms for photoacoustic tomography with integrating line detectors. *Inverse Problems*, 23:S65–S80, 2007.

[11] T.O. Müller R. Liu R. Stotzka, N.V. Ruiter and H. Gemmeke. High resolution image reconstruction in ultrasound computer tomography using deconvolution. *SPIE Med. Imaging*, 2005.

[12] E. Garduño V. Moock, C. García-Segundo and F. Arámbula Cosio. Classification of diffusion transport models for reconstruction from projections. In preparation for submission.

[13] M. Xu and L.V. Wang. Photoacoustic imaging in biomedicine. *Review of Scientific Instruments*, 66:1–20, 2006.

Photoacoustic Tomography with Diffusion Approximation

Verena M. Moock, Edgar Garduño, Crescencio García-Segundo, and Fernando Arámbula Cosio

Abstract—A framework is presented for identifying projection information in photoacoustic measurements under a diffusion approximation for tomographic image reconstruction. We propose to solve the inverse problem with respect to a thermoelastic wave transport. By means of a numerical simulation, we examine how our diffusion model relates to the signal registration and deduce an adjustment on small animal image reconstruction.

Index Terms—inverse problem, diffusion approximation, photoacoustic imaging.

I. Introduction

THERE is considerable interest on biomedical image reconstruction with photoacoustic data due to its non-invasive and non-ionizing testing utilization opportunities. Photoacoustic tomography is a hybrid image modality referring to electromagnetic (EM) energy absorption and sound generation within the object of interest. Ideally, acoustic detectors, positioned on the perimeter of the object, register projection information of the EM energy absorption map. In case of an acoustically homogeneous media the underlying transport is commonly modeled in terms of a plane wave propagation [1]. This model approach facilitates the solution of the inverse problem tremendously. One possible solution is obtained by applying the inverse (spherical) Radon transform to the measured data, and the source gets backprojected. In a recent study [2], the author works on a wave transport model incorporating an attenuation approximation in such a way that the Radon inversion is still a reliable solution. This efficient strategy no longer uses the raw detector measurement, but treated data, which approximates projection information under the consideration of attenuation.

The thermoelastic expansion, intrinsic to the photoacoustic effect, generally constitutes the inhomogeneous part of the wave equation. In this article we make the conjecture, that the transport may correspond to the thermoelastic wave equation, inspired by heat waves [3], and as a consequence we present a novel approach

V. M. Moock is with the Postgraduate Program in Computer Science and Engineering, Universidad Nacional Autónoma de México (UNAM), 04510 México, D.F., e-mail: verena.moock@ccadet.unam.mx.

E. Garduño is with the Instituto de Investigaciones en Matemáticas Aplicadas y en Sistemas, UNAM, Circuito Escolar, Ciudad Universitaria, Apdo. Postal 20-726, 04510 México, D.F., e-mail: edgargar@ieee.org.

C. García-Segundo and F. Arámbula Cosio are with the Centro de Ciencias Aplicadas y Desarrollo Tecnológico, UNAM, Circuito Exterior, Ciudad Universitaria, Apdo. Postal 70-186, 04510 México, D.F., e-mail: crescencio.garcia@ccadet.unam.mx, fernando.arambula@ccadet.unam.mx.

on photoacoustic image reconstruction with a diffusion approximation. Then, we analyze the model estimation in accordance to the findings in [2] and we apply the results on the photoacoustic section image reconstructions.

This paper is organized as follows: In section II, we present a conceptual model linking of thermoelastic wave transport to photoacoustic image reconstruction in terms of an inverse problem. As the underpinning issue of this work, we propose a model extension for photoacoustic methods with a diffusion approximation. Along with the suggested wave equation, we present in section III the common backprojection approach applied on a phantom, mimicking the zebra-fish case study of [4], referring to both plane wave and thermoelastic wave model. Furthermore, we outline a strategy for a numerical inversion with diffusion. In section IV, we deduce an adjustment of the zebra-fish section image reconstruction and express the visual results. Finally, we outline our conclusion in section V and reveal implications for biomedical image reconstruction.

II. The extended photoacoustic inverse Problem

In this section, we present a conceptual model linking of photoacoustic methods to tomographic image reconstruction in its mathematical formulation as an inverse problem. Thereby, we deduce a new photoacoustic transport approximation inspired by heat waves [3], that permits general interpretations in the broader domain of diffraction tomography.

The photoacoustic transport can be described in terms of a system of partial differential equations by modeling a specific transport acting on the pressure distribution function $p : \mathbb{R}^n \times \mathbb{R} \to \mathbb{R}_+$ over space and time. In case that the source, or rather the initial distribution $f(\mathbf{x}) = p(\mathbf{x}, 0)$ is a weakly scattering or small object, the occurring phenomena allow an approximation of the transport in free space expressed by a linear integral equation of second order with initial (functional and temporal gradient) conditions, $\forall \mathbf{x} \in \mathbb{R}^n$ and $\forall t \in \mathbb{R}$,

$$\mathcal{L}p(\mathbf{x}, t) = 0 \tag{1}$$
$$p(\mathbf{x}, 0) = f(\mathbf{x}) \tag{2}$$
$$\partial_t p(\mathbf{x}, 0) = 0. \tag{3}$$

The homogeneous linear differential equation (1) reveals an acoustic homogeneous media under stress confinement. By the principle of Duhamel the system (1-3) has an equivalent inhomogeneous version [5],

$$\mathcal{L}p(\mathbf{x},t) \;=\; f(\mathbf{x})\partial_t \delta(t), \qquad (4)$$

$$\partial_t p(\mathbf{x},0) \;=\; 0, \qquad (5)$$

$$p(\mathbf{x},t_-) \;=\; 0, \quad \forall t_- < 0, \qquad (6)$$

where δ represents the temporal delta function related to the illumination. In photoacoustic tomography it is assumed that for any source f there exists a trace g of the forward problem that corresponds to what sensors register at the boundary of the observed region Ω over a fixed time interval $t \in [0,T]$,

$$p(\mathbf{y},t) = g(t), \quad \mathbf{y} \in \partial\Omega. \qquad (7)$$

Photoacoustic imaging in a homogeneous and non-attenuating environment is usually based on a plane wave transport according to [1], and is modeled by the linear d'Alembert operator $\Box$ (including the Laplace operator ∇^2) and a constant wave speed c,

$$\mathcal{L}_0 p_0(\mathbf{x},t) := \Box p_0(\mathbf{x},t) = (\partial_t^2 - c^2\nabla^2)p_0(\mathbf{x},t). \qquad (8)$$

The associated inverse problem can be expressed in terms of the (spherical) Radon transform

$$\mathcal{R}f = g, \qquad (9)$$

where the actual integrating geometry varies with the detector shape. The inverse operator is known [6], hence the problem can be solved numerically.

"Nowadays, there is a trend to incorporate more and more modelling into photoacoustics" [7]. For miscellaneous applications of photoacoustic methods on non-homogeneous media we propose to consider the thermoelastic wave equation:

$$\mathcal{L}_d p_d(\mathbf{x},t) := \Box p_d(\mathbf{x},t) + d(t) * \partial_t p_d(\mathbf{x},t), \qquad (10)$$

introducing the weight function d for the gradient transport. This diffusion approach should not be ignored when heat propagation is considerable in the experimental analysis. A feasible approach to estimate the appropriate weights is done by optimizing

$$\{d : [0,T] \to \mathbb{C} \mid \min_{t \in [0,T]} \|d(t)\partial_t g(t) + \partial_t^2 g(t)\|_2\}. \qquad (11)$$

From a point of view of the model description (4-6) we can compare both waveform expressions in the Fourier space,

$$(c^2\nabla^2 + \omega^2)\hat{p}_0(\mathbf{x},\omega) \;=\; \frac{i\omega}{\sqrt{2\pi}} f(\mathbf{x}), \quad (12)$$

$$(c^2\nabla^2 + \omega^2 - i\omega\hat{d}(\omega))\hat{p}_d(\mathbf{x},\omega) \;=\; \frac{i\omega}{\sqrt{2\pi}} f(\mathbf{x}), \quad (13)$$

and obtain the following relation on the measurements at the boundary $g_0(t) = p_0(\mathbf{x},t)$, $g_d(t) = p_d(\mathbf{x},t)$ for $\mathbf{x} \in \partial\Omega$

$$\hat{g}_0(K(\omega)) = \frac{K(\omega)}{\omega}\hat{g}_d(\omega), \qquad (14)$$

with $K(\omega) = \sqrt{\omega^2 - i\omega\hat{d}(\omega)}$. Hence, the issue is to estimate g_0 from g_d using the relationship $g_d = \mathcal{T}g_0$, where $\mathcal{T}$ under the consideration of (14) is defined by

$$\mathcal{T}g_0(t) = \frac{1}{2\pi}\int_{\mathbb{R}} \frac{\omega}{K(\omega)} e^{i\omega t} \int_0^T g_0(t')e^{-iK(\omega)t'}dt'd\omega. \qquad (15)$$
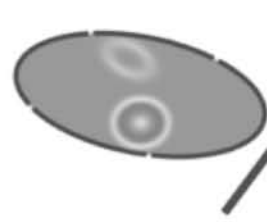
Figure 1: Schematic absorption map of a zebra fish.

We apply the strategy of [2] and solve the inverse problem by performing the following instructions:

1) Given the measurement g_d in a physical environment modelled by $\mathcal{L}_d p_d = 0$, estimate $g_0 = \mathcal{T}^{-1}g_d$.
2) Perform backprojection with respect to the adjusted projection data $\mathcal{T}^{-1}g_d$.

We carry out the inversion of the integral in (15) using an appropriate discretization and the Singular Value Decomposition (SVD) approach in the interest of succeeding the inversion of the ill-conditioned matrix representing $\mathcal{T}$.

III. Forward simulations and backprojection

We perform a numerical simulation of both plane wave and thermoelastic wave transport on a two-dimensional phantom, mimicking the zebra-fish case study of [4] and predict the sinogram information (forward problem). Moreover, we illustrate how errors, due to inappropriate projection approximation, can affect the reconstruction quality.

Figure 1 illustrates a simple musculoskeletal and digestive atlas of a zebra-fish axial cross-section, representing by different gray levels distinct regions of the EM energy absorption. If the absorption map can be considered as nearly acoustically homogeneous, we may simulate the photoacoustic forward and inverse problem i.e. with a cylindrical detector assuming a plane wave transport as in (8). The result is demonstrated in Figure 2. In case of a large number of projections, equally distributed around the object of interest, reconstruction artifacts are essentially insignificant. However, when diffusion alters the transport, as indicated by the thermoelastic wave equation (10), measurements approximate projections whose information content is not correctly interpreted, or rather the Radon transform is erroneously applied to the source. Figure 3 illustrates sinogram and the backprojection result when $K(\omega)$ is approximated by $\omega - 1/2cd\omega^3$ with constant $d = -0.02$. Interference artifacts, apparently weighted by the absorption coefficients, distort the image reconstruction. However, we are able to correct this impact by applying the inverse Radon transform on the transformed data $\mathcal{T}^{-1}g_d$. The reconstruction quality is expected to be as good as in Figure 2.
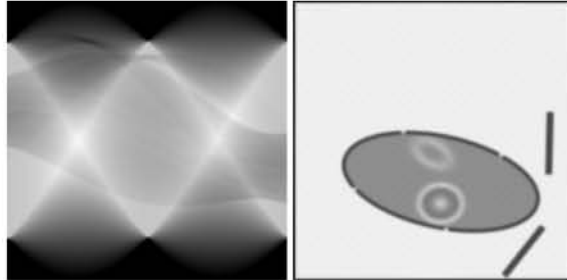
Figure 2: Projection approximation g_0 and the inverse solution $f_0 = \mathcal{R}^{-1}g_0 \approx f$ under a plane wave transport.
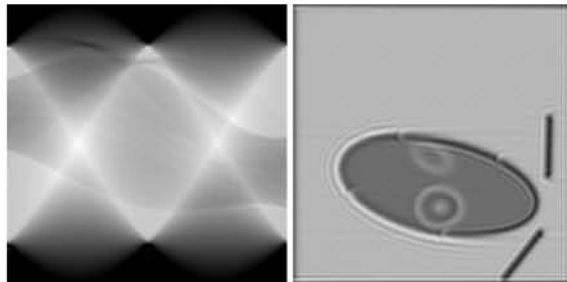

Figure 3: Projection approximation g_d and the inverse solution $f_d = \mathcal{R}^{-1}g_d$ under a diffusive transport.
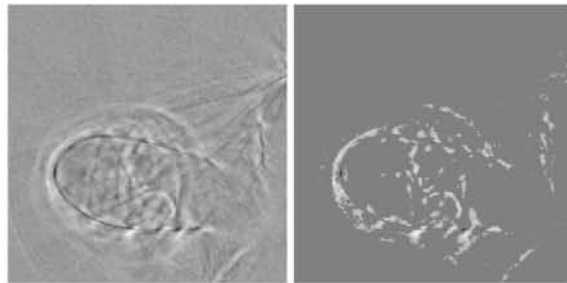

Figure 4: Backprojection $\mathcal{R}^{-1}g_d$ and its windowed image over the intervals $[0.0, 0.3]$ and $[0.7, 1.0]$.
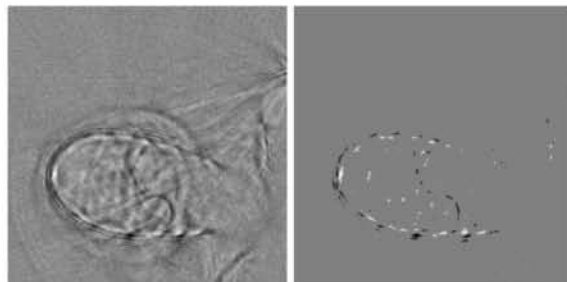

Figure 5: Backprojection $\mathcal{R}^{-1}(\mathcal{T}^{-1}g_d)$ and its windowed image over the intervals $[0.0, 0.3]$ and $[0.7, 1.0]$.

IV. Adjusted biological section image reconstruction

The purpose of this section is to evaluate how an adjusted projection approximation with the diffusion approach simulated previously will alter the reconstruction result. Hence, we compare the registered sinogram of a real zebra-fish axial cross-section and its $\mathcal{T}$-Transformation and their normalized backprojection images in Figure 4 and Figure 5. Since both reconstructions do not reveal the essential differences at a first sight, we also visualize a windowed image and filter out normalized signal values of the interval $[0.3, 0.7]$ that are finally mapped on the neutral value 0.5.

Visual results

We observe that by applying the projection adjustment the well-defined body shape and the zebra-lines of the fish become more fitted and clear. Nonetheless, it is noticeable that poor absorption signals, e.g. from the pelvic fins or the digestive region, suffer the signal processing and disappear up to some extent.

V. Conclusions

We conclude from our results that a projection adjustment provide profitable advantages for small animal tomographic experiments, when the scientific study involves a (rough) segmentation problem. The particular benefit of the present adjustment technique is that the diffusion transformation is only applied once on the measurement, hence it does not imply extra computational reconstruction efforts.

We have demonstrated that the proposed photoacoustic transport model extension is a valid approach to improve tomographic image reconstruction in the presence of acoustic heterogeneities. Indeed, the present case study is a first application approach that apparently does not present a significant thermoelastic wave transport. That is why the constant diffusion parameter d in (14) has to be held small, and consequently backprojection results in Figure 4 and Figure 5 look very similar. Probably this adjustment strategy may interfere even better on photoacoustic tomography of more diffusive media. Our future expectation is to apply the model to some larger volumes and thus proceed refining the methodology. It remains an open problem to complete the transport equation in order to improve image reconstruction results.

Acknowledgment

References

[1] M. Xu, and L.V. Wang, "Photoacoustic Imaging In Biomedicine," *Review of Scientific Instruments*, vol. 66, 2006.
[2] H. Ammari, "Mathematical Modeling in Biomedical Imaging II - Optical, Ultrasound, and Opto-Acoustic Tomographies," Springer-Verlag Berlin Heidelberg, 2012.
[3] D.D. Joseph, and L. Preziosi, "Heat waves," *Reviews of Modern Physics*, vol. 61, 1988.
[4] S. Gratt, K. Passler, R. Nuster, and G. Paltauf, "Photoacoustic section imaging with an integrating cylindrical detector," *Biomedical Optics Express*, vol. 2, pp. 2973-2981, 2011.
[5] P. Burgholzer, J. Bauer-Marschallinger, H. Grün, M. Haltmeier, and G. Paltauf, "Temporal Back-Projection Algorithms For Photoacoustic Tomography With Integrating Line Detectors," *Inverse Problems*, vol. 23, pp. S65-S80, 2007.
[6] D. Finch, S.K. Patch, and Rakesh, "Determining A Function From Its Mean Values Over A Family Of Spheres," *SIAM J. Math. Anal.*, vol. 35, pp. 1213-1240, 2004.
[7] R. Kowar, and O. Scherzer, "Photoacoustic Imaging Taking Into Account Attenuation," *math.AP*, pp. 1-49, 2010.

Optics Letters

Frequency analysis for an extended photoacoustic transport model

V. M. Moock,[1] **B. Reyes-Ramírez,**[2] **C. García-Segundo,**[2,*] **A. García-Valenzuela,**[2] **F. Arámbula-Cosio,**[2] **and E. Garduño**[3]

[1]*Posgrado de Ciencia e Ingeniería de la Computación, Universidad Nacional Autónoma de México, Circuito de Posgrados S/N, Bldg. C, Ciudad Universitaria, D.F. 04510, Mexico*
[2]*Centro de Ciencias Aplicadas y Desarrollo Tecnológico, Universidad Nacional Autónoma de México, Circuito Exterior S/N, P.O. Box 70-186, Ciudad Universitaria, D.F. 04510, Mexico*
[3]*Instituto de Investigaciones en Matemáticas Aplicadas y en Sistemas, Circuito Escolar S/N, P.O. Box 20-725, Universidad Nacional Autónoma de México, Ciudad Universitaria, D.F. 04510, Mexico*
Corresponding author: crescencio.garcia@ccadet.unam.mx

In photoacoustic imaging, the signal attenuation is a well-known source of artifacts over the image reconstruction. It is recognized that this is caused by optical absorption effects and by the ultrasound broadband scattering. However, the sound dispersion is generally neglected, although it appears notably in thick or heterogeneous tissues. In the present Letter, we give an experimental example in which both attenuation and sound dispersion are dealt with as relevant features to be taken into consideration. An analytic perspective of these perturbations leads us to a waveform transport-model extension that provides a linear description of the induced acoustic effects. We find a near match between the theoretical predictions and the experimental results in the frequency domain. These outcomes approximate projection data that represent forward solutions in photoacoustic image reconstruction. © 2015 Optical Society of America

OCIS codes: (060.2630) Frequency modulation; (070.7345) Wave propagation; (110.5125) Photoacoustics; (260.2030) Dispersion.

http://dx.doi.org/10.1364/OL.40.004030

Efforts in photoacoustic (PA) image applications, such as computerized tomography, are focused on reducing image blurring, signal attenuation, and acoustic reflections, mainly because these artifacts are notably present when reconstructing thick or acoustically heterogeneous media, i.e., where the acoustic impedance is not necessarily constant. Contributions range from experimental procedures [1–3] to theoretical and computational algorithms, including the introduction of frequency-domain PA imaging analysis [4–6] and error minimization, in which the plane wave transport is used as a first approximation [7–9]. Further approaches compensate attenuation at a stage prior to the image formation [10–13] or use a nonuniform sound speed [14]. However, little attention has been dedicated for transport adjustments on sound dispersion of the PA components. This dispersion can be due to depth of the PA

source (>1 cm) and by effective heterogeneities of the tissue. In addition, since the bandwidth of PA signals, compared to conventional medical ultrasound imaging, is substantially broader, then dispersion features are likely to be unmasked. Consequently, it is important incorporating sound dispersion (or rather acoustic impedance) as an important factor in PA models. Dealing with sound perturbations is particularly important when reconstructing images, because they produce artifacts, such as contour reflections and blurring. By using large bandwidth admittance sensors for registering the PA signals, the magnitude of these artifacts increases together with the heterogeneity of the sample and its apparent thickness. PA transport models using monochromatic plane waves fail to satisfactorily account for the artifacts induced by the sound dispersion; see [15]. By visualizing PA measurements in the frequency domain, it is easier to understand the modulations of the impulse response of a medium [9,10,16]. Accordingly, we designed our experiments to produce PA data whose visualization display both acoustic dispersion and attenuation. Further, we design a waveform-transport model extension to predict analytically these phenomena. As a consistency test, we verify the match between the theoretical predictions and the experimental results. To conclude the transport extension, we propose a linear adjustment that applies at a stage prior to solving the inverse problem of image reconstruction. This represents an improved approximation for the reconstruction of the PA source out of the registered projections.

For our experiments, we used as targets neoprene slices, all of them 1.5 mm in thickness (N) and located inside of phantoms of polyvinyl alcohol (PVA) [17] immersed in still water. For these phantoms, we created three cubic samples measuring 45 mm wide, 10 mm tall, and 9 mm, 14 mm and 19 mm long (D), respectively; see the upper-right box of Fig. 1. To obtain our measurements, we used a low-noise capacitive transducer (S) of polyvinylidene fluoride (PVDF) operating in piezoelectric mode that we placed on one side of the phantom, along its length and at a distance (L) of 20 mm from the edge of the
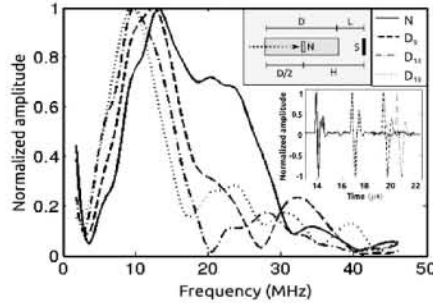
Fig. 1. Experimental PA response in the frequency domain. The bandwidths exhibit the differences between the PA signals for laser pulses impinging on a 1.5-mm-thick neoprene slice (N) alone (continuous line), and those for the same type of neoprene slab centered within PVA phantoms measuring $D = 9$ mm, 14 mm, and 19 mm long (dashed, dash-dotted and dotted lines), respectively. The PA sensor (S) was placed at fixed distance of 20 mm (L) from the phantom. The inset curves correspond to the time domain PA response.

phantom. The laser source is a pulsed Nd:YAG laser-emitting pulses of ∼7 ns time-width at a wavelength of 1064 nm and rate repetition of 10 Hz. The triggered photo-acoustic signal travels across the phantom length, plus 20 mm in water, before being read out by the detector S [18]. In Fig. 1, we present the response in the frequency domain of four experimental cases: that from a neoprene slab of 1.5 mm thickness (N), i.e., the source free from dispersion and attenuation; the three remaining cases are obtained from similar 1.5-mm-thick neoprene slabs embedded right at the half of the length of the PVA phantoms, $D/2$. The output curves are correspondingly labeled as D_9, D_{14}, and D_{19}. For schematic details see the inset in Fig. 1. The experiments were made such that the sensor and the phantoms were kept immersed in water. Notice that the distance L from the end face of the phantom to the sensor was kept constant during the experiments. We took care that the neoprene's interaction area and the transducer's sensing area were parallel, while the laser excitation and, thus, the photoacoustic signal propagation were set to be perpendicular to these areas. Full experimental details can be seen in [18,19]. In Fig. 1, we can appreciate frequency shifts and time-pulse-width differences between the nondispersive and the dispersive cases. The distinct bandwidth distributions are due to the dispersion experienced by the PA signals; here, for purposes of visual presentation, the curves are normalized. The above description and the examples in [18,19] suggest that acoustical attenuation and dispersion are perturbations that necessarily appear in tomographic image reconstruction. At the following stage, we analyze how these can be included within the transport model.

A mathematically well-stated transport description through weakly scattering media or small objects, as it is the case with the probed phantoms, can be expressed by a linear integral equation of second order with initial Cauchy conditions (related to the functional and to the temporal gradient): $\forall \mathbf{x} \in \mathbb{R}^n$ and $\forall t \in \mathbb{R}$,

$$\mathcal{L}p(\mathbf{x}, t) = 0, \tag{1}$$

$$p(\mathbf{x}, 0) = f(\mathbf{x}), \tag{2}$$

$$\partial_t p(\mathbf{x}, 0) = 0. \tag{3}$$

Here $\mathcal{L}$ is a linear wave operator acting on the acoustic pressure-distribution function $p{:}\mathbb{R}^n \times \mathbb{R} \to \mathbb{R}_+$ over space and time. In imaging, the forward problem refers to finding the projection data of the PA source f

$$g(t) = p(\mathbf{y}, t), \qquad \mathbf{y} \in \partial\Omega \tag{4}$$

that is registered by sensors at the boundary of the observed closed and bounded region Ω over a fixed time interval $t \in [0, T]$. For reconstructing images, this problem is stated inversely: given $g(t)$ of Eq. (4), find the initial pressure distribution f. If the projection scheme holds, the inverse problem can be solved by known computerized tomography strategies, e.g., backprojection.

Upon reviewing transport models on the wider field of waveform tomography related to Eqs. (1)–(4) for compatible attenuation and dispersion aspects, we recognize two distinct classes for homogeneous and heterogeneous media under Duhamel's principle. These problem classes differ by their linear operator $\mathcal{L}$ and analytical form of the involved differentials on the distribution function p. Thus, PA imaging of homogeneous and nonattenuating media is commonly based on a plane wave transport [3,10,16], which is modeled by $(1/c^2\partial_t^2 - \nabla^2)$, where ∇^2 is the Laplace operator and c the constant wave speed. When $c = 1$, the linear wave operator results in

$$\mathcal{L}_0 p_0 \equiv (\partial_t^2 - \nabla^2)p_0. \tag{5}$$

In the current contribution, we work out an extension to the dispersive waveform transport of optical tomography [20] by incorporating the attenuation approach of ultrasound for PA propagation in dispersive, acoustically perturbing media [10], by means of the Heaviside telegraph equation,

$$\mathcal{L}_{a,d} p_{a,d} \equiv (\partial_t^2 - \nabla^2)p_{a,d} + d * \partial_t p_{a,d} + a * p_{a,d}. \tag{6}$$

Here $*$ denotes the convolution between two functions. This operator combines the wave enhancement with diffusive attenuation and represents a more-realistic transport description. The analytic estimation of the functions of attenuation, $a(t)$, and dispersion, $d(t)$, has to account for the limitations reviewed in [1]. However, the resulting transport model including perturbations $\mathcal{L}_{a,d}$ does not represent a projection scheme; therefore, reconstruction algorithms from projections are not feasible. To sort out this inconvenience, the authors of [2,10] provide the strategy of inverting the attenuation to approximate the projection data.

We follow an analog approach to [10] by modeling the photoacoustic transport with a sound-dispersion approximation and attenuation with the operator $\mathcal{L}_{a,d}$ in Eq. (6). Our reference is the wave equation (5) under the consideration of the initial conditions and the Duhamel's principle (e.g., [21]). Taking its Fourier transform (symbolized by ^) in terms of the frequency-dependent pressure results in the following relations:

$$(\nabla^2 + \omega^2)\hat{p}_0(\mathbf{x}, \omega) = \frac{i\omega}{\sqrt{2\pi}}f(\mathbf{x}), \tag{7}$$

$$(\nabla^2 + \omega^2 - i\omega\hat{d}(\omega) - \hat{a}(\omega))\hat{p}_{a,d}(\mathbf{x}, \omega) = \frac{i\omega}{\sqrt{2\pi}}f(\mathbf{x}). \tag{8}$$

In conformity with the previous equations, we derive the measurements at the boundary for $\mathbf{y} \in \delta\Omega$ in the Fourier space, in

the juxtaposition from the homogeneous to the heterogeneous case

$$\hat{g}_0(k(\omega)) = \frac{k(\omega)}{\omega}\hat{g}_{a,d}(\omega), \tag{9}$$

with $g_0(t) = p_0(\mathbf{y}, t)$ and $g_{a,d}(t) = p_{a,d}(\mathbf{y}, t)$ in the Euclidean space and

$$k(\omega) = \sqrt{\omega^2 - i\omega\hat{d}(\omega) - \hat{a}(\omega)}. \tag{10}$$

The novelty in obtaining a better projection approximation in attenuating and dispersive media is now achieved via the estimation of g_0 from $g_{a,d}$ with respect to the relationship $g_{a,d} = \mathcal{T}g_0$, where $\mathcal{T}$ is defined by

$$\mathcal{T}g_0(t) = \frac{1}{2\pi}\int_{-\infty}^{\infty}\frac{\omega}{k(\omega)}\exp(i\omega t)\mathcal{I}_t(\omega)\mathrm{d}\omega, \tag{11}$$

with $\mathcal{I}_t(\omega) = \int_0^T g_0(t)\exp(-ik(\omega)t)\mathrm{d}t$. This solution strategy is similar to this introduced in [22] and later generalized in [10–12].

For a homogeneous (HM) thermo-viscous medium with sound absorption, the wave number and frequency are related as $k(\omega) = \omega/\sqrt{1 - i\alpha_{\mathrm{HM}}\omega}$; with α_{HM} the attenuation coefficient [10,23]. However, for heterogeneous (HT) medium, the wave number has an additional term due to the first-order derivative. Hence for consistency with the HM case, (10) can be rearranged and series expanded at first order to recover the mathematical structure. Though a coefficient $\alpha_{\mathrm{HT}}(\omega) \in \mathbb{C}$ is introduced, and for consistency with [10] and [23], we change variables, such that $\hat{d}(\omega) = -\omega^2\tilde{a}$ and $\hat{a}(\omega) = \omega^4\tilde{d}$, and after approximations, we get

$$k(\omega) = \omega + \frac{1}{2}[i\tilde{a}\omega^2 - \tilde{d}\omega^3], \tag{12}$$

where $\tilde{a}, \tilde{d} \in \mathbb{R}$ are empirical factors. In relationship with the experimental outcome, we suppose that the response of the neoprene N approximates projection data of a rectangular function, then in correspondence $\hat{g}_0$ comes up to an absolute sinc function. The solid line in Fig. 2 shows this output. For the neoprene, N, hidden within the three PVA blocks
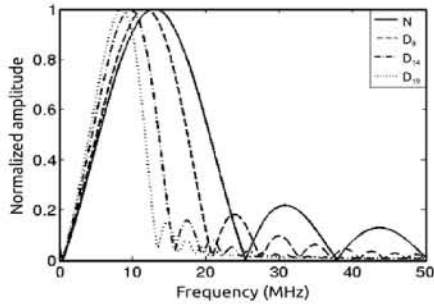

Fig. 2. Theoretical outcome for the PA frequency response is phenomenologically in near correspondence with the experimental observations. See main text for parametric details. The considered cases are: $\hat{g}_0$ (continuous line), approximating N, and three implementations of $\hat{g}_{a,d}$ with distinct factors $\tilde{a}$ and $\tilde{d}$; $\tilde{a}_9 = \tilde{d}_9 = -0.001$ model D_9 (dashed line), $\tilde{a}_{14} = \tilde{d}_{14} = -0.005$ model D_{14} (dash-dotted line), and $\tilde{a}_{19} = \tilde{d}_{19} = -0.01$ model D_{19} (dotted line).

(D_9, D_{14}, D_{19}), we discretized the transport $\mathcal{T}$ in Eq. (11). Given the PVA phantoms D_9, D_{14}, D_{19}, we deduce the empirical factors for the perturbation in the sample: $\tilde{a}_9 = \tilde{d}_9 = -0.001$, $\tilde{a}_{14} = \tilde{d}_{14} = -0.005$, and $\tilde{a}_{19} = \tilde{d}_{19} = -0.01$. These values are the results of a line search algorithm, which gives the local minimal differences between the experimental and theoretical curves. The resulting frequency PA outcome is also presented in Fig. 2, being the dashed line for D_9, the dash-dotted line for D_{14}, and the dotted line for D_{19}. A comparative display between the experimental and the analytic curves in terms of acoustic dispersion features is shown in Fig. 3. The abscissa corresponds to the PVA length, recalling that in each case, the hidden target is placed at the middle of this length. The left ordinate in blue for frequency maxims has to be distinguished from the right ordinate in red, referencing the mean bandwidths. The dashed lines refer to the experimental results, while the continuous lines stand for the analytic results.

The previous analysis allows the setup of an analytic description of how to invert the effect of acoustic perturbations within the measurements and deduce less-erroneous projection data to feed computerized tomographic algorithms. To prevent an ill-conditioned linear system, the inversion of the transport $\mathcal{T}$ can be carried out by numerical calculations such as the singular value decomposition (SVD). SVD approximates $\mathcal{T}$ by the matrix product $T = \mathbf{U}\mathbf{S}\mathbf{V}^t$ where $\mathbf{U}, \mathbf{V}$ are real or complex unitary matrices, ($\mathbf{V}^t$ symbolizes the transpose of the matrix $\mathbf{V}$), and $\mathbf{S}$ is a rectangular diagonal matrix. For a positive real number $\varepsilon > 0$, we can obtain an approximation of its inverse according to

$$g_0 \approx T_{1,\varepsilon}^{-1}g_{a,d} = \sum_j \frac{\sigma_j}{\sigma_j^2 + \varepsilon^2}\langle g_{a,d}, V_j\rangle U_j, \tag{13}$$

with $\mathbf{U}_j, \mathbf{V}_j^t$ representing the jth row of matrices $\mathbf{U}, \mathbf{V}^t$, respectively, and σ_j, for all pixel indexes $1 \leq j \leq J$, are nonnegative real singular values. In this way, it is immediate that by SVD, one solves the forward problem, by approximating projections $g_0 = T^{-1}g_{a,d}$, being that these fit better a linear PA transport and contain attenuation and dispersion components.

The significance of attenuation and sound dispersion over the transport of PA signals before their detection is clearly
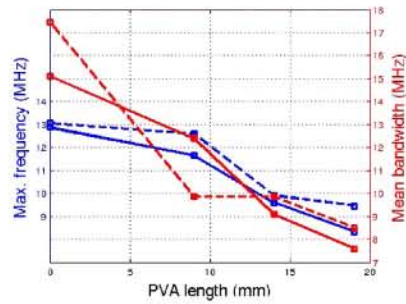

Fig. 3. Frequency maxims (blue, right ordinate) and the mean bandwidths (red, left ordinate) of the experimental results (dashed line) and the model prediction (continuous line). The abscissa refers to the PVA phantom length. For each case, the target N is at the half of this length (see inset in Fig. 1).

exhibited from the frequency analysis of the experiments. This lends support for the presented mathematical model with numerical approximations to establish a phenomenological interpretation and realistic output representation of the experimental phenomenon. From the present analysis, it is unveiled that PA common image reconstruction algorithms misinterpret the sensor response as simple projection output. Our proposal of modeling the PA transport with the Heaviside telegraph equation (6) provides the conditions to ensure that the acquired data have a close match with perturbed acoustic signals and are further invertible. By means of using the numerical approximation to set up the coefficients $\tilde{a}_j$ and $\tilde{d}_j$ ($j = 9$, 14 and 19), we achieved to exhibit that indeed the change in depth of the hidden target clearly induces acoustic dispersion and how it can be described (see Fig. 3). This prompted us to manage a better projection approximation, Eq. (11). The analytic representation of these coefficients is matter of our current research efforts.

REFERENCES

1. M. Xu and L. V. Wang, Phys. Rev. E **67**, 056605 (2003).
2. A. Ishimaru, Proc. IEEE **79**, 1359 (1991).
3. K. Maslov and L. V. Wang, J. Biomed. Opt. **13**, 024006 (2008).
4. B. Lashkari and A. Mandelis, J. Acoust. Soc. Am. **130**, 1313 (2011).
5. S. A. Telenkov and A. Mandelis, J. Biomed. Opt. **11**, 044006 (2006).
6. B. Lashkari and A. Mandelis, J. Biomed. Opt. **19**, 036015 (2014).
7. A. I. Nachman, J. F. Smith, and R. C. Waag, J. Acoust. Soc. Am. **88**, 1584 (1990).
8. H. Grün, R. Nuster, G. Paltauf, M. Haltmeier, and P. Burgholzer, Proc. SPIE **6856**, 685620 (2008).
9. J. Jose, R. G. H. Willemink, W. Steenbergen, C. H. Slump, T. G. van Leeuwen, and S. Manohar, Med. Phys. **39**, 7262 (2012).
10. H. Ammari, E. Bretin, V. Jugnon, and A. Wahab, in *Mathematical Modeling in Biomedical Imaging II*, Vol. **2035**, Lecture Notes in Mathematics (Springer, 2012), pp. 57–84.
11. H. Ammari, E. Bretin, J. Garnier, and A. Wahab, "in *Mathematical and Statistical Methods for Imaging* Contemporary Mathematics (AMS, 2011).
12. H. Ammari, E. Bossy, V. Jugnon, and H. Kang, SIAM Rev. **52**, 677 (2010).
13. C. Xu, P. D. Kumavor, A. Aguirre, and Q. Zhu, J. Biomed. Opt. **17**, 061213 (2012).
14. B. E. Treeby, J. G. Laufer, E. Z. Zhang, F. C. Norris, M. F. Lythgoe, P. C. Beard, and B. T. Cox, Proc. SPIE **7899**, 78992Y (2011).
15. D. Modgil, B. E. Treeby, and P. J. La Rivière, J. Biomed. Opt. **17**, 061204 (2012).
16. K. R. Waters, J. Mobely, and J. G. Miller, IEEE Trans. Ultrason. Ferroelectr. Freq. Control **52**, 822 (2005).
17. R. M. Quispe-Siccha, B. Reyes-Ramírez, C. García-Segundo, N. Hevia-Montiel, F. Arámbula-Cosío, R. Sato-Berrú, and J. O. Flores-Flores, J. Appl. Res. Technol. **10**, 63 (2012).
18. B. Reyes-Ramírez, C. García-Segundo, and A. García-Valenzuela, Meas. Sci. Technol. **25**, 055109 (2014).
19. B. Reyes-Ramírez, C. García-Segundo, and A. García-Valenzuela, Proc. SPIE **9040**, 90401J (2014).
20. S. R. Arridge, Inverse Prob. **15**, R41 (1999).
21. L. C. Evans, *Partial Differential Equations* (AMS, 1998).
22. P. J. La Rivière, J. Zang, and M. A. Anastasio, Opt. Lett. **31**, 781 (2006).
23. L. D. Landau and E. M. Lifshitz, *Fluid Mechanics*, 2nd ed. (Butterworth-Heinemann, 1987), Chap. VIII.

Index